UNIVERSITY OF CRETE
PHYSICS DEPARTMENT

p-$SrCu_2O_2$ and n-ZnO(:Al) Thin films: *Growth, properties and applications*

MARIA VARDA

MASTER THESIS

SUPERVISOR : DR. ELIAS APERATHITIS (IESL, FORTH)

HERAKLION, NOVEMBER 2008

ACKNOWLEDGEMENTS

The work was supervised by Dr. Elias Aperathitis and Dr. Evie Papadopoulou, to whom I would like greatly to express my acknowledgements for introducing me to this subject and gave me the opportunity to work with them, and for their guidance during our collaboration. Also I would like to thank Dr. E. Chikoidze for making the electrical characterization, Dr. O. Durand for some structural characterization, Vicky Kambilafka for the profilometer measurements, Giannis Lambrakis for the technical support and all the people that supported me during this period. Finally I would like to thank Dr. Panagiotis Tzanetakis and Dr. Zacharias Chatzopoulos for taking part in the examinational committee.

TABLE OF CONTENTS

Aim of the study 1

CHAPTER 1 - TRANSPARENT CONDUCTIVE OXIDES 3

1.1 Introduction 3

1.2 N-type ZnO 4

1.2.1 Crystal structure of ZnO 5

1.2.2 Electronic band structure of ZnO 6

1.3 P-type $SrCu_2O_2$ 8

1.3.1 Crystal structure of $SrCu_2O_2$ 9

1.3.2 Electronic band structure of $SrCu_2O_2$ 10

1.4 References 12

CHAPTER 2 - THE PULSED LASER DEPOSITION TECHNIQUE 15

2.1 Introduction 15

2.2 The process of Pulsed Laser Deposition 16

2.3 The Laser-Target Interaction 18

2.4 The Laser-Plume Interaction 19

2.5 Plasma Plume Expansion 20

2.6 Laser Power Density 22

2.7 Laser Wavelength 22

2.9 Film Growth 23

2.9.1 Particulate formation 24

2.10 References 26

CHAPTER 3 - p-n JUNCTION 27

3.1 Introduction 27

3.2 p-n Homojunction Diode 28

3.3 p-n Heterojunction Diode 32

3.4 References 35

CHAPTER 4 - EXPERIMENTAL,PROCEDURE 37

4.1 Experimental set-up and procedure of the PLD technique 37

4.2 Characterization of the films 39

4.2.1 Profilometer 39

4.2.2 UV-Vis-NIR Spectrophotometer 39

4.2.3 X-ray diffraction 42

4.2.4 Electrical measurements 44

4.3 Rapid Thermal Annealing (RTA) 45

CHAPTER 5 – PULSED LASER DEPOSITION OF UN-DOPED AND Al-DOPED ZnO THIN FILMS 47
5.1 Introduction.....47
5.2 Experimental Conditions 47
5.3 Structural Properties 48
5.3 Electrical Properties 52
5.4 Optical Properties.....54
5.5 Conclusions.....58
5.6 References 59
CHAPTER 6 – PULSED LASER DEPOSITION OF UN-DOPED AND DOPED $SrCu_2O_2$ THIN FILMS 61
6.1 Introduction.....61
6.2 Experimental Conditions 61
6.3 SCO and SCO:X thin films deposited by a 248nm laser 63
6.3.1 SCO thin films 63
6.3.2 Doped SCO thin films 67
6.4 SCO and SCO:X thin films deposited by a 308nm laser 70
6.4.1 SCO thin films 70
6.4.2 Doped SCO thin films 74
6.5 Conclusions.....77
6.6 References 79
CHAPTER 7 – p-n HETEROJUNCTIONS 81
7.1 Introduction.....81
7.2 p-$SrCu_2O_2$ on n-Si 81
7.3 p-$SrCu_2O_2$/n-ZnO on ITO.....84
7.3.1 p-$SrCu_2O_2$:X(3%)/n-ZnO on ITO by a 248 nm laser 85
7.3.2 p-$SrCu_2O_2$:X(3%)/n-ZnO on ITO by a 308 nm laser 86
7.4 References 88
Papers.....91

AIM OF THE STUDY

In the present work, thin films of un-doped and doped ZnO and $SrCu_2O_2$ were grown and then characterized. The technique used for the growth was pulsed laser deposition. The films were mainly characterized according to their structural and optical properties as a function of different deposition parameters, such as substrate temperature and background oxygen pressure. Some electrical measurements also took place. Initially, the aim of the work was to obtain thin films with enhanced crystal structure and tuned electrical properties and transparency from UV to NIR of the spectral region. ZnO is an n-type material of wide ranging applications for a long time, including Transparent Conductive Oxides (TCOs). $SrCu_2O_2$ is a relatively novel p-type material which belongs to the arising p-type TCOs but, still, with inferior properties compared to ZnO and other n-type TCOs. The final aim of the work was to combine the growth of (un-doped or doped) n-ZnO and p-$SrCu_2O_2$ thin films, with the appropriate properties, in order to fabricate and realize a transparent p-n heterojunction. To reach the final aim it is important to fully understand the properties of the films.

The present work was set for the fulfillment of the master degree in "Microelectronics & Optoelectronics" of the Physics Department of University of Crete. It has been carried out in laboratories of the Institute of Electronic Structure & Laser (IESL), Foundation for Research and Technology-Hellas (FORTH). A part of this work was within the framework of the European project FP6 – IST – FET NATCO (Novel & Advanced Transparent Conductive Oxides) (Contract no 511925).

In the following chapters, after an introduction to TCOs, a review of ZnO and $SrCu_2O_2$ materials is presented. This is followed by an introduction to pulsed laser deposition technique and a brief theory on p-n heterojunctions is presented. Next, the experimental set-up and the film characterization methods used for the present work were presented. Finally the presentation and discussion of the results are given along with further work which could be done on TCO materials and devices.

CHAPTER 1
TRANSPARENT CONDUCTIVE OXIDES

1.1 INTRODUCTION

Transparent Conductive Oxides (TCOs) are wide band-gap semiconductors with relatively high concentration of free electrons or holes in their conduction or valence band for n- or p-type, respectively. The electrons or holes arise either from defects in the material or from extrinsic dopants, the impurity levels of which lie near the conduction or valence band edge, respectively.

Despite the fact that there are materials, like metals, which exhibit high conductivity, they are normally opaque. Also there are materials, like oxide glasses, which are highly transparent in visible light but they are insulators. The way to achieve materials being transparent and conductive simultaneously is to understand the fundamental relationships for the structure that a material must have in order to retain both transparency and conductivity. Thereby, TCOs represent a class of materials that combines two properties, conductivity and transparency.

The first realization of a TCO material was published in 1907 by Badekar[1]. Badekar prepared cadmium oxide (CdO) films by thermal oxidation of sputtered films of cadmium. Since then, extensive work has been done to prepare new types of TCOs for wide range applications. Some well-known and widely used n-type TCOs include[2] SnO_2, In_2O_3:Sn (ITO), ZnO etc. Among the n-type TCOs reported so far, ITO has the lowest resistivity of 10^{-4} Ωcm and transparency of 80-90% over visible-NIR spectral range. ZnO:Al has been suggested as alternative oxide to ITO but its performance is still inferior to that of ITO (resistivity $>10^{-4}$ Ωcm).

More recently, p-type TCOs have been documented. Their fabrication has proved to be difficult. Since the valence band of the majority of oxides is composed of 2p-orbitals of oxygen, even if it was possible to achieve p-type hole doping, the films would be strongly localized and carrier mobility would be low. In 1997 Kawazoe et al.[3] reported p-type conductivity in a highly transparent thin film of copper aluminum oxide ($CuAlO_{2+x}$). Since then, a series of p-type TCOs based on Cu^+-bearing oxides, such as $CuGaO_2$ [4], $CuInO_2$ [5], $SrCu_2O_2$ [6] and LnCuOCh (where Ln

= lanthanides and Ch = S or Se)[7] has been reported. The p-type TCOs identified at this point, have resistivities at least one order of magnitude higher than their n-type counterparts (the best one until now is $CuCr_{1-x}Mg_xO_2$ with reported resistivity $4.5x10^{-3}\Omega cm$).

As far as applications are concerned, TCOs are widely applied as transparent electrodes for liquid crystal displays (LCDs), organic light-emitting diodes (OLEDs), solar cells etc.[8] The realization of p-TCOs has opened up a new field in optoelectronics device technology, where a combination of the two types of TCOs in the form of a p-n junction could lead to a ‘‘functional window’’, which transmits the solar radiation at the visible range but absorbs the UV part[3] resulting in electricity generation. These devices can also operate as ‘‘UV-shields’’. Despite the poor performances of p-TCOs, a few transparent p-n junctions have already been reported, such as transparent diodes based on p-n homojunctions ($CuInO_2$)[9] and opto-electronic devices utilizing p-n heterojunctions (p-$SrCu_2O_2$/n-ZnO [10] and p-$ZnRh_2O_4$/n-ZnO UV-LEDs [9,10,11], p-NiO/n-ZnO UV detectors and p-$CuAlO_2$/n-ZnO photovoltaic cells). However, the performance of these diodes was poor due to poor material quality, non-optimum resistivity and carrier concentration of the p-type TCO material or due to non-abrupt interfaces of the heterojunctions. Consequently, the calculated ideality factors was not less than 1.5, the forward to reverse current ratios was between 10 and 80 for potentials less than ±4V, the breakdown voltage was at less than 8 V, there was an increased series resistance and the turn-on-voltage was not corresponding always to the band gap of the materials. The transparency of these devices was between 40% and 80%. The development of enhanced p-type and n-type TCOs not only will benefit the application areas in which they are already used, but also it will give rise to new applications of these materials and their devices, with enormous potential market impact on many aspects of our daily life.

Transparent conductive oxides have been produced by various methods including sputtering[12], pulsed laser deposition[13], chemical vapour deposition[14] and spray pyrolysis[15].

In this work, p-type $SrCu_2O_2$ and n-type ZnO(:Al) were chosen as the TCOs candidates to be studied. In the following sections a brief description of the two materials is given.

1.2 N-TYPE ZnO

Zinc oxide (ZnO) films have been investigated in recent years as TCOs due to their good electrical and optical properties in combination with wide direct band gap, abundance in nature, and absence of toxicity[16]. ZnO is a *n*-type II-VI compound semiconductor with a wide variety of

applications as electrodes, window materials in display, solar cells, and various optoelectronic devices[17]. Table 1.1 shows some basic physical parameters for ZnO. Still some uncertainty exists in these values.

Table 1.1: Basic physical properties of ZnO

Property	***Value***
Stable phase at RT (300K)	Wurtzite
Lattice parameters at RT (300K)	a_o = 0.32495 nm b_o = 0.52069 nm
Density	5.606 g/cm^3
Melting Point	1975 °C
Thermal Conductivity	0.6 W/cm°C
Linear expansion coefficient	a_o : 6.5x10^{-6} /°C c_o : 3.0x10^{-6} /°C
Dielectric constant	8.656
Refractive index	2.008, 2.029
Optical Energy band gap	3.37 eV, direct
Intrinsic carrier concentration	< 10^6 cm^{-3}
Breakdown voltage	5x10^6 V/cm
Saturation velocity	3x10^7 cm/s
Exciton binding energy	60 meV
Electron effective mass	0.24
Hole effective mass	0.59
Electron Hall mobility at 300 K for low n-type conductivity	200 cm^2/Vs
Hole Hall mobility at 300 K for low p-type conductivity	5-50 cm^2/Vs

1.2.1 CRYSTAL STRUCTURE OF ZnO

ZnO crystallizes in three different crystal lattices[18] (i) the hexagonal wurtzite lattice which is mainly used in the thin film industry as a TCO or as a catalyst in methanol synthesis, (ii) the cubic rocksalt (NaCl) structure which is stable only at relatively high pressures and (iii) the zinc-blende ZnO structure which can be stabilized only by growth on cubic substrates. At ambient conditions, the thermodynamically stable phase is wurtzite.

The wurtzite crystal lattice of single crystal ZnO is depicted in figure 1.1. Each O^{-2} is surrounded by four Zn^{+2} at the corners of the tetrahedron, and vice versa. The unit cell contains two Zn^{+2} and two O^{-2}. One important characteristic of the wurtzite structure is its noncentral symmetry. The wurtzite structure of ZnO can be considered as two interpenetrating hexagonal close packed (hcp) sublattices of Zn^{+2} and O^{-2} displaced by the length of cation-anion bond in the c-direction. The polar surfaces are the other important characteristic of the wurtzite structure. The oppositely charged ions produce positively charged (0001)-Zn and negatively charged (0001)-O polar surfaces, resulting in a normal dipole moment and spontaneous polarization along the c-axis. The lattice constants of the ZnO hexagonal unit cell are *a=3.2500 Å* and *c=5.2060 Å*. The c/a ratio for ZnO hcp unit is 1.60, which is very close to the ideal value of 1.633 of hcp. The point defects, such as zinc antisites, oxygen vacancies, and extended defects, such as threading dislocations also increase the lattice constant in ZnO crystal, but for a small extent in heteroepitaxial layers.

The lattice parameters of a semiconductor usually depend on the following factors: (i) free electron concentration, which affects the potential of the bottom of conduction band occupied by electrons, (ii) concentration of foreign atoms and defects and their difference of ionic radii with respect to the substituted matrix ion, (iii) external strains (for example, those induced by the substrate), and (iv) temperature[19]. On the other hand, the strict periodicity of the lattice is disturbed by many imperfections or defects. These imperfections or defects have a considerable and, sometimes, even controlling influence on mechanical, thermal, electrical and optical properties of semiconductors.

1.2.2 ELECTRONIC BAND STRUCTURE OF ZnO

ZnO is a wide-bandgap oxide semiconductor with a direct energy gap (E_g) of about 3.37 eV (at RT). Fig. 1.2 presents the band structure of ZnO. There are six valence bands between –6 eV and 0 eV, at the band structure, where 0 eV is at the upper part of the valence band maximum (VBM). These six valence bands correspond to the oxygen's 2*p* orbitals that contribute to the band structure. Below -6 eV at about –20 eV the VB terminates with the oxygen's 2*s* core like state. This specific band has no significant contribution to the density of states in the conduction band (CB). For the CB there are two bands which are strongly localized on the Zn and correspond to the unoccupied Zn: 3*s* levels.

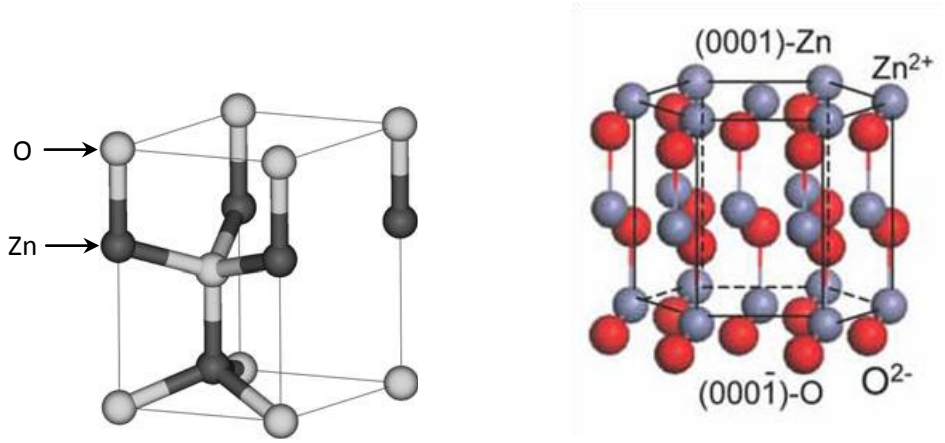

(a) *(b)*

Fig. 1.1: (a) Unit cell of the crystal structure of ZnO. (b) Hexagonal wurtzite structure of ZnO (adopted from [35]).

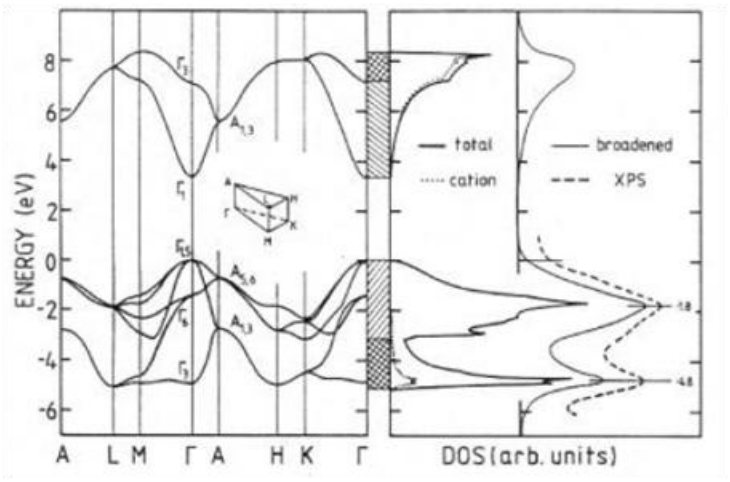

Fig. 1.2: Band structure of ZnO, the zero in the graphs is taken as the valence band upper edge [36].

ZnO with a wurtzite structure is naturally an *n*-type semiconductor because of a deviation from stoichiometry due to the presence of intrinsic defects such as O vacancies (V_O) and Zn interstitials (Zn_i) (giving free carriers). ZnO shows intrinsic *n*-type conductivity with very high electron densities[20] of about 10^{21} cm^{-3}. *N*-type doping of ZnO is relatively easy. Group-III elements Al, Ga, and In as substitutional elements for Zn and group-VII elements Cl and I as substitutional elements for O can be used as *n*-type dopants[21]. Doping with Al, Ga, and In has been obtained by many groups, resulting in high-quality, highly conductive *n*-type ZnO films[22].

In the present work, aluminum (Al) was used as the dopant element for ZnO. Al acts as effective donor due to contribution from Al^{3+} on the substitutional site of Zn^{2+} as well as Al interstitial atoms that change the oxygen vacancy characteristics, leading to very low resistivity.

1.3 P-TYPE $SrCu_2O_2$

As mentioned above, a possible reason for the difficulty in preparing p-TCO is the electronic structure of the metal oxides. There is a strong localization of holes at oxygen *2p* levels on the valence band edge due to the high electronegative nature of oxygen. O *2p* levels are far lower lying than the valence orbit of metallic atoms, leading to the formation of a deep acceptor level by the holes. In other words, the holes have high probability to be localized around the oxygen atoms. Hence, these holes require high enough energy to overcome a large barrier height in order to migrate within the crystal lattice, resulting in poor conductivity and hole mobility. A possible solution for reducing the strong localization was proposed by Kawazoe et al.[23] According to them, the introduction of a ‘‘degree of covalency’’ in the metal-oxygen bondings would induce the formation of an extended valence band structure, i.e. the valence band edge should be modified by mixing orbitals of appropriate counter cations that have energy-filled-levels comparable to the O *2p* level. This would reduce the strong coulombic force by oxygen ions thereby delocalizing the holes. This main approach to obtain p-TCO is called ‘‘Chemical Modulation of the Valence Band (CMVB)’’. Investigations showed that the required cationic species, that will serve the CMVB technique, are the $3d^{10}$-closed shell of Cu^+ ions and $4d^{10}$-closed shell of Ag^+ ions.

According to the considerations mentioned above and after the discovery of p-type transparent conductive $CuAlO_2$ thin films[3], there has been an increasing interest in developing copper-based p-type TCOs. $SrCu_2O_2$ (SCO) is an interesting candidate p-type TCO. Von Teske et al.[24] first achieved to grow SCO monocrystal. Suzuki et al.[25] followed with the report of their work on the Sr–Cu–O bulk phase diagram. More recently, the growth of SCO thin film was reported by several deposition techniques. In 1998, Kudo et al.[6] published the fabrication of highly transparent un-doped and K-doped SCO thin films, by pulsed laser deposition. The thin films exhibited high transparency and phase pure crystal structure. They reported low mobility, $2.56x10^2$ Ωcm and 20.8 Ωcm resistivity and 10^{14} cm^{-3} and $6.1x10^{17}$ cm^{-3} hole concentration, respectively. In 2003, Ginley et al.[26] obtained phase pure high quality SCO films by spray and sol–gel technique. Bobeico et al.[27] fabricated SCO thin films by e-beam evaporation. They reported polycrystalline structure, 60% transparency in the visible region, 18.9 Ωcm resistivity, $1.5x10^{17}$ cm^{-3} hole concentration and 2.2 cm^2/Vs hole mobility. However, the film obtained more than one crystalline phases. In 2005, Varadarajan et al.[28] fabricated opaque, with nearly phase pure and high density of defects un-doped and K-doped SCO thin films, by pulsed laser deposition. The un-doped films exhibited insulating behavior and the K-doped films had 140 Ωcm resistivity. In 2006, Sheng et al.[29] deposited Ca-doped SCO thin films by pulsed laser

deposition. The films exhibited low transmittance in the visible region, low crystal quality and resistivity of the order of ~12.2 Ωcm. For the lowest temperature deposited film, the hole concentration and mobility were $1.33x10^{17}$ cm^{-3} and 3.82 cm^2/Vs. In 2008, Papadopoulou et al.[13] fabricated SCO thin films by pulsed laser deposition. They reported transparent, with phase pure SCO films, ~10^3 Ωcm resistivity and ~10^{13} cm^{-3} hole concentration.

1.3.1 CRYSTAL STRUCTURE OF $SrCu_2O_2$

SCO has a body-centered tetragonal crystal structure, presented in fig. 1.3, and belongs to the $I4_1/amd$ space group[24]. The crystal has an O–Cu–O dumbbell-shaped structure[30,31]. The dumbbell-shaped structural units are connected to form zig-zag, one-dimensional chains running along [100] and [010] directions at an angle of 96.25° (experimental value). The electronic interactions between d^{10} electrons of the nearest neighboring Cu^+ ions are restricted to a single chain. The fact that the chains are one-dimensional comparing to the three-dimensional chains of Cu_2O, which has a similar crystal structure, favors the reduction of the Cu-Cu interaction resulting in the increase of the optical band gap. A Sr^{+2} is coordinated by six O^{-2} to form a slightly distorted octahedron.

According to Modreanu et al.[32] the computed lattice parameters for SCO from XRD measurements are *a=b=0.5469 nm* and *c=0.9826 nm* and by PBE-PAW are *a=b=0.5447 nm* and *c=0.9871 nm.*

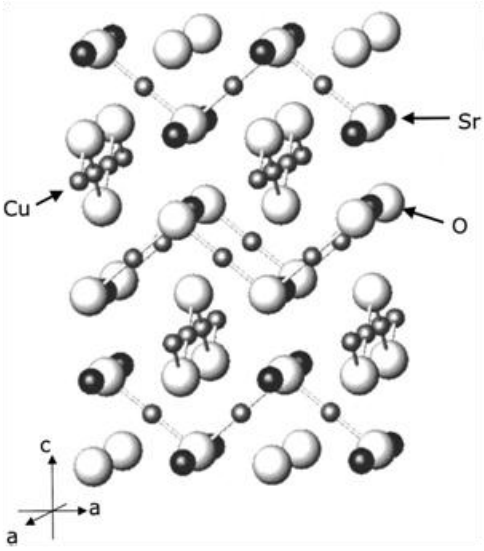

Fig. 1.3: Schematic illustration of the $SrCu_2O_2$ crystal structure (adopted from [31]).

1.3.2 ELECTRONIC BAND STRUCTURE OF $SrCu_2O_2$

The SCO material has a direct optical band gap of about 3.3 eV (experimental value for the bulk)[30]. Fig. 1.4 presents the electronic band structure of $SrCu_2O_2$ [32]. The valence states of $SrCu_2O_2$ consist of two major parts. The upper part of the VBM (0 eV) to -3 eV the states that exist correspond predominantly to the Cu 3*d* states. The lower part, from -3 eV to -6 eV consists predominantly the O 2*p* states. This is due to the fact that Cu 3*d* level is shallower than O 2*p*. So, the Cu containing oxides have much higher VBM than other conventional oxides such as ZnO, where the Zn 3*d* state is deeper than the O 2*p* state. Higher VBM leads to higher *p*-type dopability as suggested by the doping limit rule[33]. Also in the VBs there are significant hybridization between the Cu 3*d* and O 2*p* states. The contribution of Sr orbitals to the VB is negligible. The role of Sr is not to modify the nature of the VB or CB, in a way it reduces the density and dimensionality of Cu–Cu interactions in the structure. This leads to a narrowing of the valence band width resulting in an enhanced band gap. The CBM is a mixture of Cu *4s* and *3d* with O *2p* and some Sr *4s* orbitals. SCO not only has a sufficiently large band gap, but also does not absorb visible light between the VBM and the bands below, due to forbidden transition according to the classical selection rule[33].

The highest energy valence bands are important for p-type conduction in SCO. In the top of the VB, the curvature in Γ-X or Γ-M, which is along the [100] or [110] direction respectively, is smaller than in the Γ-Z [001] direction [30, 31]. As a result, the hole effective mass along the [100] and [110] is smaller than along the [001] direction. As mentioned in paragraph 1.3.1, the zig-zag chains of O–Cu–O dumbbells are aligned with the [100] and [010] axes and thus are likely responsible for positive hole transport in SCO. The origin of p-type conductivity is the Cu vacancy formation[34] (each vacancy contributes one hole). The energy cost for forming Cu vacancies is determined by the interplay between the dimensionality of Cu-Cu interactions and the proximity of the Cu atoms. For a Cu vacancy there is no significant change in the structure, around the vacancy site. The distance between Cu-O, nearest the vacancy, is reduced and the nearest Sr atoms are pulled toward the vacancy. The formation of a neutral Cu vacancy results in the appearance of a delocalized hole state above the VB. The Cu vacancy formation results in the reduction in the number of Cu-Cu interactions in the structure and so a further increase of the band gap occurs.

According to Modreanu[32] the computed effective masses for the holes are $m^*=-9.6$, -0.70 and $-1.90\ m_e$, in order of increasing band energy.

In the current study, a dopant element for SCO was used, which was considered to substitute Sr atoms. The specific dopant element is expected, according to theoretical investigations, to little affect the band gap and the hole effective mass compared to un-doped

SCO. Doping SCO intends to decrease the Cu vacancy formation energy for a given vacancy concentration. Upon Cu vacancy formation the band gap is enhanced.

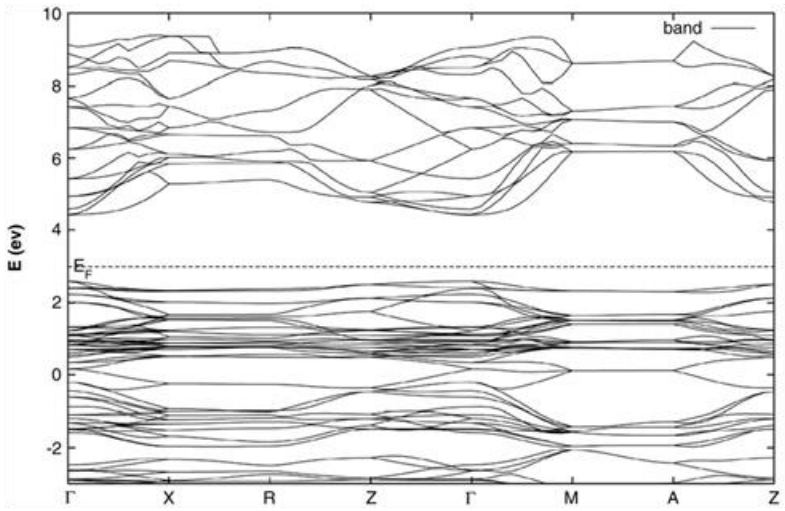

Fig. 1.4: Electronic band structure of $SrCu_2O_2$ computed with DFT (adopted from [32]).

1.4 REFERENCES

[1] K. Badekar, Ann. Phys. (Leipzig), 22 (1907) 749

[2] G. Rupprecht, Z. Phys. 139 (1954) 504

R.J. Lad et al., J. Vac. Sci. Technol., 17 (1980) 808

[3] H. Kawazoe et al., Nature, 389 (1997) 939

[4] K. Ueda, et al., J. Appl. Phys. (2001) 89 (3), 1790

[5] H. Yanagi, et al., Appl. Phys. Lett. (2001) 78 (11), 1583

H. Yanagi, et al., Solid State Commun. (2001) 121 (1), 15

[6] A. Kudo, et al., Appl. Phys. Lett. (1998) 73 (2), 220

[7] K. Ueda, et al., Appl. Phys. Lett. (2000) 77 (17), 2701

[8] J.C.C. Fan et al., J. Electrochem. Soc. 122 (1975) 1719

B.G. Lewis, D.C. Paine, MRS Bulletin on TCO, vol. 25, 2000, p. 22

D. S. Ginley and C. Bright, Mater. Res. Soc. Bull., (2000) 25 (8), 15

H. Hosono et al., Thin Solid Films, (2003) 445 (2), 155-392

[9] K. Tonooka, et al, Thin Solid Films, 445 (2003) 327

[10] H. Hosono, et al, Vacuum, 66 (2002) 419

[11] H. Ohta, et al, Applied Physics Letters, 82 (2003) 823

[12] R.P. Howson et al., Thin Solid Films, 63 (1979) 163

N. L. Dehuff et al., J. Appl. Phys., 97/6 (2005) 064505

[13] E. Papadopoulou et al., Thin Solid Films, 516 (2008) 1449

S. Christoulakis et al., Rev. Adv. Mater. Sci., 10, 4 (2005) 331

M. Grundmann et al., Superlattices Microstruct., 38, 4-6 (2005) 317

[14] K. Kane et al., Thin Solid Films 29 (1975) 155

Y. Yang et al., J. Am. Chem. Soc., 127, 24 (2005) 8796

[15] J. J. Prince et al., J. Cryst. Growth, 240, 1-2 (2002) 142

[16] S. H. Jeong, J.W. Lee, S.B. Lee, J.H. Boo, Thin solid films 435(2003) 78-82

[17] K. Vanheusden, et al., J. Appl. Phys 79, 7983 (1996)

D.P. Norton, et al., Materials today (June 2004) 34-40

H.Y. Kim, et al., Optical materials 17 (2001) 141-144

[18] S. Desgreniers, Phys. Rev. B 1998, 58, 14102

C. Klingshirn, Chem. Phys. Chem., 8, (2007) 782 – 803

R.G. Gordon, MRS Bulletin/August (2000) 52-57

[19] Özgür, et al., J. Appl. Phys 98, 041301-1 (2005)

A.F. Ioffe, Physics of semiconductors, Academic Press Inc., New York 1960, 148-151

[20] T. Minami, et al., Jpn. J. Appl. Phys., Part 2, 24 L781 (1985)

[21] H. Kato, et al., J. Cryst. Growth 237–239, 538 (2002)

[22] S. Y. Myong, et al., Jpn. J. Appl. Phys., Part 2 36, L1078 (1997)

A.V. Singh, et al., J. Appl. Phys., 95, 7 (2004)

B. M. Ataev, et al., Thin Solid Films, 260, 19 (1995)

V. Assuncao, et al., Thin Solid Films 427, 401 (2003)

Z. F. Liu, et al., J. Cryst. Growth 259, 130 (2003)

T. Minami, et al., Jpn. J. Appl. Phys., Part 2 23, L280 (1984)

B. Kotlyarchuk, et al., Cryst. Res. Technol. 40, 12 (2005) 1118 – 1123

[23] H. Kawazoe, et al., MRS Bull. (August 2000) 28

[24] Von Chr. L. Teske, et al., Z. Anorg. Allg. Chem., 379 (1970) 113–121

[25] R.O. Suzuki, et al., J. Am. Ceram. Soc., 75 (1992) 2833

[26] D. Ginley, et al., Thin Solid Films, 445 (2003) 193

[27] E. Bobeico, et al., Thin Solid Films, 444 (2003) 70

[28] V. Varadarajan, et al., Thin Solid Films, 488 (2005) 173

[29] S. Sheng, et al., Semicond. Sci. Technol., 21 (2006) 586

[30] X. Nie, et al., Phys. Rev. B, 65 (2005) 075111

[31] H. Ohta, et al., J. Appl. Phys., 91, 5 (2002)

[32] M. Modreanu,et al., Thin Solid Films, 515 (2007) 8624–8631

[33] S. B. Zhang, et al., J. Appl. Phys., 83, No. 6 (1998)

[34] M. Nolan, S.D. Elliott, Phys. Chem. Chem. Phys., 8 (2006) 5350

[35] Z. L. Wang, "Nanostructures of ZnO", Materials today, June 2004

[36] W. Göpel, et al., Phys. Rev. B 26 (1982) 3144-3150

CHAPTER 2
THE PULSED LASER DEPOSITION TECHNIQUE

2.1 INTRODUCTION

Pulsed Laser Deposition (PLD) is only one of many thin film deposition techniques. The history of laser-assisted film growth started soon after the technical realization of the first laser in 1960 by Maiman[1]. Smith and Turner[2] utilized a ruby laser to deposit the first thin films in 1965. However, the deposited films were still inferior to those obtained by other techniques such as chemical vapor deposition and molecular beam epitaxy. In the early 1980's, a few research groups achieved remarkable results on manufacturing thin film structures utilizing laser technology. The breakthrough came in 1987 when Dijkkamp and Venkatesan[3] deposited a thin film of $YBa_2Cu_3O_7$, a high temperature superconductive material, which was of superior quality than films deposited with alternative techniques. Since then, the technique of Pulsed Laser Deposition has been utilized to fabricate high quality crystalline films. The deposition of ceramic oxides, nitride films, metallic multilayers and various superlattices has been demonstrated. In the 1990's the development of new laser technology, such as lasers with high repetition rate and short pulse duration, made PLD a competitive tool for the growth of thin, well defined films with complex stoichiometry, even in low deposition temperatures.

In comparison with other deposition techniques, such as sputtering, molecular beam epitaxy (MBE) and chemical vapour deposition (CVD), the PLD technique is simpler, faster and more controllable. Using a pulsed UV-laser and a vacuum chamber, a variety of stoichiometric oxide films can be grown without the need for further processing. By appropriate programming and using multiple targets, the PLD technique allows the growth of multilayered films, useful for the production of multicomplex materials and devices (e.g. growth of capacitors and piezoelectric elements).

A significant disadvantage of PLD is that, during the PLD process, large and undesirable particulates can appear on the deposited area, which can cause undesirable surface characteristics

(droplets). This fact is limiting the extended use and the institution of the technique in an industrial level. Although some techniques for the reduction of the particulates have been found, their complete elimination hasn't been achieved yet. In addition, there is a difficulty in fabricating uniform films at a large area.

The following paragraphs are an introduction to the Pulsed Laser Deposition technique[4].

2.2 THE PROCESS OF PULSED LASER DEPOSITION

The pulsed laser deposition, shown schematically in Figure 3.1, is a physical vapor deposition technique based on the evaporation of material by means of a pulsed, highly energetic laser beam focused on a solid target by a lens. If the density of the laser energy has sufficient value for the ablation of the target, the material evaporates, forming a gas plasma (i.e. an electrified gas of electrons, ions and neutrals that maintains quasi charge neutrality) with the characteristic shape of a plume. This plasma plume expands along the direction normal to the target surface and a part of it is deposited on a substrate. The substrate is placed parallel in front of the target, usually at distances between 4 and 6 cm.

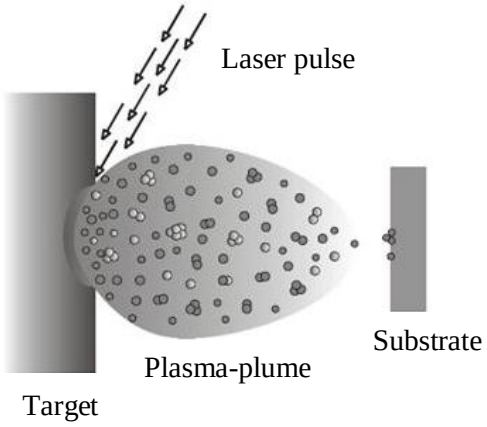

Figure 2.1 : Schematic presentation of the pulsed laser deposition process. Laser pulses irradiate a target, material is ejected and deposited on a substrate placed nearby.

The PLD process can mainly be divided into four regimes:

1. The interaction of the laser beam with the target resulting in evaporation of the surface layers
2. The interaction of the laser beam with the evaporated materials, when using a laser with pulse duration, causing the formation of isothermal expanding plasma

3. The anisotropic three-dimensional adiabatic expansion of the laser-induced plasma with a rapid transfer of thermal energy of the species in the plasma into kinetic energy
4. Film growth.

The time scales involved in the above process steps are very different. The first two regimes start with the laser pulse and continue until the next laser pulse. The next regimes start after the laser pulse terminates. The plume expansion, in a background gas, takes place within microseconds. Depending on the experimental conditions, the film growth process following a laser pulse can continue to develop until the next laser pulse occurs. Each step of the process depends significantly on the material of the target as well as on the experimental parameters such as laser wavelength, laser fluence (i.e. the density of energy on the target) and pulse width, background gas type and pressure, substrate type and temperature, and deposition geometry. Some typical parameters for the PLD are listed in Table 2.1.

Table 2.1: Typical PLD parameters

Parameter	***Typical values***
Materials examples (multicomponent oxides)	YBCO, BiSrCaCuO, $BaTiO_3$, ZnO, …
Laser wavelength	between 200 – 400 nm (e.g. 193, 248, 266, 308, 355 nm, etc.)
Laser pulse width	6 – 50 ns
Laser repetition rate	1 – 10 Hz
Fluence	0.5 – 5 J/cm^2
Base vacuum pressure	~ 10^{-6} torr
Background gas	O_2 , O_3, N_2O, NO_2, …
Background gas pressure	1 – 300 mtorr
Substrate examples	MgO, $SrTiO_3$, Si, Al_2O_3, glass, SiO_2, …
Substrate Temperatures	25° - 750°C

Due to the correlation between the above physical mechanisms involved in PLD process, only an approximated description of the phenomenon is possible.

Fig. 2.2 shows a schematic representation of the pulsed laser ablation and deposition. In the following paragraphs the process steps of PLD will be described briefly.

2.3 THE LASER-TARGET INTERACTION

When a pulsed laser beam interacts with a solid target, the local temperature of the target surface is increased. If the temperature overcomes the vaporization temperature of the material then ablation takes place on the surface of the target. Here ”ablation” covers a variety of processes that occur during the interaction such as absorption, surface melting and vaporization, ejection of particles, and plasma formation and expansion. If the laser power density is high enough (~10^9 W/cm^2), this interaction may look like an explosion[5].

The ablation process is complex as it depends on a number of parameters such as the absorption coefficient and reflectivity of the target material, as well as the laser parameters such as wavelength, fluence and pulse duration.

The first step in any structural modification of a material by laser radiation is the deposition on the surface of a certain amount of laser energy. The total laser energy and the spatial and temporal energy distributions determine the kind of final modification that will be obtained. When a laser pulse hits the surface of a target, photons are immediately absorbed by electronic processes, and electrons are excited from their equilibrium states to some excited states. For example, in semiconductors, electrons can be excited from the valence band to the conduction band. The electronic transitions can be via single photons, two-photon or higher order multiphoton absorption. Single photon absorptions are the main processes during irradiation with a laser beam of short pulse duration (ns). Irradiation with a laser beam of shorter pulse duration (ps, fs), multiphoton excitation processes occur and the probability of nonlinear absorption increases strongly with laser intensity. After the occupation of the electronic states by the excited electrons, the carrier–carrier interaction processes begin and a quasi-equilibrium situation is established among the electrons on a time scale of about 10^{-13} s after the laser pulse[6]. The quasi-equilibrium electrons cool down on a time scale of 10^{-13} to 10^{-12} s by emission of phonons. The energy of the phonons is converted to heat[i,7] via vibration of the lattice and thermal diffusion can take place on a time scale of the order of 10^{-11} s. When the temperature of the material exceeds the melting point then a transition from solid to liquid state takes place. The melted surface starts to vaporize on a time scale of the order of 10^{-10} s. The high temperatures generated at the target surface (up to several thousand degrees Celsius) cause emission of many species (ions, electrons, neutral atoms and molecules) from the target.

---

[i] Heating begins within the optical absorption depth of the material *1/a*, where *a* is the optical absorption coefficient. If the thermal diffusion length, given by $L_{th} = \sqrt{2D\tau_L}$ (where *D* is the thermal diffusion constant and τ_L the pulse duration), is smaller than *1/a*, the bulk will be heated down to *1/a*, independent of pulse duration. If L_{th} is greater than $1/\alpha$ then the bulk will be heated down to L_{th}.

There is a distinct dividing line at about 10^{-12} s separating the regime of non-thermal processes and thermal processes[6]. When using a laser with a pulse duration of the order of picoseconds or longer, the processes, that take place to bring a modification on the surface, are thermal, i.e. thermal mechanisms are happening on a time scale of the order of 10^{-12} s (picosecond) and more. When the laser pulse duration is significantly shorter than the time needed for the excited electrons to emit phonons, then non-thermal processes, which happen sooner than a picosecond, can be approached.

2.4 THE LASER-PLUME INTERACTION

The laser pulse duration plays a crucial role in the laser–plume interaction. In the case of nanosecond laser pulse, the evaporated material interacts with the laser beam ”tail”.

After the ablation, further irradiation by the laser beam ionizes the evaporated material and an expanding plasma is formed above the target surface[8]. The plasma absorbs the laser light mainly by inverse-Bremsstrahlung (IB) processes and direct single-photon processes which results in further heating of the plasma. IB involves absorption of photons by free electrons which are accelerated during collisions with neutral or ionized atoms. The excited particles will emit photons, leading to a bright plasma-plume, which is characteristic for the laser ablation process. The plasma absorbs the laser light at distances very close to the target, where the densities of the charged particles are very high. Typical plasma temperatures, measured by emission spectroscopy, during the initial expansion are ~10,000 K (~1eV), well above the boiling points of most materials ($\leq$ 3000 K). The maximum temperature induced in the plasma depends on the laser power density and the laser wavelength.

The absorption of the laser radiation by the plasma is a function of the plasma density, the plasma temperature and the laser wavelength. For sufficiently long laser pulses (and/or high laser power densities), the electron density near the target surface becomes so dense that the plasma becomes opaque and the laser-target interaction becomes difficult, the so-called plasma shielding effect[9]. However, as the plasma expands, it becomes less dense, transparent to the laser beam and the laser may again interact with the target surface.

2.5 PLASMA PLUME EXPANSION

In PLD the plasma plume typically expands in vacuum or in a background gas atmosphere that is used in order to confine the plume or adjust the film stoichiometry.

During irradiation of a target, in vacuum, with a laser pulse of around 30 ns duration, a bubble of hot plasma is formed less than approximately 50 μm from the target surface[8].

When the quantity of the ablated particles is much above 0.1 monolayers per nanosecond pulse, the particles cannot escape without collisions. That is, the ablated particles close to the target surface have an anisotropic velocity distribution (all velocity vectors point away from the target surface) which tends to be transformed into an isotropic one by collisions among the ablated particles. In this way the particles tend to come to equilibrium. This happens within a few mean-free paths from the surface of the target, a region known as the Knudsen layer. It is mainly within this Knudsen layer that laser energy is absorbed by the plasma[10].

As soon as the laser pulse ends, an adiabatically expanding plume is formed in which the plume energy, initially purely thermal, is progressively transformed into kinetic energy during the expansion. The theoretical description of the adiabatic expansion has been considered by Anisimov[11] et al. and Singh and Narayan[12]. Both considerations agree with the fact that the plasma expands in the direction of maximum pressure gradients. They show that the acceleration of the plasma varies inversely with its dimensions. Consequently, the highest velocities are obtained in the direction perpendicular to the target surface, where the initial plasma dimension is only tens of micrometers.

During PLD, in the presence of a background gas, the plume particles will collide with the gas particles, which can lead to scattering, attenuation and thermalization of the plume. Thereby, important film growth parameters such as the spatial distribution, the deposition rate and the kinetic energy distribution of the depositing species are changed. Furthermore, the plume particles can chemically react with the gas particles. This can result in the formation of molecules or clusters leading to the incorporation of the gas into the growing film.

The initial expansion of an ablation plume in a background gas does not differ much from the expansion in vacuum. The expansion is soon largely controlled by the interaction processes between the ablated particles and the background gas particles. The plume, which has a hemispherical shape, continues to expand until the internal pressure is equal to the background pressure.

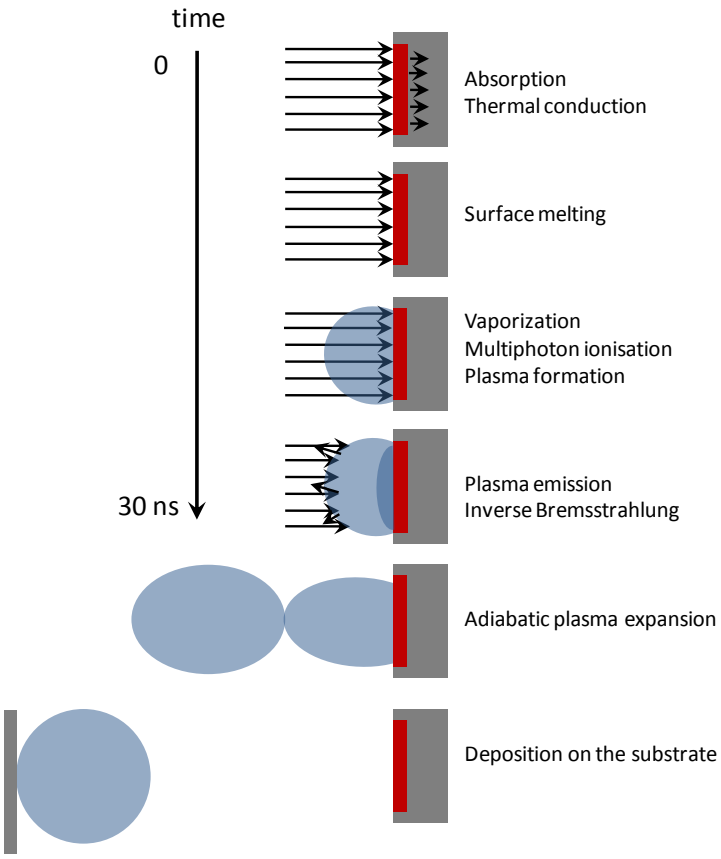

Fig. 2.2: Schematic representation of the pulsed laser ablation and deposition.

Complex plume

The plume composition is complex, especially for multicomponent targets, and may change during expansion. In the first few millimeters of the plume expansion, emission from atoms and ions, multiply charged ions and molecules can typically be observed together with Bremsstrahlung emission in the plasma. After the first millimeters of expansion, Bremsstrahlung emission and emission from multiple charged ions are no longer observed. Electrons, being much lighter, have much greater mobility than ions or neutrals, but are prevented from escaping from the dense plasma by the strong Coulombic attraction that develops as they attempt to separate from the ions. In fact, this is the basis for the *space charge acceleration model*[8] which is used to rationalize the observation that ions in ablation plumes consistently propagate faster than the corresponding neutrals; electrons at the periphery of the expanding plume attract, accelerate, and proximate ions thereby inducing further localized charge separations and further acceleration of the charged components within the plume.

2.6 LASER POWER DENSITY

A characteristic feature of laser ablation is the existence of a laser ablation threshold. Every material has a threshold laser power density value below which ablation, i.e. measurable material removal, is not possible. This threshold power density may be lower for non-metals than for metals, which is due to the poor energy transport in non-metals giving rise to higher surface temperatures during the ablation process. Typical threshold laser power densities[13,14] are in the order of 10^7-10^8 W/cm^2. Above the ablation threshold, the ablation rate increases nonlinearly with increasing laser power density.

If the power density is too close to the ablation threshold, the material removal is low and non-stoichiometric transfer of target material is possible for multicomponent targets. If the power density is too high, however, a large amount of the laser energy is ”wasted” in plume heating and ionization instead of being used for heating the target surface.

2.7 LASER WAVELENGTH

The laser wavelengths used for pulsed laser ablation are typically between 200 and 400 nm[15]. This is because most materials used for deposition exhibit strong absorption in this spectral region. For most metals, when decreasing the laser wavelength in this spectral region, there is a tendency of the absorption coefficients increase and the optical penetration depths of the target materials reduce correspondingly. The stronger absorption at the short wavelengths also results in a decrease in ablation fluence thresholds.

Wavelengths in the visible or infrared part of the photonic spectrum are problematic as they greatly enhance the inverse-Bremsstrahlung. Below 200 nm, strong absorption of molecular oxygen can make the beam control difficult if film deposition is performed in an oxygen background gas. Furthermore, the optics are more difficult at shorter UV-wavelengths as special and expensive optical components are needed at these wavelengths.

2.8 SURFACE MODIFICATION OF THE TARGET

The laser ablation process alters the target surface topology and can change the chemical composition of the target surface as well. After several laser pulses, an initially flat target surface will typically convert to a rough surface morphology exhibiting small structures like cones,

ripples or ridges[16]. In order to obtain steady state laser ablation, preconditioning (pre-ablation) of the target is necessary.

In a laser deposition experiment, the laser beam is usually incident at 30°-45° to the target surface. Thereby, the laser-plasma interaction is reduced and any laser-substrate interaction is avoided. A drawback of this geometry is that the laser may etch a trench into the target so that the plume tilts back towards the laser beam[17].

2.9 FILM GROWTH

In PLD, when using a ns laser at 10 Hz of repetition rate, the substrate is typically exposed to an incident flux of ablated particles for approximately 1 ms in duration, followed by a period of approximately 100 ms during which no ablated material arrives before receiving the next flux. The evolution of the film is taking place during the periods when the substrate is being exposed to the ablated flux. The incident atoms may be re-evaporated from the substrate or they could sputter pre-deposited atoms. For film growth, however, some of the ablated particles must accommodate. Depending on the particles' kinetic energy, the accommodation may involve adsorption onto the surface, or more violent embedding and damage of the pre-existing film. Larger incident particles may fragment on impact. Once they arrive at the substrate, the particles can diffuse over the substrate, nucleate with pre-existing surface and clusters, or induce fragmentation of pre-existing clusters[18]. In many deposition experiments, substrate surface defects such as atomic steps, dislocations and point defects, provide low-energy sites at which nucleation preferentially occurs. Similarly, there are situations where epitaxial growth is possible – most generally when the lattice mismatch between the material of the film and the substrate is small.

Film growth and chemistry may be enhanced or modified by carrying out PLD in an ambient background gas[19]. The gas has two effects that are expected to influence the film formation: it reduces the energy of the ablated particles, and it provides a high flux of background gas particles bombarding the substrate surface during the deposition which is compensating for the loss of an elemental component of the target through incongruent ablation and finally growing the desired film stoichiometry[20].

The laser wavelength affects the nature of the ablated particles[19]. As a result of a change in the optical penetration depth of the laser on the target and a change in the interaction of the radiation field with ablated material the vapor flux composition varies from large clusters and particulates (for IR irradiation) to atoms (for UV irradiation).

During thin film growth, the simultaneous heating of the substrate is frequently desired in order to favor the diffusion of the adsorbed vapor atoms on the substrate. Investigations[21] of the structural properties and the stoichiometry of films, deposited at different experimental conditions (substrate temperature, fluence, target-substrate distance) has shown that there is a critical substrate temperature, T_c, below which the crystal structure of the films mostly contains amorphous phase and the film composition deviates significantly from the stoichiometric one. The velocity of crystallization strongly depends on the substrate temperature. This temperature determines the heat loss of the condensate through the substrate. The higher the cooling rate of the condensate, the lower is the velocity of the crystallization.

2.9.1 PARTICULATE FORMATION

During laser irradiation, macroscopic particulates can appear on the surface of the film. Their occurrence results from four phenomena[22]:

1. Subsurface boiling. It occurs in target materials in which the time needed to convert laser energy into heat and transfer it into the bulk is shorter than the time needed to evaporate the surface layer. Under this condition the subsurface layer is superheated before the surface itself has reached the vapor phase. This process will expel micro-sized globules onto the substrate.
2. Recoil pressure. When the melted layer below the laser focus spot is subjected to the recoil pressure exerted by the shock wave of the expanding plume, droplets can be ejected as the melt is squeezed onto the solid bulk.
3. Exfoliation, which describes the particulate ejection due to the morphology of the target. During repetitive laser ablation (melt-freeze cycles) of the target, microstructures are formed, of only a few microns in dimension, on the surface of the target. Mechanically these structures are fragile and can be broken by the thermal shock induced by the intense laser irradiation.
4. Condensation from vapor species due to supersaturation which is most likely observed when high gas pressure is used.

Combining the effects of laser wavelength λ and laser fluence, more and larger particulates are generated when using laser parameters which favor deeper penetration depth. Massive splashes occur as the penetration depth increases further, which lead to predominantly particulate formation. On the other hand, little penetration depth is not beneficial, since it results in incongruent evaporation and very poor, slow deposition. For most metals, the absorption coefficient α decreases with decreasing λ. Hence, the laser penetration depth in metals is larger in the UV range that in the IR range. For other materials, the variation of α with λ is more complex

since various absorption mechanisms, such as lattice vibrations, free carrier absorption, impurity centers or band gap transition, may occur. For the oxide superconductors, the penetration depth appears to be larger in the near IR than in the UV.

When a PLD experiment is done in poor vacuum, with an ambient gas, or at a substantially large target-to-substrate distance in which coalescence of particulates can take place, markedly different particulate appearance may occur, depending on the position of the substrate.

A way to reduce particulate formation is to reduce the laser fluence, below the threshold level for explosive boiling. It is commonly believed that particulates can be minimized by working with targets of high density. Several other ways for particulate reduction have been demonstrated, though these usually require some redesign of the deposition chamber[21].

2.10 REFERENCES

[1] T. H. Maiman, Nature, 187 (1960) 4736, pp. 493-494

[2] H. M. Smith and A. F. Turner, Appl. Opt., 4 (1965) 147

[3] D. Dijkkamp and T. Venkatesan, Applied Physics Letters, 51, No. 8 (1987) pp. 619-621

[4] "Pulsed Laser Deposition of Thin Films", ed. by D.B. Chrisey, G.K. Hubler (Wiley, New York 1994)

[5] R.E. Russo, Appl. Spectrosc., 49, 14A (1995)

[6] D. von der Linde et al., Applied Surface Science 109, 110 (1997) 1–10

[7] P. R. Willmot et al., Reviews of Modern Physics 72, 1 (2000) 315-328

[8] D.B. Geohegan in [4] p. 115-165

[9] X. Mao, R.E. Russo, Observation of plasma shielding by measuring transmitted and reflected laser pulse temporal profiles, Appl. Phys. A 64 (1997) 1–6

[10] R. Kelly, A. Miotello in [4] p.55-87

[11] S. I. Anisimov et al., Phys. Rev. B 48, 16 (1993) 12076-12081
S. I. Anisimov et al., Applied Surface Science, 96-98 (1996) 24-32

[12] R. K. Singh and J. Narayan, Phys. Rev. B 41, (1990) 8843-8859

[13] "Laser Ablation and its Applications", chapter 4 : Plume Dynamics, ed. by J. Schou, S. Amoruso and J. G. Lunney

[14] J.C.S. Kools in [4] p. 455-471

[15] S.M. Green, A. Piqué, K.S. Harshavardhan, J.S. Bernstein in [4] p. 23-54

[16] S.R. Foltyn in [4] p. 89-113

[17] J.A. Greer et al., Nucl. Inst. and Meth. in Phys. Res. B 121,357 (1997)

[18] M. N. R. Ashfold et al., Chem. Soc. Rev., 2004, 33, 23–31

[19] J.S. Horwitz, J.A. Sprague in [4] p. 229-254

[20] Gupta, A., and B. W. Hussey, 1991, Appl. Phys. Lett. 58, 1211

[21] "Trends in quantum electronics", ed. by S. Metev and M. Sendova, vol.1033, p. 260, SPIE

[22] Li-Chyng Chen in [4] p.167-198

CHAPTER 3
p-n JUNCTION

3.1 INTRODUCTION

One of the main utilities of semiconductors, in a wide range of electronic devices (i.e., devices that employ the transport properties of carriers in the material) and optoelectronic devices (i.e., devices for the generation and detection of light), is related to their capability to form various electrical junctions. Some of these junctions include p–n homojunctions and heterojunctions. The basic theory of current-voltage (I-V) characteristics of p-n junctions was established by Shockley[1]. This theory was then extended by Sah, Noyce, and Shockley[2], and by Moll[3]. Junction structures have been used in fabricating switching diodes, diode rectifiers, solar cells, light emitting diodes (LEDs), laser diodes (LDs), photodetectors, bipolar junction transistors (BJTs), heterojunction bipolar transistors (HBTs), junction field-effect transistors (JFETs), metal–semiconductor field-effect transistors (MESFETs) and several other devices. The p-n heterojunctions can be formed from a wide variety of elemental and compound semiconductors such as n-Si/p-SiGe, p-AlGaAs/n-GaAs, p-Ge/n-GaAs, p-InAlAs/n-InGaAs, p-GaN/n-InGaN, n-ZnO/p-Si and other semiconductor heterojunction devices. Some fabricated homojunctions are p/n Si, GaAs, ZnO etc. These material systems have been fabricated using different growth techniques such as molecular beam epitaxy (MBE), metal-organic chemical vapor deposition (MOCVD), sputtering, liquid-phase epitaxy (LPE) etc.

The following sections are an introduction to the theory of p-n homojunction and heterojunction diodes[4,5].

3.2 p-n HOMOJUNCTION DIODE

A p–n homojunction is formed between two semiconductor regions of opposite doping types and of a single semiconductor. This can be depicted by bringing two oppositely doped regions together and aligning their conduction and valence band energies (fig. 3.1). It is assumed that the n- and p-doped regions are uniformly doped and the transition between the two regions is abrupt (abrupt p–n junction).

The majority carriers, electrons in n-type region and holes in p-type region, close near the junction diffuse across it (fig. 3.1(a) and (d)). The electrons diffuse into the p-type region, whereas the holes diffuse into the n-type region, and while interacting with each other they recombine. Thus, this leads to the formation of a region (around the junction) that is depleted of mobile carriers and is called depletion region W (fig. 3.1(c)). As a result of this diffusion of electrons and holes across the junction, the immobile ionized donors and acceptors in n- and p-type regions are no longer compensated, resulting in the formation of space–charge regions near the junction. This is associated with the concentrations of acceptor N_A and donor N_D ions, which produce a net negative charge on the p-type side of the junction and a net positive charge on the n-type side, respectively. Such a build-up of oppositely charged regions results in the formation of the junction potential, which effectively prevents further migration of majority carriers. Any majority carrier, entering the depletion region, is experiencing a force that pushes it back away from the depletion region. The presence of uncompensated charge due to the ionized donors and acceptors produces an electric field that results in a drift of minority carriers (electron and hole minority carriers in the p- and n-type region respectively) in the opposite direction (fig. 3.1(a) and (d)).

The internal (built-in) potential V_{bi} is essentially formed as the result of the Fermi energy difference between the n- and p-type regions (fig. 3.1(d)). In the thermodynamic equilibrium (no voltage bias is applied), the Fermi level (which is near the valence band edge in a p-type region and near the conduction band in an n-type region) of a p–n junction must be constant across the junction, which necessitates the band bending through the junction (fig. 3.1(b)). The equilibrium built-in voltage is related to the difference in the Fermi levels, of the two semiconductors, prior to their equalization, i.e. $eV_{bi} = E_{Fn}-E_{Fp}$.

In order to move across the depletion region, majority carriers require extra energy to overcome the forces of the space–charge region. Such a barrier, which is equal to qV_{bi}, is depicted in fig. 3.1(d) as band bending of the conduction and valence bands in the depletion region. Such a depiction represents the condition of the electrons that now have to “move uphill” in order to traverse across the depletion region from the *n*-type side to the *p*-type side.

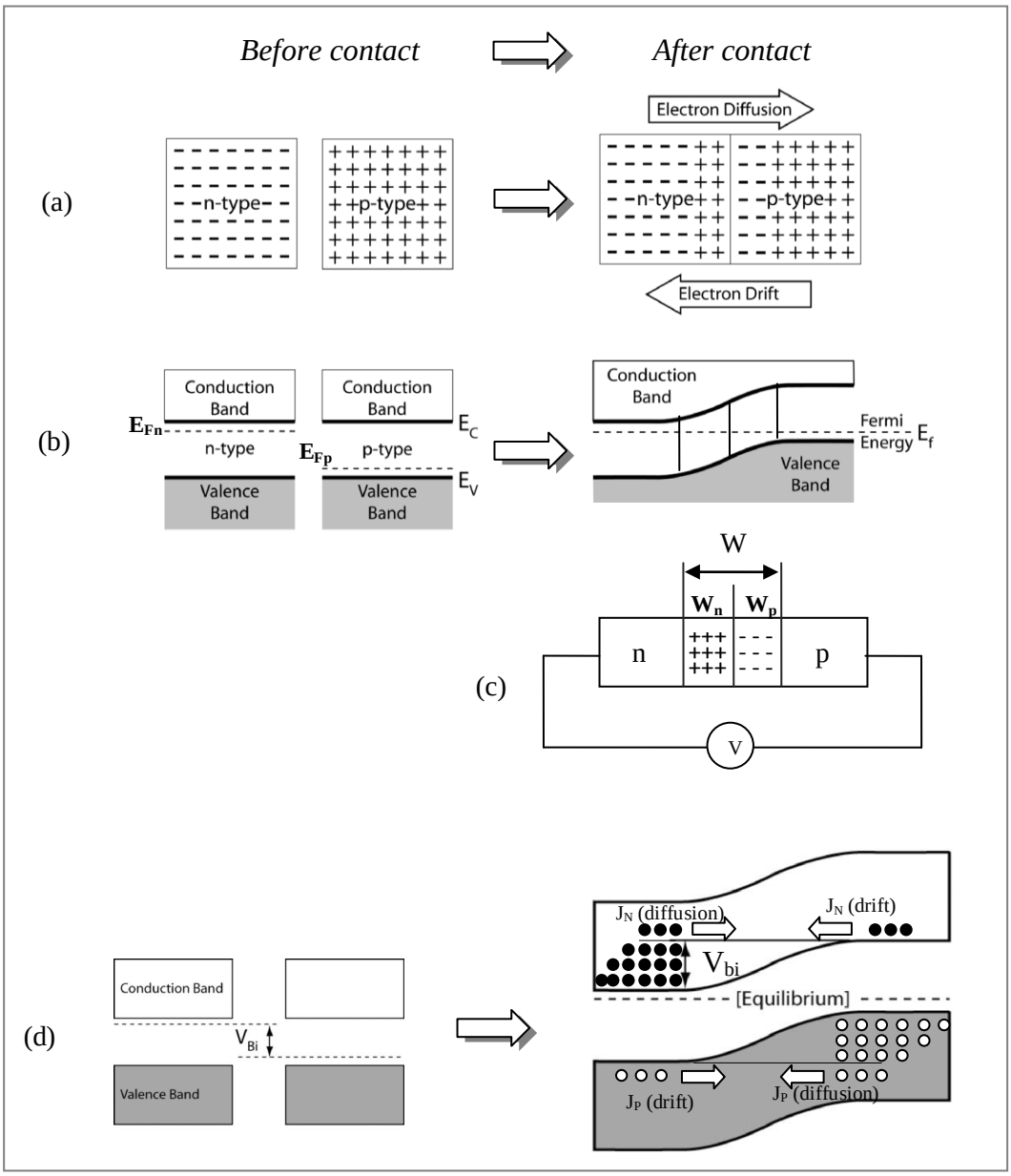

Fig. 3.1: Schematic illustration of the p-n junction; (a) before the contact of the materials and after contact where electrons and holes diffuse across the junction, (b) energy band diagram of a p- and n-type semiconductor before and after the junction formation (in thermal equilibrium), (c) a p-n junction showing the depletion region or space-charge region W, and (d) the difference in Fermi energies (dashed lines) before contact establishes a band edge bending, carrier flux and a contact potential V_{bi} after contact (most of the figures adopted from [6]) .

The opposite is for holes. Thus, majority carriers require energy to traverse across the depletion region; this can be accomplished by the application of a voltage between the two ends of the p–n junction diode (fig. 3.1(c)). However, depending on polarity, the application of such a voltage may either assist in overcoming the barrier, or vice versa. This effectively results in a rectifying characteristic of a diode, which allows the flow of electrical current in one direction but not in the other. This depends on the forward-bias or reverse-bias conditions of such a diode.

Consider the n-region to be grounded and voltage *V* is applied to the p-region.

If *V* is positive, i.e. the junction is *forward biased*, the potential barrier to majority carriers at the junction is reduced, from qV_{bi} to $q(V_{bi} - V)$ (fig. 3.2(b)). The majority carriers are pushed towards the edges of the depletion region where they neutralize some of the space-charge resulting in the reduction of the magnitude of the electric field and the narrowing of the depletion region. Because of the reduction of the barrier height more majority carriers are able to diffuse on the other side resulting in an increase in the diffusion current. While the drift current remains the same, since a change in barrier height has no effect in the number of minority carriers drifting down the potential hill. As the forward bias voltage increases, the forward current will increase at approximately an exponential rate, and can become very large.

If *V* is negative, i.e. the junction is *reversed biased*, the potential barrier to majority carriers at the junction is increased, from qV_{bi} to $q(V_{bi} + V)$ (fig. 3.2(c)). The majority carriers are pulled away from the edges of the depletion region, which therefore widens, and it is more difficult for them to traverse the depletion region. There is very little current flow, since the bias polarity aids the transfer of the minority carries which are low in density.

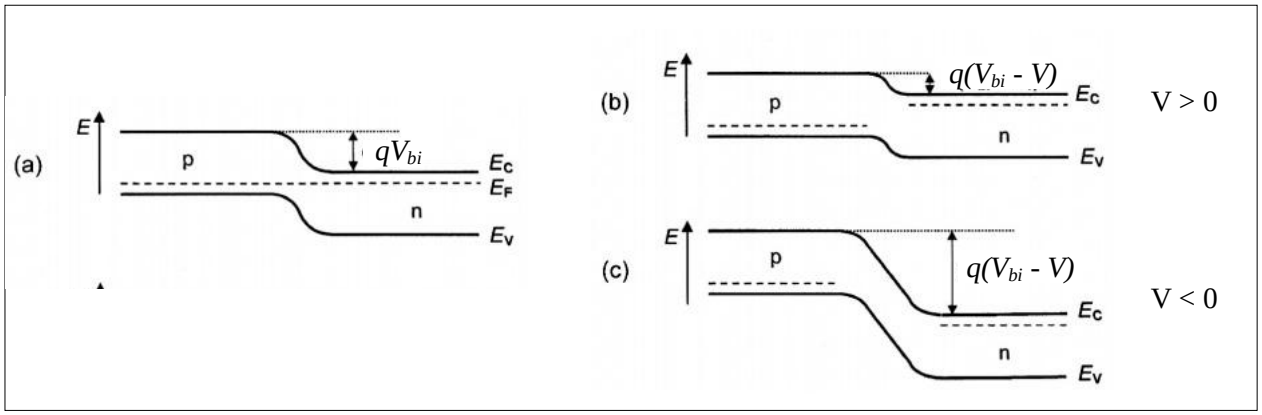

Fig. 3.2: Schematic illustration of the energy band diagrams of a p-n junction (a) in equilibrium, (b) under forward bias, and (c) under reverse bias.

From the analysis of the flow of charge carriers across the p–n junction and from the charge neutrality condition for the abrupt junction, one can derive analytical relationships for the diode in equilibrium. In this case, the total current is zero (i.e., the net current across the junction due to both electrons and holes is zero), as the diffusion current and drift current are equal and opposite and, thus, they cancel each other out. When the diode is biased the total current is given by

$$I = I_o\left(e^{qV/kT} - 1\right) \qquad (eq.3.1)$$

where I_o is the reverse saturation current supplied by the thermally generated minority carriers and independent of V after a few tenths of a volt of reverse bias. Further increases in the amount of reverse bias voltage have no effect on the minority carrier supply. I_o is defined as

$$I_o = qAn_i^2\left[\frac{D_N}{L_N N_A} + \frac{D_P}{L_P N_D}\right]$$

where A is the area of the junction, n_i the intrinsic concentration, D_N and D_P are the diffusion constants of electrons and holes, L_N and L_P are the diffusion lengths of electrons and holes, and N_D and N_A the donor and acceptor concentration of the n- and p-type region, respectively.

The expression for the depletion width for the case of a biased diode is defined as

$$W = w_n + w_p = \left(\frac{2\epsilon(V_{bi} - V)}{q}\ \frac{N_A + N_D}{N_A N_D}\right)^{1/2} \qquad (eq.3.2)$$

where ϵ is the dielectric constant of the material. The penetration of the transition region into the n and p materials, as a consequence of the balanced charge requirement $w_n N_D = w_p N_A$ and the equality $W = w_n + w_p$, is

$$w_n = W\frac{N_A}{N_A + N_D} = \left(\frac{2\epsilon(V_{bi} - V)}{q}\ \frac{N_A}{N_D(N_A + N_D)}\right)^{1/2}$$

$$and \qquad w_p = W\frac{N_D}{N_A + N_D} = \left(\frac{2\epsilon(V_{bi} - V)}{q}\ \frac{N_D}{N_A(N_A + N_D)}\right)^{1/2}$$

Due to the charge separation in the depletion region (i.e., the presence of two layers of space charge in the depletion region), it behaves like a capacitor, and the (junction) capacitance per unit area can be expressed as

$$C = \frac{\epsilon}{W} = \epsilon\left(\frac{2\epsilon}{q}\ \frac{N_A + N_D}{N_A N_D}\right)^{-\frac{1}{2}} \frac{1}{(V_{bi} - V)^{\frac{1}{2}}} \qquad (eq.3.3)$$

In the case of an asymmetrically doped junction, the depletion layer extends primarily into the less doped side, and the capacitance is determined by the doping concentration of the less doped side.

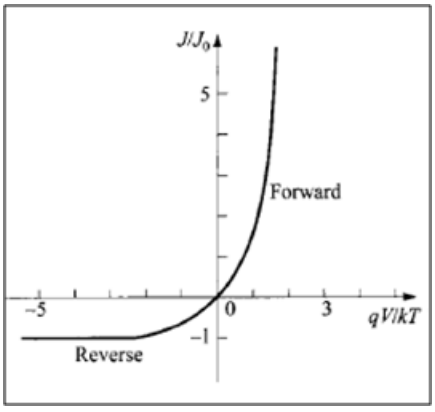

Fig. 3.3: Ideal current-voltage characteristics.

The equations above refer to the ideal diode. Several conditions of applied voltage and/or temperature exist where the ideal diode fails to adequately represent physical devices. When reverse biased, the current can become more negative than $-I_o$ as a result of generation of carriers in the depletion region, and at even larger reverse voltages due to junction breakdown. Breakdown is due to one of two phenomena: avalanching or Zener process. Forward bias deviations for the ideal occur at very small currents due to recombination in the depletion region. At high currents deviations occur due high level carrier injection and at higher currents due to ohmic voltage drops in the bulk regions and contacts. The two latest effects are usually combined into a resistor R_S, the series resistance. For many decades of current the ideal and the real device are really very close. The parameter "*n*" is called the ideality factor and is a measure of how close to ideal were the conditions under which the physical device was fabricated. The ideality factor is incorporated to the ideal equation by replacing *q/kT* by *q/nkT*,

$$I = I_o\left(e^{qV/nkT} - 1\right) \qquad (eq.\,3.4)$$

Deviation of *n* from unity, which corresponds to the ideal value, may be attributed to a number of factors such as large surface leakage current, high density of bulk recombination centers in the depletion region, and high interface state density as well as high series resistance.

3.3 p-n HETEROJUNCTION DIODE

A Heterojunction is a junction formed between two dissimilar semiconductors. When the two semiconductors have the same type of conductivity, the junction is called an isotype heterojunction (*n–n* or *p–p* junctions). When the conductivity types differ, the junction is called an anisotype heterojunction (*p–n* heterojunctions) which is a much more useful and common structure than its counterpart. A brief description of the anisotype heterojunction is followed.

The energy-band model of an idealized anisotype abrupt heterojunction without interface traps was proposed by Anderson[7] based on the previous work of Shockley[8]. This model is considered next, since it can adequately explain most transport processes, and only slight modification of the model is needed to account for non-ideal cases such as interface traps. Figs 3.4 (a) and (c) show the energy-band diagrams of two isolated semiconductors of opposite types. The two semiconductors are assumed to have different bandgaps E_g, different permittivities ϵ, different work functions Φ_m, and different electron affinities χ. Work function and electron affinity are defined as the energy required to remove an electron from the Fermi level E_F and from the bottom of the conduction band E_C, respectively, to a position just outside the material (vacuum level). The difference in energy of the conduction-band edges in the two

semiconductors is represented by ΔE_C, and that in the valence-band edges by ΔE_V. The electron affinity rule ($\Delta E_C = q\Delta\chi$) shown in fig. 3.4 may not be a valid assumption in all cases. However, by choosing ΔE_C, as an empirical quantity, the Anderson model remains satisfactory and unaltered.

When a junction is formed between these semiconductors, the energy-band profile at equilibrium is as shown in fig. 3.4 (b) for an n-p anisotype heterojunction where, in this example, the narrow-bandgap material is n-type. Since the Fermi level must coincide on both sides in equilibrium and the vacuum level is everywhere parallel to the band edges and is continuous, the discontinuity in the conduction-band edges ΔE_C and valence-band edges ΔE_V is invariant with doping in those cases where E_g and χ are not functions of doping (i.e., nondegenerate semiconductors).

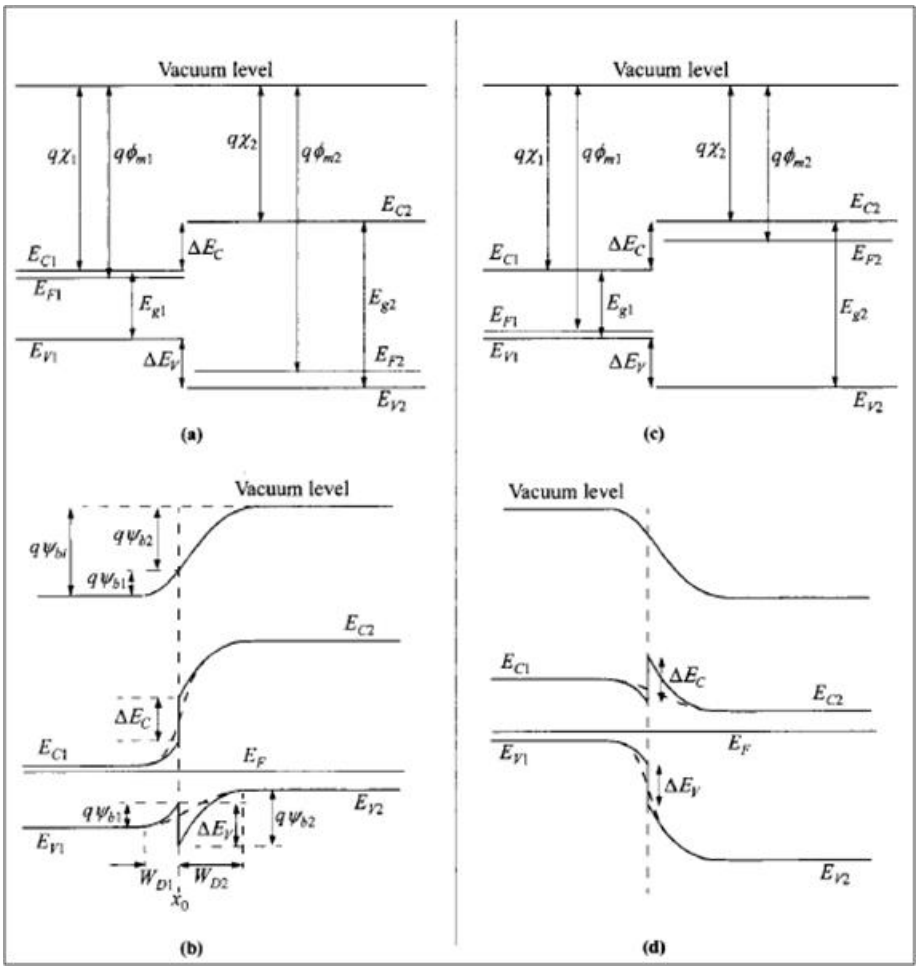

Fig. 3.4: Energy-band diagrams for (a) two isolated semiconductors of opposite types and different E_g (of which the smaller band gap is n-type) and (b) their idealized anisotype heterojunction at thermal equilibrium. In (c) and (d), the smaller band gap is p-type. In (b) and (d), the dashed lines across the junctions represent graded composition. (Figure adopted from [4])

The total built-in potential Ψ_{bi} is equal to the sum of the partial built-in voltages ($\Psi_{b1} + \Psi_{b2}$), where Ψ_{b1} and Ψ_{b2} are the electrostatic potentials supported at equilibrium by semiconductors 1 and 2, respectively[ii]. From fig. 3.4, it is apparent that since at equilibrium, $E_{F1} = E_{F2}$, the total built-in potential is given by $\Psi_{bi} = |\Phi_{m1} - \Phi_{m2}|$. The depletion widths and capacitance can be obtained by solving the Poisson equation for the step junction on either side of the interface. When the applied total voltage is V, the depletion region on each type and the total depletion region are

$$W_{D1} = \left[\frac{2N_{A2}\epsilon_1\epsilon_2(\Psi_{bi} - V)}{qN_{D1}(\epsilon_1 N_{D1} + \epsilon_2 N_{A2})}\right]^{1/2} \quad , \quad W_{D2} = \left[\frac{2N_{D1}\epsilon_1\epsilon_2(\Psi_{bi} - V)}{qN_{A2}(\epsilon_1 N_{D1} + \epsilon_2 N_{A2})}\right]^{1/2}$$

and

$$W = W_{D1} + W_{D2} = \left[\frac{2\epsilon_1\epsilon_2(\Psi_{bi} - V)(N_{D1} + N_{A2})^2}{qN_{D1}N_{A2}(\epsilon_1 N_{D1} + \epsilon_2 N_{A2})}\right]^{1/2}$$

The junction capacitance per unit area can be expressed as

$$C = \sqrt{\frac{\epsilon_1\epsilon_2}{W}} = \left[\frac{qN_{D1}N_{A2}\epsilon_1\epsilon_2}{2(\epsilon_1 N_{D1} + \epsilon_2 N_{A2})(\Psi_{bi} - V)}\right]^{1/2} \qquad (eq.\,3.4)$$

The relative voltage supported in each semiconductor is

$$\frac{V_{b1} - V_1}{V_{b2} - V_2} = \frac{N_{A2}\epsilon_2}{N_{D1}\epsilon_1}$$

Where $V=V_1+V_2$. It is apparent that the foregoing expressions will reduce to the expression for the p-n Homojunction when both sides of the heterojunction become the same material. Considering the current flow, the example in fig. 3.4(b) shows that the band edge E_C, increases monotonically while the valence-band edge E_V, goes through some peak near the junction. The hole current could become complicated because of the added barrier which might present a bottle-neck in thermionic emission, in series with diffusion. The analysis can be greatly simplified by assuming a graded junction where ΔE_C and ΔE_V become smooth transitions inside the depletion region. With this assumption, the diffusion currents are similar to a regular p-n junction but with the appropriate parameters in place. And so the total current becomes:

$$J = J_N + J_P = \left(\frac{qD_{N2}n_{i2}^2}{L_{N2}N_{A2}} + \frac{qD_{P1}n_{i1}^2}{L_{P1}N_{D1}}\right)\left[exp\left(\frac{qV}{kT}\right) - 1\right]$$

The band offsets ΔE_C and ΔE_V are not in this equation, and also each diffusion current component depends on the properties of the receiving side only, as in the case of a homojunction.

[ii] The convention is to list the material with the smaller bandgap as the first symbol

3.4 REFERENCES

[1] W. Shockley, “The Theory of *p-n* Junctions in Semiconductors and *p-n* Junction Transistors,” Bell Syst. Tech. J., 28,435 (1949)

[2] W. Shockley, Electrons and Holes in Semiconductors, D. Van Nostrand, Princeton, New Jersey, 1950

C. T. Sah, R. N. Noyce, and W. Shockley, “Carrier Generation and Recombination in *p-n* Junction andp-n Junction Characteristics,” Proc. IRE, 45, 1228 (1957)

[3] J. L. Moll, “The Evolution of the Theory of the Current-Voltage Characteristics of *p-n* Junctions,” Proc. IRE, 46, 1076 (1958)

[4] Kwok K. Ng and S. M. Sze, “Physics of Semiconductor Devices”, John Wiley & Sons (2007)

[5] B. G. Yacobi, ”Semiconductor Materials; An introduction to Basic Materials”

[6] A. Rockett, “The Materials Science of Semiconductors”, Springer (2008)

[7] R. L. Anderson, Solid-state Electron., 5, 341 (1962)

[8] W. Shockley, US. Patent 2, 569, 347 (1951)

CHAPTER 4
EXPERIMENTAL PROCEDURE

4.1 EXPERIMENTAL SET-UP AND PROCEDURE OF THE PLD TECHNIQUE

The PLD set-up is presented in fig. 4.1. The laser beam is directed into the vacuum chamber and is focused through a coated lens on the surface target to a spot size of about 4.2 to 4.5 mm^2. The lens was plano-convex, had a +350 mm focal length and was placed (outside the vacuum chamber) at a position that the focal point was approximately at the surface target. After the strike of the focused beam on the surface target, the ablated material was deposited on the substrate placed parallel, at 40mm in front of the surface target. Before each film deposition, the laser pulse energy was measured with a laser power meter. In order to achieve the desired pulse energy, the laser beam was attenuated by an attenuator positioned in the beam way.

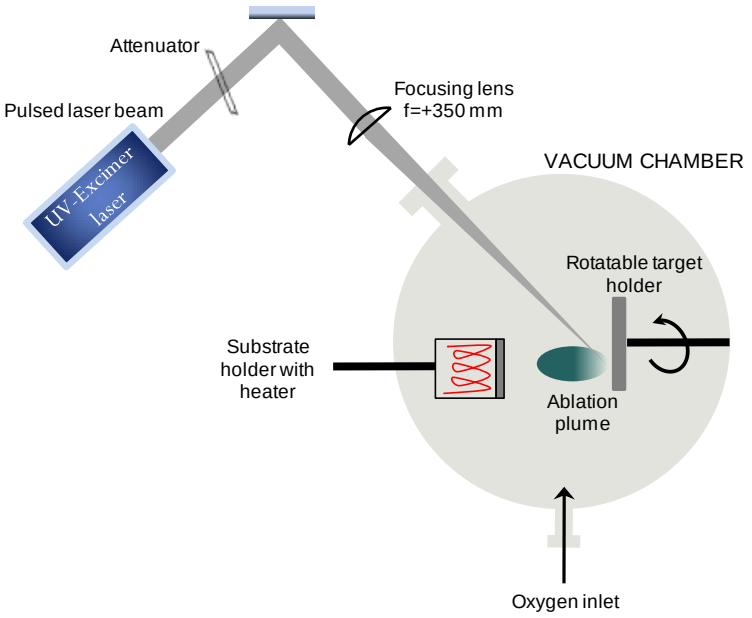

Fig. 4.1: Experimental set-up of the pulsed deposition technique

The two lasers used for the ablation process were an LPX 200 excimer laser Lambda Physik which uses KrF gas mixture for the production of a laser beam at 248 nm, and an LPX 300 excimer laser Lambda Physik which uses XeCl gas mixture for the production of a laser beam at 308nm wavelength. Both of the lasers had nominal pulse duration of 34 ns, with pulse energy 600 mJ maximum and during the ablation were operating at a repetition rate of 10 Hz. The intensity profile of the laser beam was "top hat" along the horizontal axis and Gaussian along the vertical axis.

The vacuum chamber was evacuated utilizing two vacuum pumps. Initially, using a diffusion pump the vacuum chamber was evacuated at 1.3×10^{-3} mbar and afterwards a turbo-molecular rotary pump was used to achieve vacuum of the order of 10^{-7} mbar. The pressure of the chamber was measured by two vacuum gauges, a Pirani gauge (measured pressure range 10^{-3} to 10^{3} mbar) and a Penning gauge (measured pressure range 10^{-8} to 10^{-3} mbar). Film deposition was typically performed in an oxygen ambient background gas, with a pressure ranging from 6×10^{-5} up to 2.5×10^{-3} mbar.

The laser beam was focused on the target at an angle of about 45° in order to reduce the laser-plasma interaction and avoid any laser-substrate interaction. In order to avoid repeated ablation for long time and from the same spot on the target, the target was rotated using a motor inside the chamber. In this way crater formation is avoided. In order to avoid the reduction of the deposition rate the targets were resurfaced, by polishing, before each deposition. Furthermore pre-ablation, immediately before film deposition, was necessary in order to obtain steady state laser ablation and to avoid the deposition of the ablated material from the first layers of the target, which can contain contaminants. For the pre-ablation, the targets were irradiated with 200-300 pulses and a shutter was interposed between the substrate and the target, preventing the traveling ablated material reaching the substrate. To grow a multi-layer sample in situ, a rotatable multi-target carousel was used. The manufacturing of the PLD targets were done by Umicore.

Since the ablated material is ejected as a highly forward-directed plume along the target normal, the substrate was held directly opposite the target. The optimal target-to-substrate distance mainly depends on the energy delivered to the target (higher beam energies permit larger distances to be used) and the desired deposition rate (increasing the distance the deposition rate reduces).

The substrates were mounted on a heating holder. The substrate holder could be heated from room temperature up to 700°C so that to produce good adhesion and to favor the better crystallinity of the films. A Kanthal *A* wire was used for the heating of the substrate, highly

resistive to oxidization. The temperature was adjusted by changing the current supply and was measured continuously by a thermocouple. After the termination of each deposition the sample was cooled to room temperature at the same oxygen partial pressure as during deposition.

The used substrates were n-type Si ((001) oriented, 1-10Ωcm, ~$10^{15}$$cm^{-3}$), fused silica and fused silica coated with ITO. All substrates were ultrasonically cleaned prior to deposition; initially dipped for 15 min in acetone, afterwards dipped for 15 min in 2-propanol, then dipped for 15 min in deionized water and finally dried with nitrogen flow.

4.2 CHARACTERIZATION OF THE FILMS

4.2.1 PROFILOMETER

The determination of the films' thickness was made by a Stylus profilometer (alpha-step 100 Tencor). The profilometer measures the vertical depth of a material across a specified horizontal length. A small needle, called stylus, is moved across the surface of interest and generates a profile based on the deflection of the needle.

4.2.2 UV-VIS-NIR SPECTROPHOTOMETER

The optical properties of the films were studied by UV-Vis-NIR Reflectance & Transmittance using a PerkinElmer Lambda 950 spectrophotometer at the 250-2000 nm spectrum range. Information about the electronic structure of the films could be extracted from the spectra and a general idea of the carriers' concentration could be obtained. Furthermore, the absorption and the optical energy band gap of the films could be calculated.

In general, there are several optical absorption processes[i], and each of these contributes to the total absorption coefficient. These mechanisms include:

(i) fundamental absorption process, where a photon excites an electron from the valence band (VB) to the conduction band (CB) and both energy and momentum must be conserved,

(ii) exciton absorption, which is observed at energies which are slightly lower than the energy gap of a semiconductor due to the fact that the excitonic states are at energies just below the CB, and they can exist in a series of bound states in the gap.

(iii) absorption due to dopants, observed as shoulders on the low-energy region of the absorption edge. This absorption occurs as a result of transitions between impurity and band states, i.e.

[i] "Semiconductor Materials", ed. by B. G. Yacobi, (2003) Kluwer

acceptor level-to-CB and VB-to-donor level, as well as transitions between donor level-to-CB and VB-to-acceptor level that result in absorption in the far infrared region.

(iv) absorption due to imperfections. Imperfections (e.g., point defects, impurities, dislocations, and grain boundaries) introduce localized energy levels in the energy gap of a semiconductor. In this case, electronic transitions are from occupied imperfection levels to the CB or from the VB to the unoccupied imperfection levels. Absorption between two imperfection levels may also occur.

(v) absorption due to intraband transitions, is due to the presence, in most semiconductors, of the VB with separated light-hole (LH) and heavy-hole (HH) bands, as well as the split-off band. This inter-valence band absorption is due to the electron transitions between the split-off band and LH and HH bands, as well as between LH and HH bands.

(vi) free carrier absorption, which is due to the transitions to higher energy levels, within the same energy band, resulting in absorption continuum at lower energies. This case of optical absorption requires the participation of a photon and a phonon for the change in both the energy and momentum of the carrier during the transition. Thus, this interaction results in an energy loss from the EM wave to the lattice vibrations through the carrier scattering processes.

Consider the sample of fig. 4.2, characterized by reflection coefficients R_1, R_2, absorption coefficient α, complex refractive index $(n_1\text{-}jk_1)$ and thickness d. Light of intensity I_i and wavelength λ is incident from the left. $I_{r1}=R_1I_i$ is reflected at point A and $(1\text{-}R_1)I_i$ is transmitted into the sample where it is attenuated as it traverses the sample. At point B, just inside the sample at $x=d$, the intensity is $(1\text{-}R_1)exp(-\alpha d)I_i$. The fraction $R_2(1\text{-}R_1)exp(-\alpha d)I_i$ is reflected back into the sample at point B and the fraction $I_{t1}=(1\text{-}R_2)(1\text{-}R_1)exp(-\alpha d)I_i$ is transmitted through the sample.

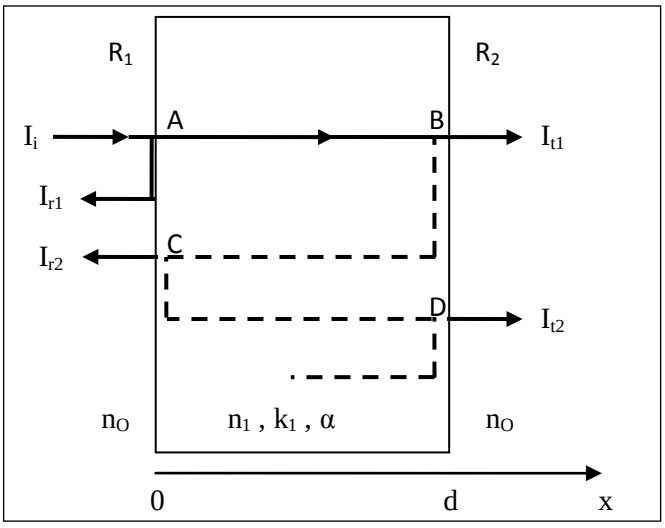

Fig. 4.2: Schematic showing the various reflected and transmitted components.

Some of the light reflected at B is reflected back into the sample at C and the component I_{r2} is back-reflected. As shown in the figure, light is reflected back and forth and each time some of it is reflected and some is transmitted. When all components are summed, it can be shown that the transmittance T is given by

$$T = \frac{I_t}{I_i} = \frac{(1-R_1)(1-R_2)e^{-ad}}{1 + R_1R_2e^{-2ad} - 2\sqrt{R_1R_2}e^{-ad}\cos(\varphi)}$$

where $\varphi = 4\pi n_1 d/\lambda$. If the detector does not have sufficient spectral resolution, then the oscillations due to the $cos(\varphi)$ term average to zero. The effect of the reduced resolution can be calculated by averaging the transmitted intensity over a period of the cosine term as

$$T = \frac{1}{2\pi}\int_{-\pi}^{\pi} \frac{(1-R)^2e^{-ad}}{1 + R^2e^{-2ad} - 2Re^{-ad}\cos(\varphi)}\, d\varphi$$

where it has been assumed that the sample is symmetrical, i.e. the reflectance is $R_1=R_2=R$. Assuming, further, that α and n_1 are constant over the wavelength integral, transmittance becomes

$$T = \frac{(1-R)^2e^{-ad}}{1 - R^2e^{-2ad}}$$

The absorption coefficient from the above equation is:

$$\alpha = -\frac{1}{d}ln\left(\frac{\sqrt{(1-R)^4 + 4T^2R^2} - (1-R^2)^2}{2TR^2}\right) \qquad (4.1)$$

For the absorption process the density of states $N(E)$ is of importance, where E is the energy. The absorption coefficient, related to the absorption transitions between direct parabolic bands (fig. 4.3), can be expressed as

$$a(h\nu) = A\sum P_{if}n_in_f$$

where ν is the frequency of the incident photon, P_{if} is the transition probability, n_i and n_f are the densities of the electrons in the initial state and of empty energy levels in the final state, respectively, and the sum is over all initial and final states.

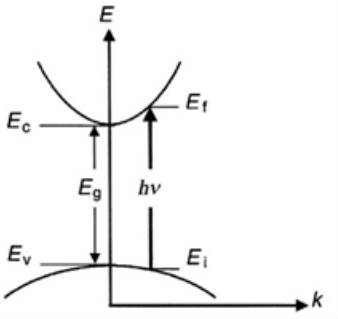

Fig. 4.3: Absorption transition, between direct parabolic bands, from energy level E_i to energy level E_f.

As a result of the conservation of the energy, the transition energy can be expressed as

$$hv = \frac{\hbar^2 k^2}{2m_e^*} + \frac{\hbar^2 k^2}{2m_h^*} + E_g \qquad \Rightarrow \qquad hv - E_g = \frac{\hbar^2 k^2}{2m_r^*}$$

where $m_r^* = m_e^* m_h^* / (m_e^* + m_h^*)$ is the reduced effective mass. The general expression for the density of states is $N(E)dE = (2\pi^2\hbar^3)^{-1}(2m^*)^{3/2}E^{1/2}dE$, and for the present case it can be written as: $N(hv)d(hv) = (2\pi^2\hbar^3)^{-1}(2m_h^*)^{3/2}\left(hv - E_g\right)^{1/2}d(hv)$

Thus, for direct transitions between parabolic valence and conduction bands, the absorption coefficient as a function of the photon energy is

$$ahv = A\left(hv - E_g\right)^{1/2} \qquad (4.2)$$

where *A* is a constant (no depend of the frequency), the energy gap E_g and *hv* are in *eV*, and α is in cm^{-1}. For direct band gap semiconductors, plotting α^2 against *hv* the optical band gap E_g is determined from the extrapolated intercept. Such a plot is sometimes referred to as Tauc plot.

For indirect band gap materials, the transition process requires the involvement of an extra particle (i.e., phonon) as compared with the direct transition. Thus, the probability of the absorption of light (and hence the absorption coefficient) in this case is much lower than in direct-gap materials. This implies that light has to travel a large distance into the material before being absorbed. For indirect band gap semiconductors, plotting $\alpha^{1/2}$ against *hv* the optical band gap E_g is determined from the extrapolated intercept.

4.2.3 X-RAY DIFFRACTION

X-ray diffraction (XRD) measurements were performed using a Rigaku D/MAX-2000H rotating anode (12 kW) Cu Kα monochromated diffractometer, with 1.5405 Å X-ray wavelength, at the diffracted angle range of 20-90°. Because the wavelength of x-rays is comparable to the size of atoms, they are ideally suited for probing the structural arrangement of atoms and molecules in a wide range of materials. The energetic x-rays can penetrate deep into the materials and provide information about the bulk structure.

X-rays primarily interact with electrons in atoms. When x-ray photons collide with electrons, some photons from the incident beam will be deflected away from the direction where they original travel. If the wavelength of these scattered x-rays did not change, i.e. did not lose any energy, the process is called elastic scattering and only momentum has been transferred in the scattering process. These are the x-rays that are measured in diffraction experiments, as the scattered x-rays carry information about the electron distribution in materials. On the other hand, in the inelastic scattering process, x-rays transfer some of their energy to the electrons and the scattered x-rays will have different wavelength than the incident x-rays.

Diffracted waves from different atoms can interfere with each other and the resultant intensity distribution is strongly modulated by this interaction. If the atoms are arranged in a periodic way, as in crystals, the diffracted waves will consist of sharp interference maxima (peaks) with the same symmetry as in the distribution of atoms. Measuring the diffraction pattern therefore allows deducing the distribution of atoms in a material.

The peaks in a XRD spectrum are directly related to the atomic distances. Consider an incident monochromatic x-ray beam interacting with the atoms arranged in a periodic manner as shown in fig. 4.4 in 2-D. The atoms can be viewed as forming different sets of planes in the crystal. The path difference for rays reflected from a given set of lattice plane, with an inter-plane distance of d, is $2d \sin\theta$, where θ is measured from the plane. Constructive interference of the radiation reflected from successive planes occurs whenever the path difference is an integral number (n) of wavelengths λ of the x-ray. Thus the condition for constructive reflection of the incident radiation is:

$$2d \sin\theta = n\lambda \qquad (4.3)$$

which is known as the Bragg's law. So the above relation describes the condition for a diffraction peak.

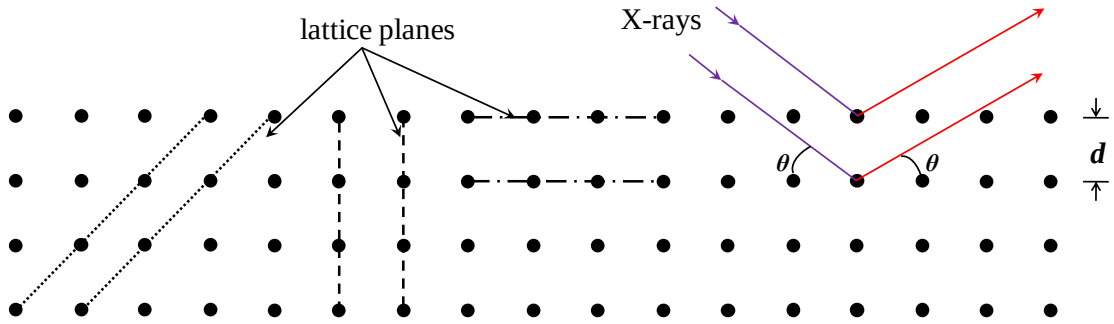

Fig. 4.4: Sets of lattice planes in the crystal (different kind of lines different planes, on the left) and Bragg's diffraction condition (on the right).

From the XRD spectra the lattice parameters can be calculated and the quality of the crystals of the materials can be defined. Due to crystal disorders a diffraction angle can differ from the ideal one. Such disorders can be the strain effect, due to thermal expansion coefficient mismatch between the film and the substrate, internal stress and different stoichiometry from the expected one. It can also be determined whether the material is amorphous, pollycrystalline or monocrystal, through the definition of the orientation derived from the XRD analysis. Furthermore the crystallite size can be measured according to Scherrer's formula[ii]:

[ii] A. L. Patterson, Phys. Rev., 56, 978-982 (1939)

$$d_g = \frac{0.9\lambda}{\beta \cos \vartheta_\beta} \qquad (4.4)$$

where d_g is the crystallite size, λ is the wavelength of the X-ray beam (for the specific experiment the wavelength of the X-ray beam used was *1.5405Å*), β is the full width at half maximum (FWHM) of the diffracted peak with peak angle θ_β, in radians. Small crystallite size can be considered as a kind of defect and can alter diffraction peak widths. Very small crystals cause peak broadening.

For this study, the XRD measurements were made by *θ-2θ* scan, where *θ* is the angle between the incident beam and the surface of the sample and *2θ* is angle between the incident beam and the reflected beam which arrive at the detector (as shown in fig. 4.5). During the measurement the *2θ* is always two times *θ*. After each measurement, the derived data were modified in order to eliminate the *Kα1* absorption.

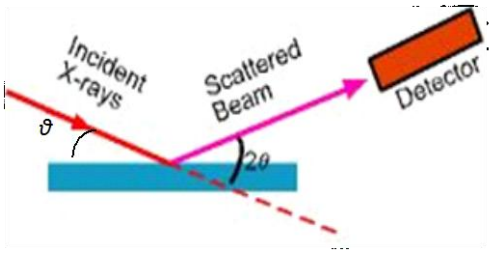

Fig. 4.5: XRD θ-2θ scan

4.2.4 ELECTRICAL MEASUREMENTS

The electrical properties of the films, i.e. resistivity (ρ), carriers' mobility (μ) and concentration (N_D or N_A), were studied by standard resistivity and Hall effect set – ups in the Van der Pauw configuration using indium for the electrical contacts, at room temperature. The measurements performed by E. Chikoidze, in GEMaC of France.

The carrier mobility is determined by random scattering processes, among which the main mechanisms in semiconductors include impurity scattering and the intrinsic phonon (lattice) scattering. Impurity scattering sources include both the ionized and neutral donor and acceptor atoms that are used to dope the semiconductor to the desired conductivity level. In general, impurity scattering may also arise due to unintentionally introduced impurities and native defects and their complexes. The intrinsic scattering mechanisms may also include, besides phonon scattering, carrier–carrier scattering. Typically, carrier–carrier scattering may have a significant contribution only in heavily doped semiconductors under degenerate conditions or under high-field conditions. In general, ionized impurity scattering and phonon

scattering are dominant electron scattering mechanisms in practical semiconductors. It should be noted that higher doping concentrations result in increased scattering (and lower mobilities) of the carriers by the ionized impurities.

4.3 Rapid Thermal Annealing (RTA)

A few samples underwent rapid thermal annealing (RTA) in order to achieve better crystal quality. A Fav4 RTA aperture of the Jipelec company was used. The RTA used had 10 incandescent lamps of 500W. The RTA aperture consisted of a vacuum chamber which used a mechanical and a turbo pump to achieve vacuum of the order of 10^{-6} mbar. During thermal annealing there was flow of gas mixture which consists of 95% N_2 and 5% H_2 forming gas. According to the type of the sample substrate a suitable holder is used. The temperature of the sample holder was controlled by a thermocouple or a pyrometer.

CHAPTER 5
PULSED LASER DEPOSITION OF UN-DOPED AND Al-DOPED ZnO THIN FILMS

5.1 INTRODUCTION

This chapter presents the results derived from the characterization of the un-doped and the Aluminum-doped ZnO thin films, which were grown by pulsed laser deposition. A comparative study of the properties of the films is made as a function of the substrate temperature (between 200 and 500°C) and the ambient oxygen pressure (between $6x10^{-5}$ and $1x10^{-3}$ mbar). The films were studied according to their structural, optical and electrical properties which were determined by X-ray diffraction, UV-NIR Reflectance and Transmittance, and Hall Effect measurements, respectively.

5.2 EXPERIMENTAL CONDITIONS

ZnO and ZnO:Al (98wt.% ZnO+2wt.% Al_2O_3) were the two targets used for the ablation and were delivered by Umicore (target #; TA050 (ZnO) and TA014 (ZnO:Al(2%))).

The pulsed laser used for the fabrication of the ZnO and ZnO:Al films was the KrF excimer with 248 nm wavelength and 34 ns pulse duration. The density of the laser energy on the surface target was 1.5 J/cm^2 per pulse. For each deposition 3000 or 4000 pulses were used to strike the target at a repetition rate of 10 Hz.

The base pressure prior to deposition was better than 10^{-6} mbar. All depositions were realized in an oxygen ambient atmosphere at a steady pressure. The ablated material was delivered on heated UV-graded fused silica substrates, which have an amorphous structure. The thicknesses of the thin films measured between 100 and 300 nm. The deposition parameters are presents in Table 5.1.

Table 5.1: experimental conditions for the growth of ZnO and ZnO:Al thin films by PLD

Substrate type Substrate – target distance	UV-graded fused silica (15x15x1 mm) 4 cm
Laser parameters	λ=248 nm, τ =34 ns, F=1.5 J/cm^2 3000 or 4000 pulses/deposition, r.r.=10 Hz
Ambient oxygen pressure (Po_2) (mbar) at a substrate temperature of 300°C	$5x10^{-5}$, $5x10^{-4}$, $1x10^{-3}$, $2.5x10^{-2}$ (ZnO films) $6x10^{-5}$, $1x10^{-4}$, $2.5x10^{-4}$, $5x10^{-4}$, $1x10^{-3}$ (ZnO:Al films)
Substrate temperature (T_S) (°C) at an ambient oxygen pressure of $5x10^{-4}$ mbar	200, 300, 500 (ZnO films) 200, 250, 300, 400, 500 (ZnO:Al films)

5.3 Structural Properties

The crystal structure of the films was studied by X-ray diffraction. Figures 5.1 and 5.3 show the effect of oxygen pressure (Po_2) on the crystallinity of the ZnO and the ZnO:Al films at a substrate temperature of 300°C, respectively. Figures 5.2 and 5.4 show the effect of substrate temperature (Ts) on the crystallinity of the ZnO and the ZnO:Al films at an ambient oxygen pressure of $5x10^{-4}$ mbar, respectively.

As can be seen from the figures, the ZnO and ZnO:Al thin films have polycrystalline structure, with c-axis preferred orientation along [001] direction (normal to the substrate) and the (002) crystal orientation dominant, indicating the growth of the wurtzite structure. The (002) diffraction peak of the ZnO and ZnO:Al films exhibits a small shift to higher angles with increasing substrate temperature and oxygen pressure. The figures also show the calculated full width at the half maximum (FWHM) of each (002) peak, which decreases when the crystallite size increases.

The (002) diffraction peak of the ZnO films is located in 34.36° diffraction angle for the films deposited at the highest substrate temperature (500°C) and for the films deposited at the highest oxygen ambient pressure ($2.5x10^{-2}$ mbar), showing approach to the ideal value, which is 34.42° (according to the value reported in the JCPDS #48-1514 database). The rest of the films exhibit the (002) diffraction angle between 33.7 and 33.9°. For the ZnO:Al thin films, the (002) peak slightly shifts from ~34° to 34.36° with increasing Ts. Increasing Po_2 the peak of the film deposited at $2.5x10^{-4}$mbar show a better approach to the ideal value. Because of the small percentage of the dopant Al ions, no diffraction peaks arising from Al and Al_2O_3 are observed. The deviations from the ideal value of (002) peak are due to non-stoichiometry of the films, probably due to oxygen deficiency. Increasing the Ts, the positions of (002) peaks are shifted to

higher angles. This means that the lattice parameters decrease with increasing Ts[1]. Increasing Po_2, the (002) peak shifts to higher angles and this may be due to the reduction of oxygen vacancies and so an approach to more stoichiometric ZnO film. Also the (004) diffraction peak is observed, with much lower intensity, at approximately 72° diffraction angle.

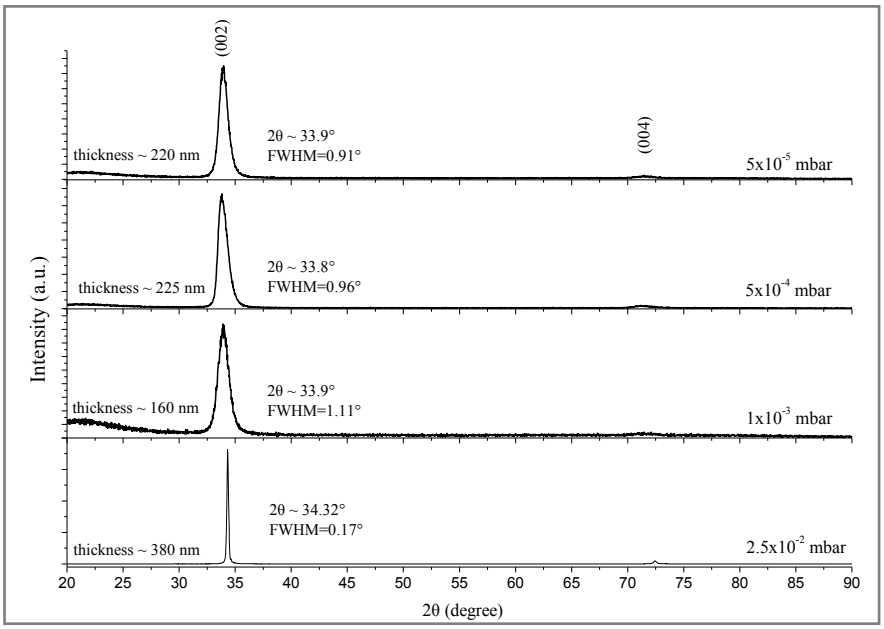

Fig. 5.1: The effect of Po_2 on the crystallinity of the ZnO films at a substrate temperature of 300°C.

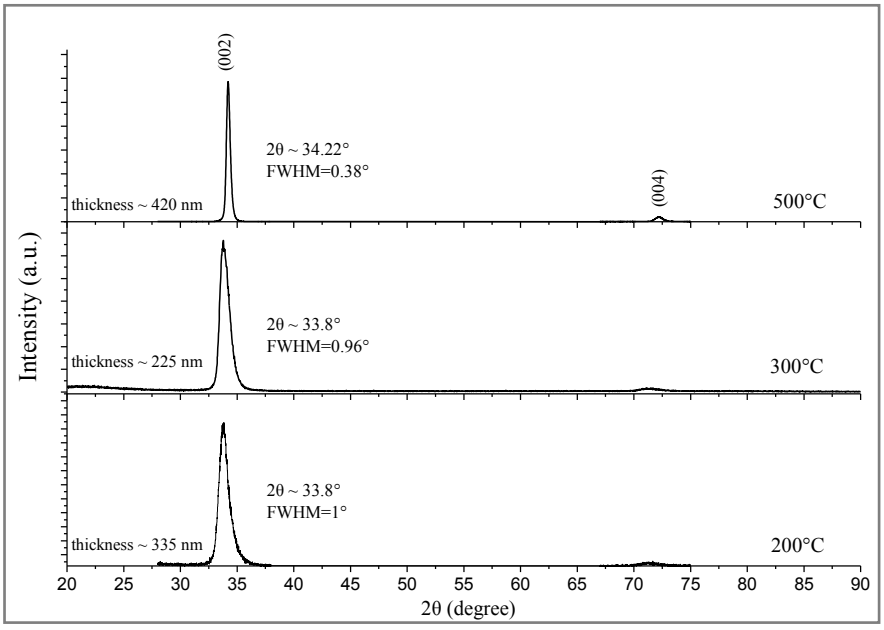

Fig. 5.2: The effect of Ts on the crystallinity of the ZnO films at an ambient oxygen pressure of $5x10^{-4}$ mbar.

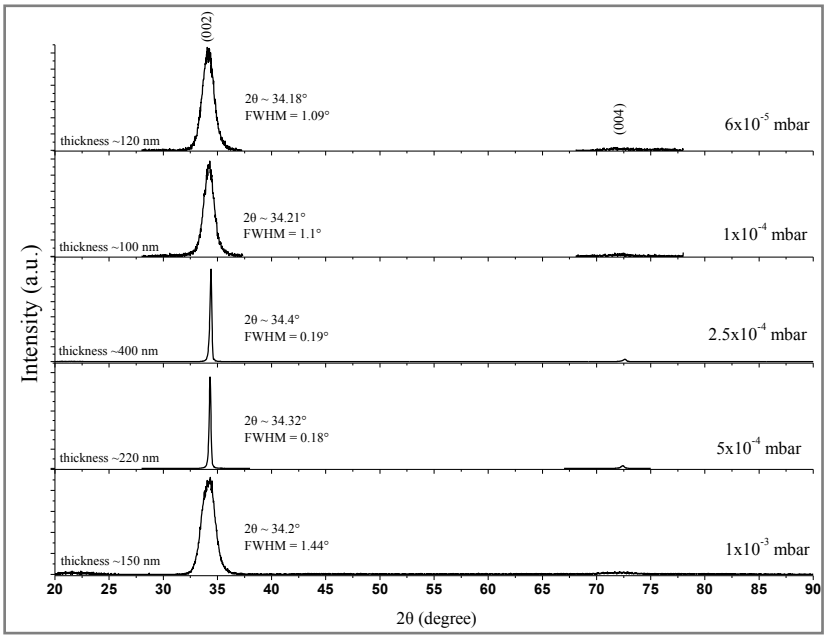

Fig. 5.3: The effect of Po_2 on the crystallinity of the ZnO:Al films at a substrate temperature of 300°C.

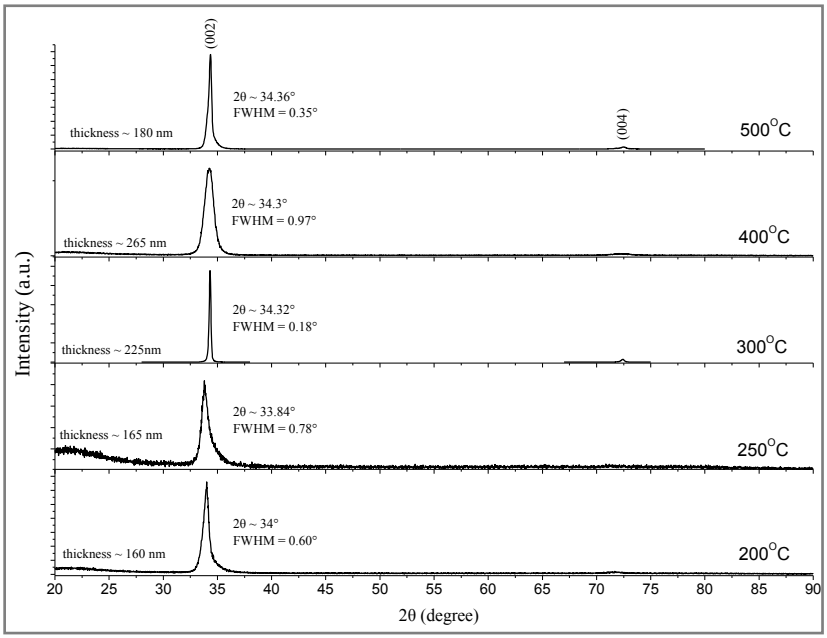

Fig. 5.4: The effect of Ts on the crystallinity of the ZnO:Al films at an ambient oxygen pressure of $5x10^{-4}$ mbar.

As mentioned in paragraph 4.2.3, the grain size of the films can be measured using Scherrer's formula. The derived grain size of the ZnO and ZnO:Al films, as a function of the Ts and the Po_2, is presented in the figures 5.5 and 5.6 below. For the ZnO films, the grain size increases with Po_2 and Ts, being in the range of 8-50 nm, showing the improvement of the crystallinity. Those results are in good agreement with other reported[2].

Fig. 5.3 and 5.6(a) indicate that increasing Po_2 from $6x10^{-5}$ until $5x10^{-4}$ mbar, at 300°C Ts, the crystal quality of the ZnO:Al films improves and then degrades at $1x10^{-3}$ mbar. The largest grain size obtained was 43 nm at $5x10^{-4}$ mbar. The mean grain size, for the rest of the examined pressure range, is of the order of 7.5 nm. For low Po_2 the low crystal quality may be due to high Zn percentage which incorporates to interstitial sites. For high Po_2, excess O may induce defects in the films, causing changes in growth mode on the growth surface and influencing the nucleation, probably resulting in lower crystal quality. Figs 5.4 and 5.6(b) indicate that increasing Ts from 200 to 300°C, at $5x10^{-4}$ mbar Po_2, the crystal quality of the ZnO:Al films improves, and then degrades until 500°C. The best grain size obtained, at $5x10^{-4}$ mbar, was of 45 nm at 300°C. Similar behavior has been reported in the literature[3].

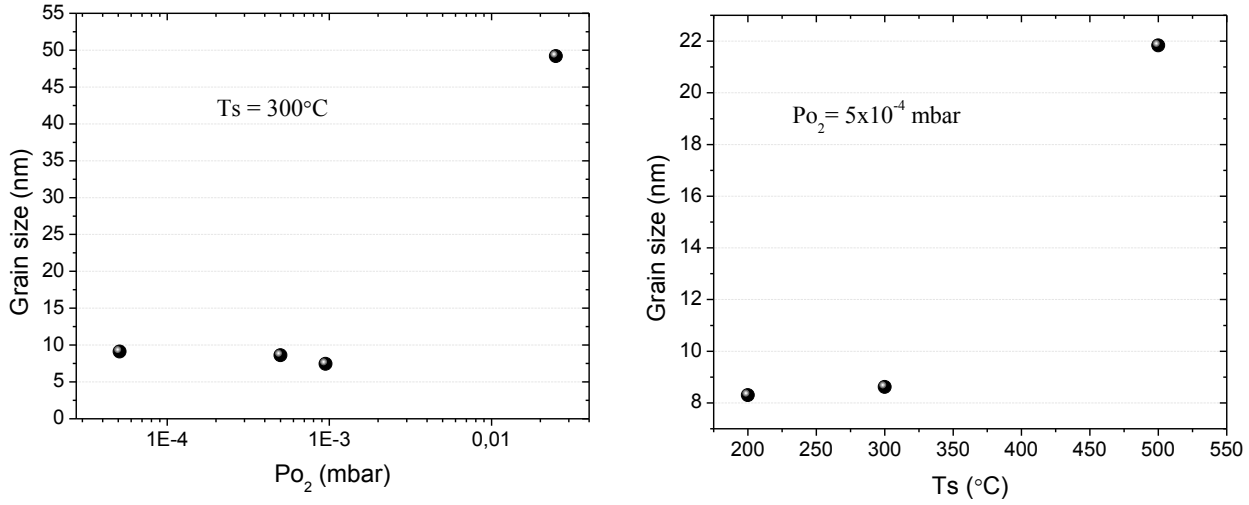

(a) *(b)*

Fig. 5.5: The effect of (a) Po_2 and (b) Ts on the grain size of the ZnO films.

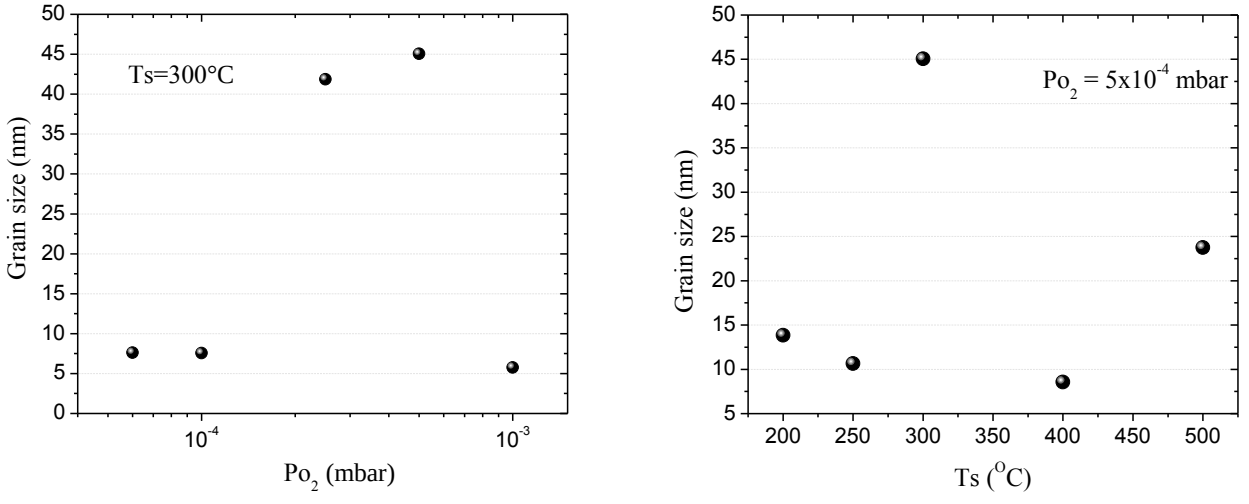

(a) *(b)*

Fig. 5.6: The effect of (a) Po_2 and (b) Ts on the grain size of the ZnO:Al films.

5.3 ELECTRICAL PROPERTIES

The resistivity (ρ), electrons' mobility (μ) and concentration (N_D) of the films were studied by standard resistivity and Hall effect set – ups in the Van der Pauw configuration at room temperature.

The dependence of the electrical properties of the ZnO films on the Ts is presented in figs. 5.7 (a). Increasing Ts no significant changes on the electrical properties of the films were observed. The electron concentration of the ZnO films is of the order of 4.5-5x10^{19} cm^{-3} (fig. 5.7 (a)-(ii)) and the electron mobility is of the order of 6-9 cm^2/Vs (fig. 5.7 (a)-(i)). Increasing Ts, the resistivity slightly increases from 1.5x10^{-2} to 4.2x10^{-2} Ωcm (fig. 5.7 (a)-(iii)).

The dependence of the electrical properties of the ZnO films on the Po_2 is presented in figs. 5.7(b). Increasing the oxygen pressure, the electron concentration increases one order of magnitude, from 2.7x10^{18} to 7.5x10^{19} cm^{-3} (fig. 5.7 (b)-(ii)). The mobility initially decreases from 55 to 6 cm^2/Vs, probably due to the increase of the electron concentration which leads to more electron-electron scattering contributing to lower mobility. For higher Po_2, the mobility increases back to 30 cm^2/Vs (fig. 5.7 (b)-(i)). Increasing the Po_2, the resistivity decreases and reaches the value of 1.7x10^{-2} Ωcm (fig. 5.7 (b)-(iii)).

Doping ZnO with Al increased the electron concentration by almost two orders of magnitude. Al^{+3} substitutes Zn^{+2} and therefore acts as a donor. Increasing the substrate temperature from 200 to 500°C, the electron density slightly decreases from 1.5x10^{21} cm^{-3} to 6.7x10^{20} cm^{-3} (fig. 5.8 (a)-(ii)). The lowest electron density observed at 500°C may be due to the evaporation of some Zn atoms, as the melting point of Zn is at 419.6°C. The electron mobility increases from 11 to 22.7 cm^2/Vs (fig. 5.8 (a)-(i)) having a maximum at 300°C (31 cm^2/Vs). The increased mobility can be explained by the high crystal quality and consequently the large grain size of the films at this Ts. Generally, during transport in thin films, the electrons are scattered by the boundaries between the grains. The mean free path of the electrons is approximately equal to the mean grain diameter. Thus large grain size favors fewer scatterings which contributes to higher electron mobility and consequently less resistivity. Due to the above claim, the reason of the lowest resistivity of 2.3x10^{-4} Ωcm obtained at 300°C becomes comprehensible (fig. 5.8 (a)-(iii)).

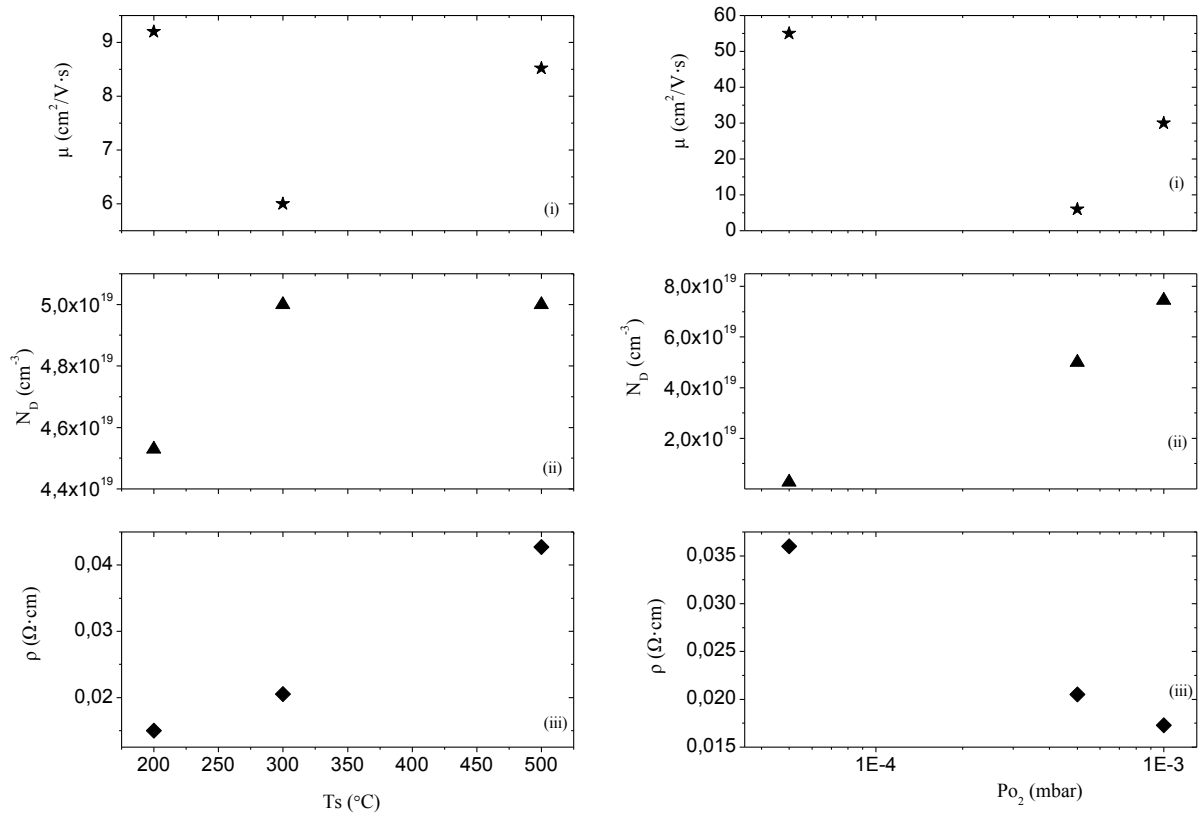

Fig. 5.7: The effect of (a) Ts and (b) Po_2 on the (i) mobility (μ), (ii) the electrons' concentration and (iii) the resistivity of the ZnO films.

Varying oxygen pressure from $5x10^{-5}$ to $1x10^{-3}$ mbar at 300°C of Ts, the electron concentration does not significantly change, having values of the order of $0.9x10^{21}$ – $1.7x10^{21}$ cm^{-3} (fig. 5.8 (b)-(ii)). The electron mobility has its maximum value of 31 cm^2/Vs at $5x10^{-4}$ mbar of Po_2, probably due the large grain size of the films at this Po_2. The mean electron μ, for the rest of the examined pressure range, is of the order of 10 cm^2/Vs (fig. 5.8 (b)-(i)). Increasing Po_2 the resistivity slightly decreases having its minimum value of $2.3x10^{-4}$ Ωcm at $5x10^{-4}$ mbar (fig. 5.8 (b)-(iii)). It appears that at approximately $5x10^{-4}$ mbar, the combination of good crystal quality and the sufficient existence of oxygen vacancies in the films, give rise to conductivity.

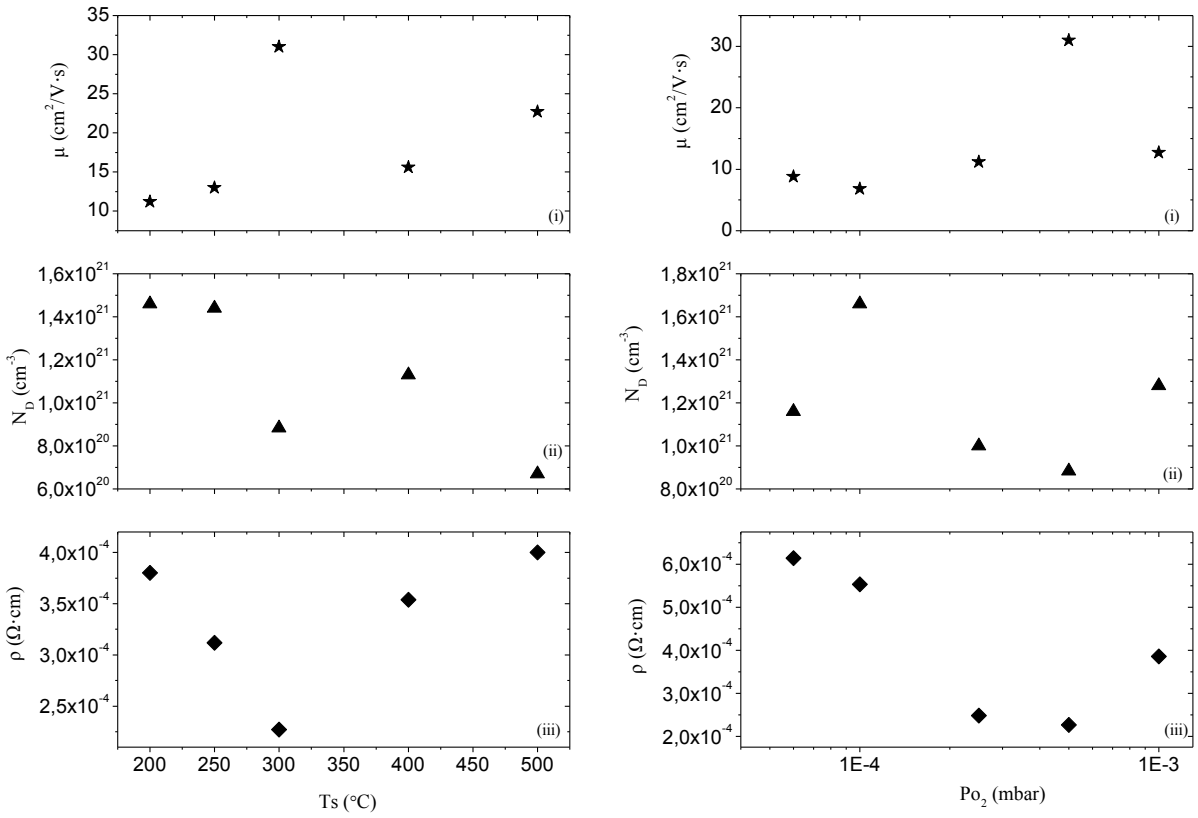

(a) (b)

Fig. 5.8: The effect of (a) Ts and (b) Po_2 on the (i) mobility (μ), (ii) the electrons' concentration and (iii) the resistivity of the ZnO:Al films.

5.4 Optical Properties

The optical properties of the films were studied by UV-NIR Transmittance & Reflectance. Figures 5.9 and 5.10 show the effect of the substrate temperature and ambient oxygen pressure on the transmittance of the ZnO and ZnO:Al films, respectively.

A noticeable increase of the transmittance, in the visible range of the spectrum, is obtained by increasing the substrate temperature and the background oxygen pressure for ZnO films, as can be observed in figs. 5.9(a) and 5.9(b), respectively. This increment might be a result of the crystal improvement. The ZnO:Al films have a similar behave, but have a slight decrease at $1x10^{-3}$ mbar of Po_2. At low oxygen pressure, the lower transmittance may be due to excessive Zn ions which exist at interstitial sites and probably absorb light. Films grown at 400°C show high transmittance, however they exhibit low crystal quality. This is may be due to the large optical band gap of these films, which results in limited absorption of photons and thereby increase of the transmittance.

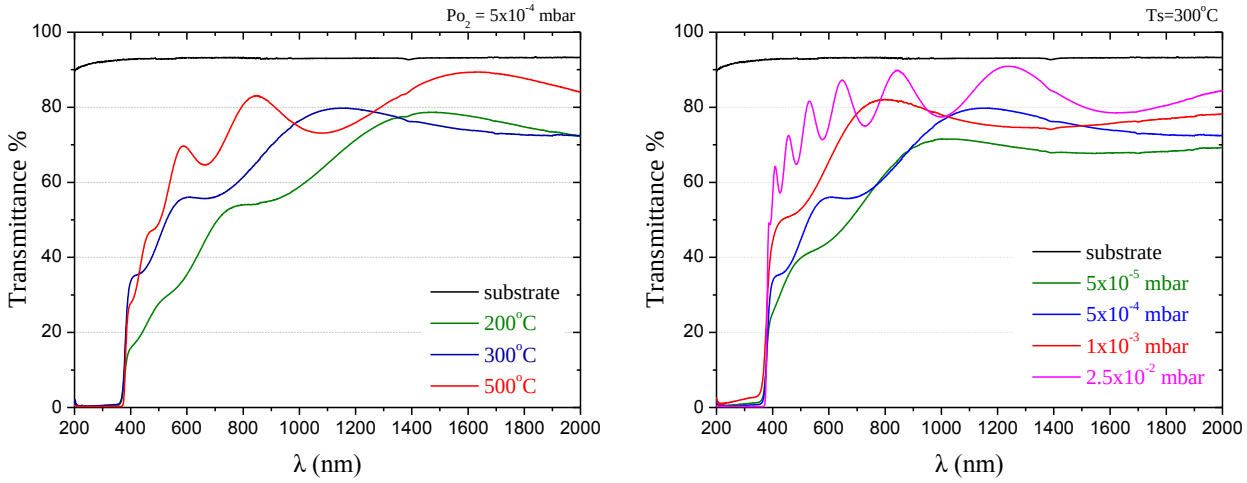

(a) (b)

Fig. 5.9: The effect of (a) Ts and (b) Po_2 on the Transmittance of the ZnO films.

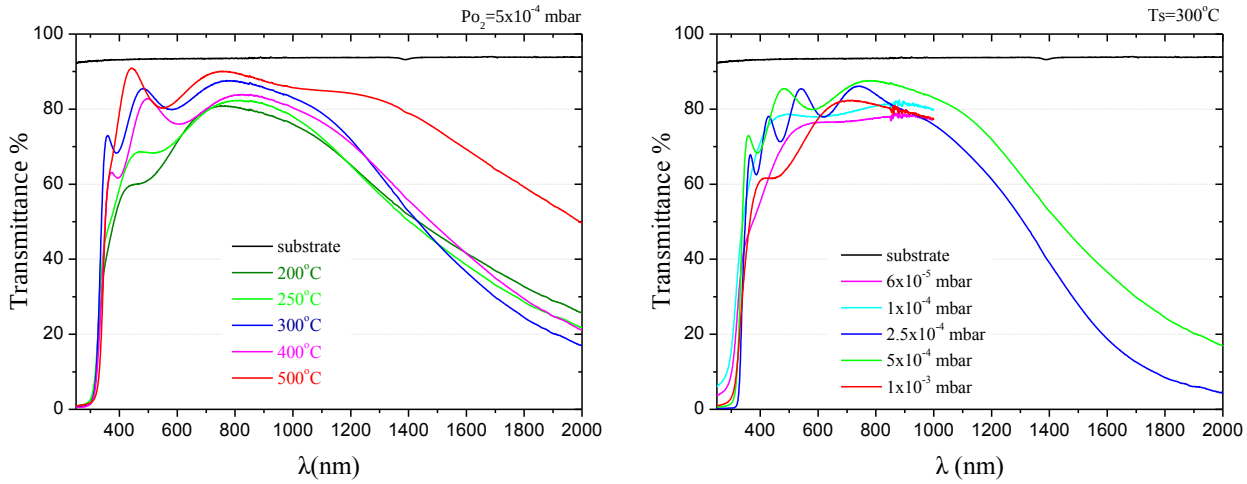

(a) (b)

Fig. 5.10: The effect of (a) Ts and (b) Po_2 on the Transmittance of the ZnO:Al films.

Fig. 5.11 presents transmittance and reflectance spectra of ZnO and ZnO:Al films grown at 300°C and $5x10^{-4}$ mbar. In the near-infrared region, transmittance decreases while reflectance starts increasing for the ZnO:Al films, they behave like metals, while for the un-doped ZnO films the change is slight. This behavior of the doped films is due to their high free electron concentration and is also report by Nimani et al.[4], Singh et al.[5] and Kim et al.[6] Consequently, this is an indication of increased conductivity.

As mentioned in paragraph 4.2.2, the optical energy band gap, E_g, of the film is determined from the absorption coefficient data (eq. 4.2), which in turn is derived by the combination of the thickness of the film, the transmittance and reflectance data (eq. 4.1). A

typical plot is shown in fig. 5.12. Compared to the band gap E_g of ZnO single crystal (3.37 eV), the calculated optical E_g of the ZnO films is somewhat smaller, ranging from 3.26 to 3.30 eV, while ZnO:Al films showed higher optical E_g ranging from 3.67 to 3.90 eV. This difference in the E_g between the doped and un-doped ZnO films is obvious in fig. 5.12 and also in fig. 5.11 where in the transmittance curves, the threshold of optical absorption shifts to shorter wavelengths with the doping of ZnO (the blue arrow in fig. 5.11 indicates the shift).

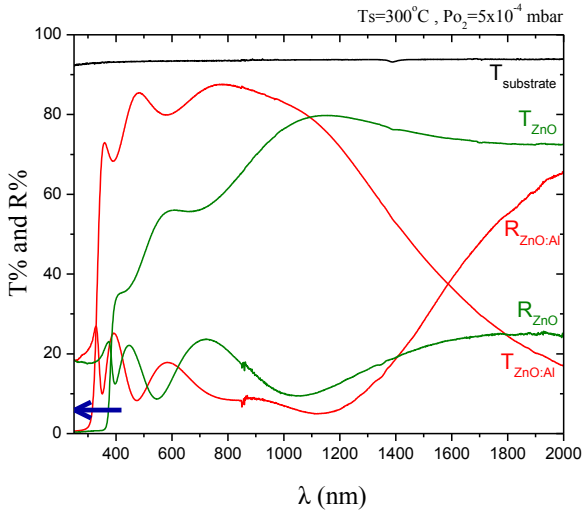

Fig. 5.11: Transmittance and Reflectance spectra of ZnO and ZnO:Al films grown at 300°C and 5x10^{-4} mbar (the arrow indicates the shift).

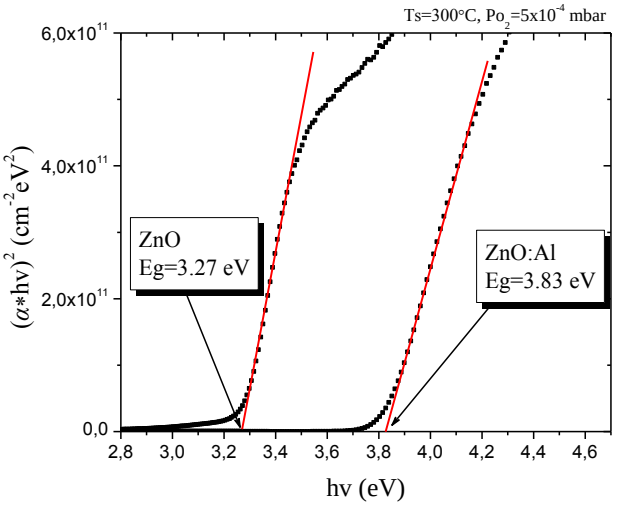

Fig. 5.12: Optical energy band gap determined by extrapolation of $(\alpha h\nu)^2$ as a function of photon energy (hv) of an Al-doped and an un-doped ZnO film grown at 300°C of Ts and 5x10^{-4} mbar of Po_2.

It has been reported[3] that the increase in the optical band gap with an increase of the electron concentration is related to shift of the Fermi level in conduction band, in degenerate semiconductors. This phenomenon is known as the ‘‘blueshift,’’ and the relationship of the optical band gap difference between the doped and un-doped semiconductor was proposed by Moss & Burstein (M-B)[7] and is equal to

$$\Delta E_g = \frac{\hbar^2}{2m^*_{VC}}(3\pi^2 N_D)^{2/3}$$

where m^*_{VC} is the reduced effective mass $(1/m^*_{VC} = 1/m^*_C + 1/m^*_V)$ and N_D is the carrier concentration. ZnO is naturally an n-type material and when it is doped with Al, the electron concentration is related to the shift of the Fermi level, which will be inside the conduction band. Since the states below the Fermi level in the conduction band are filled, the absorption edge

should shift to higher energy, above the Fermi level. Thus, the observed shift can be related to the Moss-Burstein effect. An attempt was made to evaluate the ΔE_g according to the M-B equation. Optical modeling of transmittance and reflectance spectra was performed[i] in order to extract the effective mass (m^*_{VC}/m_O) at two ZnO:Al samples, the results are listed in table 5.2. The second column, in the table, is the carrier concentration found by electrical characterization. The third column shows the experimental optical band gap difference ΔE_g^{exp} between the Al-doped and un-doped ZnO calculated according to Tauc's plot. And the last column presents the optical band gap difference ΔE_g^{B-M} calculated according to M-B equation. As can be seen the ΔE_g^{exp} is rather smaller than the ΔE_g^{B-M}.

Table 5.2

	m^*_{VC}/m_O	N_D (cm^{-3})	ΔE_g^{exp} (eV) experimental	ΔE_g^{B-M} (eV) theoretical (B-M)
Sample 1[ii]	0.62	1.46×10^{21}	0.54	0.75
Sample 2[iii]	0.42	0.67×10^{21}	0.4	0.66

It has been reported[8] that when the electron concentration is above the Mott critical value[9], then the optical band gap keeps on increasing but at a different rate, i.e. a simultaneous narrowing of the band gap is taking place. The decrease is related to the appearance of the band gap renormalization effect. As the electron concentration is above the Mott critical value, the modification of electronic states begins to appear in the crystal because of the correlated motion of the charge carriers and their scattering against ionized impurities. Thus, the band gap renormalization due to many-body effects leads to a narrowing of the band gap. There is general agreement that the B-M effect and the many-body effects are dominant in affecting the optical gap in intentionally doped semiconductors. Furthermore, there might be other band gap effects, of secondary importance, such as polaron, strain, and other types of imperfection[10]. So the divergence from the estimated ΔE_g^{B-M} could be related to the many-body effects and the other effects mentioned above. Another possible reason of the divergence could be the fact that the above equation was derived after some simplifications that were considered. And those simplifications induce errors at the results.

[i] The optical modeling performed by Dr. A. Kondilis.

[ii] Deposition parameters: Ts=200°C and $Po_2=5 \times 10^{-4}$ mbar

[iii] Deposition parameters: Ts=500°C and $Po_2=5 \times 10^{-4}$ mbar

5.5 CONCLUSIONS

The effect of the ambient oxygen pressure and the substrate temperature, at the examined range of values, on the properties of the grown films is different for ZnO and ZnO:Al thin films.

ZnO films showed high crystal quality at high oxygen ambient pressure and at high substrate temperature. The electron concentration achieved was as high as 7.5×10^{19} cm^{-3} and the lowest resistivity obtained was 1.5×10^{-2} Ωcm. The calculated optical energy band gap was approximately 3.30 eV and the transmittance obtained at 300°C and at 2.5×10^{-2} mbar was not more than 70% in the visible range of the spectrum.

Doping ZnO with Al, using 2%Al:ZnO PLD target, resulted in the increase of the electron concentration by an order of two reaching 1.7×10^{21} cm^{-3}, while the resistivity decreased by an order of two reaching 2.3×10^{-4} Ωcm. According to literature, the 2%Al:ZnO PLD targets were reported to fabricate Al:ZnO thin films with the lowest resistivity[11]. The calculated energy band gap was as high as 3.90 eV. The highest transmittances obtained were approximately 80% in the visible range of the spectrum (above 300°C and between 1×10^{-4} and 5×10^{-4} mbar).

The above results are comparable to others reports[2,3,12].The resistivity obtained for the ZnO:Al thin films may be low but is still inferior to that of ITO (resistivity $>10^{-4}$ Ωcm).

5.6 REFERENCES

[1] F.K. Shan, et al., J. Appl. Phys. 101 (2007) 053106

[2] A. Klini, et al., J. Appl. Phys., 98, 123301 (2005)

[3] S. M. Park, et al., Appl. Surf. Sci., 253 (2006) 1522–1527

[4] T. Minami,et al., Jpn. J. Appl. Phys., Part 2 **24**, L605 (1985)

[5] A. V. Singh, et al., J. Appl. Phys., Vol. 90, No. 11 (2001)

[6] H. Kim, et al., Thin Solid Films, 377-378 (2000) 798-802

[7] E. Burstein, Phys.Rev., 93 (1954) 632

T.S. Moss, Proc.Phys. Soc.Lond. B, 67 (1954) 775

[8] J. G. Lu, et al., J. Appl. Phys., 101, 083705 (2007)

Fu-Chun Zhang, et al., Chin. Phys. Lett., 25, No. 10 (2008) 3735

T. Makino, et al., Phys. Rev. B, 65 121201 (R)

[9] N. F. Mott, Philos. Mag. 6, 287 (1961)

[10] B. E. Sernelius, et al., Phys. Rev. B 37, 10244 (1988)

R. B. Fair, J. Appl. Phys. 50, 860 (1979)

[11] Y. Liu, et al., Appl. Surf. Sci. 253 (2007) 3727

D. Horwat, et al., Thin Solid Films 515 (2007) 5444

A. V. Singh,et al., J. Appl. Phys., 95, No. 7, 1 (2004)

R. K. Shukla, et al., Journal of Crystal Growth, 294, 427-431 (2006)

[12] A. V. Singh, et al., J. Indian Inst. Sci.,81,527-533 (2001)

M. Hiramatsu, et al., J. Vac. Sci. Technol. A, 16(2) (1998)

H. Kim, et al., Appl. Phys. Lett., 76, 3 (2000)

CHAPTER 6
PULSED LASER DEPOSITION OF UN-DOPED AND DOPED $SrCu_2O_2$ THIN FILMS

6.1 INTRODUCTION

This chapter presents results on the un-doped and the doped $SrCu_2O_2$ thin films, grown by pulsed laser deposition. In this study, two UV-pulsed lasers of different emitted wavelength were used for the growth of the films. The structural and optical properties were studied by X-ray diffraction and UV-NIR reflectance and transmittance, respectively, for different deposition parameters.

6.2 EXPERIMENTAL CONDITIONS

The lasers used for the fabrication of the films were a KrF excimer with 248 nm wavelength and a XeCl excimer with 308 nm wavelength. The base pressure prior to deposition was better than 10^{-6} mbar. The duration of each deposition was ~15 min. All depositions were realized in an oxygen ambient atmosphere of $5x10^{-4}$ mbar pressure on different substrates. The experimental conditions are shown in Table 6.1.

Three different targets were used, with composition $SrCu_2O_2$, $(X_{0.03}Sr_{0.97})Cu_2O_2$ and $(X_{0.06}Sr_{0.94})Cu_2O_2$ [i] (target #; TA050 (SCO), TA047 (SCO:X(3%)), TA054 (SCO:X(6%))). Fig. 6.1 (b), (c) and (d) present the XRD spectra derived from the characterization of each target, respectively. Fig. 6.1 (a) shows position of the diffraction angles of $SrCu_2O_2$ crystalline phase according to JCPDS #48-1514 database.

[i] Due to confidentiality reasons, the X component is not disclosed.

Table 6.1: Experimental conditions for the growth of SCO and SCO:X thin films by PLD.

Substrate type	UV-graded fused silica (15x15x1 mm) n-Si (P-doped, R=1-10Ωcm, n~10^{14} cm^{-3})
Substrate – target distance	4 cm
Laser parameters	λ=248 nm, τ =34 ns spot size ≈ 4mm^2 , F=0.5 J/cm^2 10000 pulses/deposition, r.r.=10 Hz
	λ=308 nm, τ =34 ns spot size ≈ 4mm^2 , F=0.5, 2 J/cm^2 10000 pulses/deposition, r.r.=10 Hz
Substrate temperature (T_S) at an ambient oxygen pressure of 5x10^{-4} mbar	300, 400, 500, 600 °C

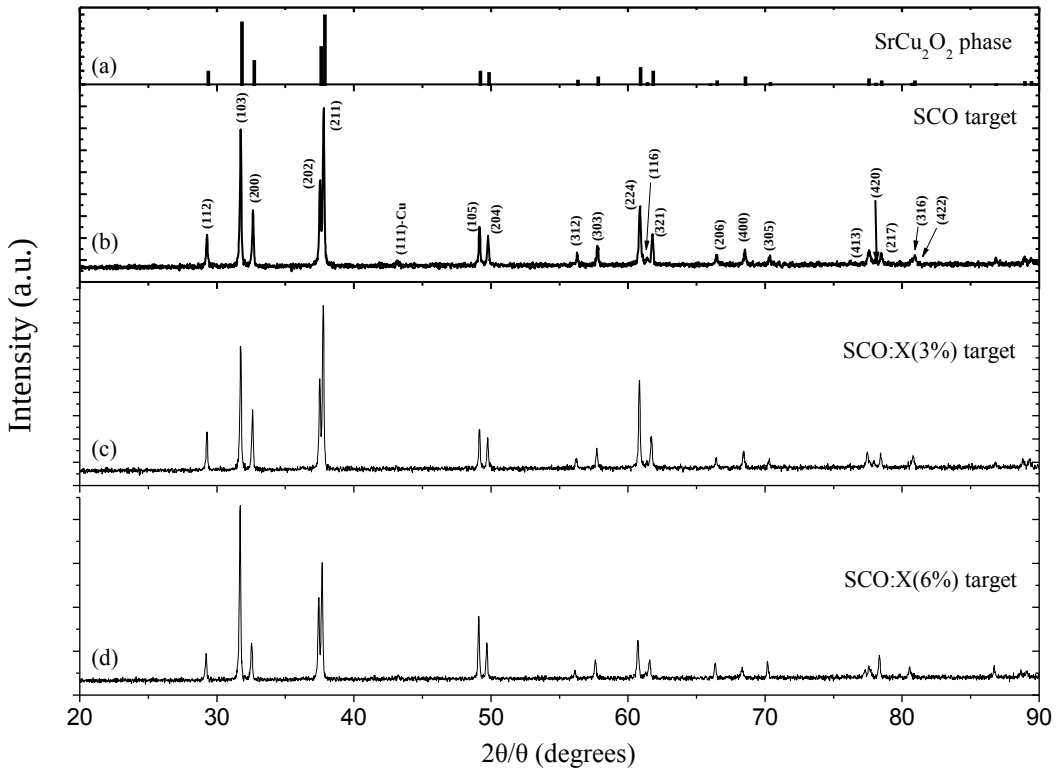

Fig. 6.1: (a) Diffraction angles of $SrCu_2O_2$ phase according to JCPDS #48-1514 database. XRD spectra of the (b) SCO, (c) SCO:X(3%) and (d) SCO:X(6%) targets.

Comparing the theoretical database with the diffraction angles of the targets, it is obvious that the targets are polycrystalline $SrCu_2O_2$. Furthermore, a small amount of pure Cu is present in the un-doped SCO target. A small shift, from 0.07 to 0.19°, to lower angles is observed by increasing the percentage of the dopant, as a result of the increase of the lattice parameters.

It is worth mentioning here some information about the phase stability of the Sr-Cu-O bulk system obtained by Suzuki et al. [Chapter 1, Ref. 25] at $5x10^{-4}$ mbar of Po_2. According to their work, in bulk the phase stability line for $SrCu_2O_2$ lies approximately between 580 and 950°C. At 300°C and 400°C the bulk phase diagram predicts the phase assemblage of $Sr_{14}Cu_{24}O_{41}$+CuO and $SrCuO_2$+CuO, respectively, where ~330°C is the dividing temperature between the two phase assemblages.

6.3 SCO AND SCO:X THIN FILMS DEPOSITED BY A 248nm LASER

6.3.1 SCO THIN FILMS

SCO thin films were grown on fused silica substrates at 300°C of Ts and $5x10^{-4}$ mbar of Po_2, and had thickness approximately 150-250 nm. Fig .6.2 shows an optical microscope image of a SCO thin film. The films appear to have a few droplet-shaped particulates on their surfaces. The possible origin of the particulates is mentioned in chapter 2.6.1; any of the reasons mentioned can be existent. According to XRD measurements, all films showed an amorphous crystalline phase.

To improve crystallinity, SCO thin films were grown on n-Si substrates, as silicon has crystal structure (diamond crystal structure). The growth took place under an ambient oxygen pressure of $5x10^{-4}$ mbar at different substrate temperatures. The thickness of the films was between 100 and 350 nm. Fig. 6.3 shows the XRD spectra[ii] derived from the characterization of the SCO/Si thin films as a function of the substrate temperature (300, 400, 500 and 600°C). All the films contain the $SrCu_2O_2$ crystalline phase. Films deposited at 500°C of Ts, have a small amount of $SrCu_2O_3$ phase as well, and when deposited at 600°C the $SrCu_2O_3$ phase decomposes and a small amount of Cu_2O phase is present. It seems that the above XRD results are not consistent with the phase behavior of the bulk. However phase pure SCO thin films were grown on Si substrates at temperature as low as 300°C. The dominant crystal orientations are shown on the spectra. Increasing Ts the preferred crystal orientation (202) gradually changes to (211).

The size of the crystallites was measured using the Scherrer formula (eq. 4.4) and showed a tendency of crystal improvement with the increase of the Ts. The crystallite size increases from 15.5 nm to 21.5 nm, with a minimum of 10 nm observed at 400°C (fig. 6.9).

[ii] The structural characterization of the SCO/Si films carried out by Olivier Durand, in Thales laboratory of France, by X-ray diffraction measurements. The X-ray diffraction performed using an INEL CPS-120 curved detector, with the $Cu_{K\alpha 1}$ wavelength $\lambda = 0.1540562$ *nm*. The incident beam angle was kept to 8 degrees with respect to the sample surface.

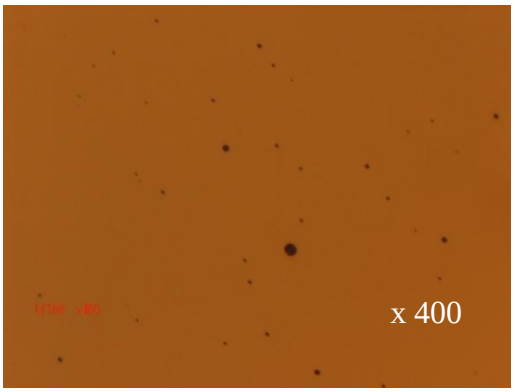

Fig. 6.2: Typical microscope image of a SCO thin film grown on a fused silica substrate (~280 nm thickness) by a 248nm laser wavelength with 0.5 J/cm^2 laser pulses under 5x10^{-4} mbar of Po_2 at 300°C of Ts.

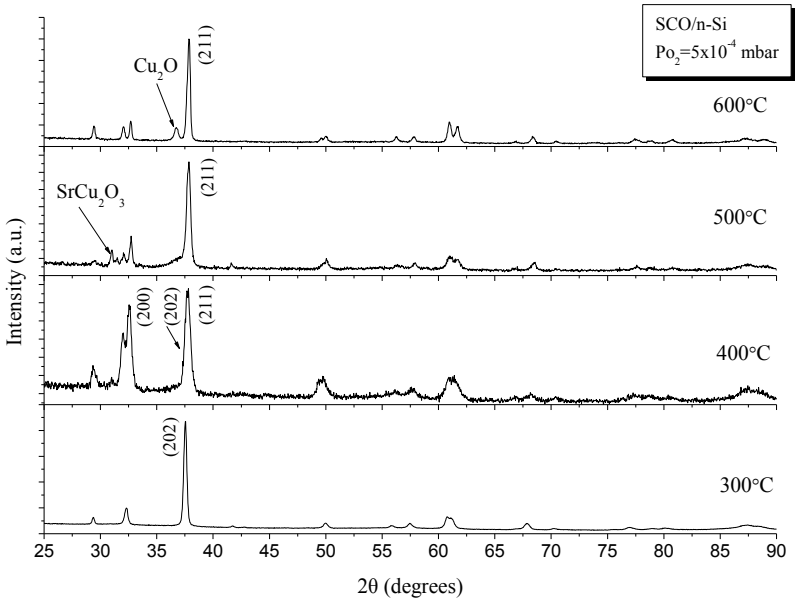

Fig. 6.3: The effect of Ts on the crystal structure of the SCO thin films deposited on Si substrates, at an ambient oxygen pressure of 5x10^{-4} mbar.

Fig. 6.4 presents the transmittance and reflectance spectra of a SCO thin film, deposited on fused silica. The film has ~30-50% in the visible region probably due to poor crystal quality which gives rise to absorption. In the near-infrared region, the film is relatively transparent indicating that the concentration of free carriers is not high enough.

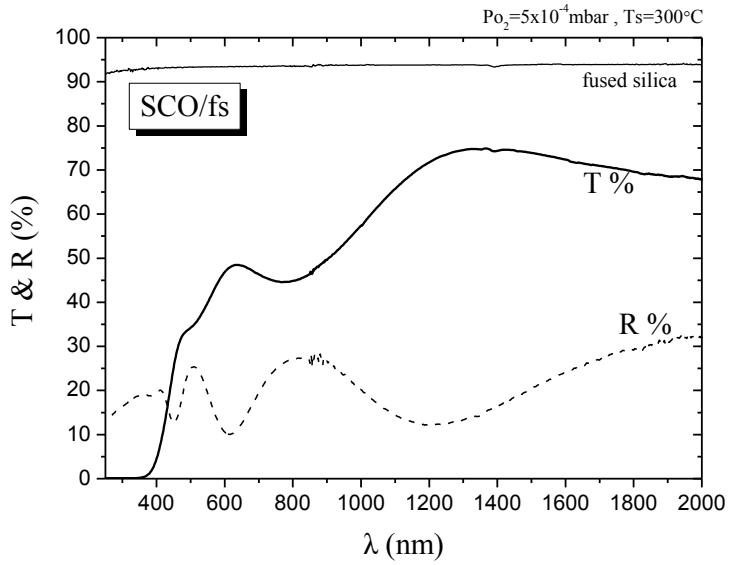

Fig. 6.4: Transmittance and reflectance spectra of a SCO thin film grown on a fused silica substrate at $5x10^{-4}$ mbar of Po_2 and 300°C of Ts by a 248 nm laser.

The optical energy band gap E_g of the SCO films, was evaluated according to Tauc's plot for a direct transition (chapter 4.2.2) and was approximately 3.10-3.24 eV. A typical plot is shown in fig. 6.7. Compared with the energy band gap of the SCO crystal (3.3 eV), the calculated optical E_g is somewhat slightly smaller.

In order to improve the properties of the SCO/fs films, they underwent rapid thermal annealing (RTA), at 330°C under forming gas flow (95% N_2 and 5% H_2) for 10 min. After RTA the amorphous as-deposited films obtained a better crystallized structure, although they still had a great amount of amorphous phase (fig. 6.5). The films contain the $SrCu_2O_2$ crystalline phase. There is an overlap between (202) and (211) crystal orientations, which are the two dominant orientations, but (211) seem to be more intense. Also, (002) is distinct. The improvement of the crystal structure is attributed to the annealed temperature.

After RTA the films exhibited a significant increase in transmittance in the visible range of the spectrum (fig. 6.6), as a result of the improvement of the crystal structure which resulted in less absorption of the photons. The optical E_g slightly increased to 3.26-2.29 eV, approaching the E_g of the SCO crystal (3.3 eV). Fig. 6.7 shows the relative Tauc plots, before and after RTA, where the slight increase is obvious.

Electrical measurements of the annealed films confirmed the p-type conductivity and showed that the resistivity was of the order of $\sim 10^3$ Ωcm and the carrier concentration was $\sim 10^{12}$ cm^{-3}.

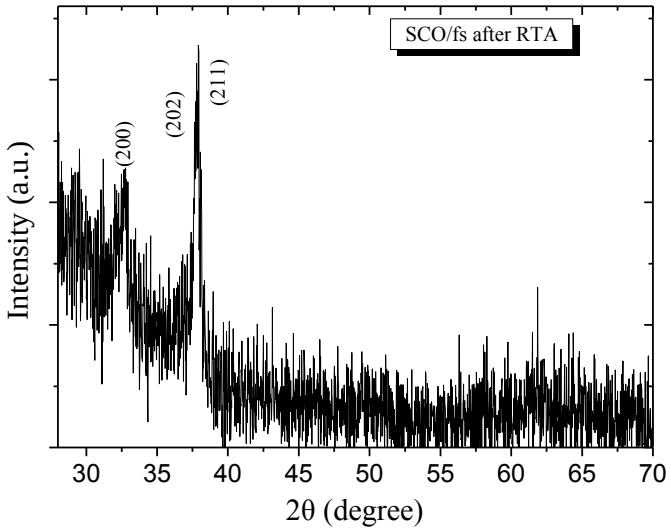

Fig. 6.5: XRD spectrum of a SCO thin film, after RTA, grown on fused silica substrate by a 248 nm laser, at $5x10^{-4}$ mbar of Po_2 and 300°C of Ts.

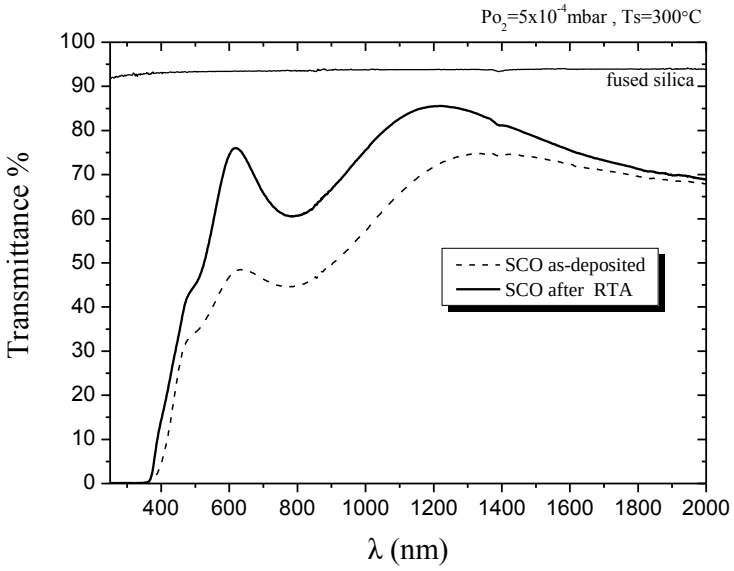

Fig. 6.6: Before and after RTA transmittance spectra of a SCO thin film grown on fused silica substrate by a 248 nm laser, at $5x10^{-4}$ mbar of Po_2 and 300°C of Ts.

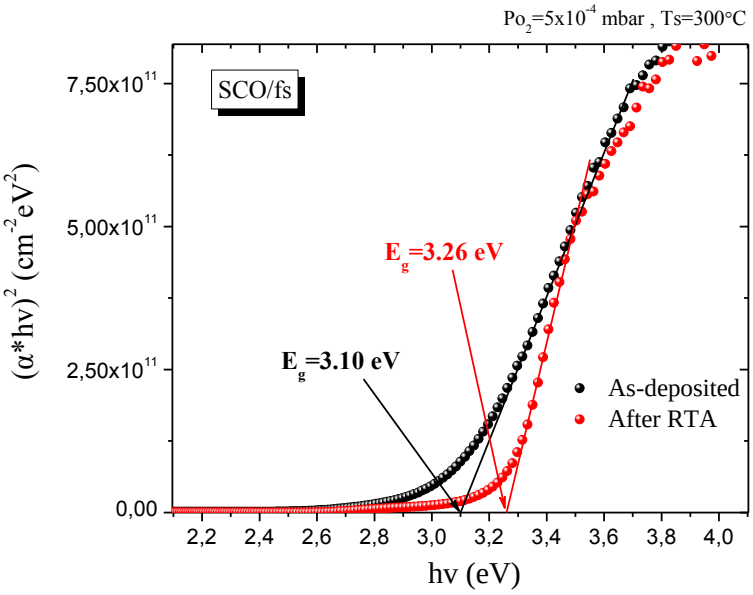

Fig. 6.7: Optical energy band gap, determined by extrapolation of $(\alpha h\nu)^2$ as a function of the photon energy ($h\nu$) of a SCO film, as-deposited and after RTA, grown by a 248 nm laser at 300°C of Ts and $5x10^4$ mbar of Po_2.

6.3.2 DOPED SCO THIN FILMS

In order to improve transparency in the visible region and increase the carrier concentration, an effort was made to fabricate doped SCO thin films on fused silica and n-Si. The targets used were the SCO:X(3%) and SCO:X(6%).

SCO thin films were grown on fused silica substrates at 300°C of Ts and $5x10^{-4}$ mbar of Po_2, and had thickness approximately 150-250 nm. The optical microscope revealed surfaces similar to the un-doped films (fig. 6.2). According to XRD measurements, all films showed an amorphous phase, similar to the un-doped films. On the contrary, when the deposition took place on n-Si substrates, all the films contained the SCO crystalline phase, just as obtained for the un-doped films. The thickness of the films in the latter case was ~100-400 nm. Figs 6.8 (a) and (b) show the XRD spectra of the SCO:X(3%) and SCO:X(6%) thin films, respectively, when deposited on n-Si substrates at $5x10^{-4}$ mbar of Po_2 and different substrate temperatures (300, 400 and 500°C). All films deposited at 500°C have a small amount of $SrCu_2O_3$ phase as well. The dominant crystal orientation of the films is mainly the (211), and the (200) follows.

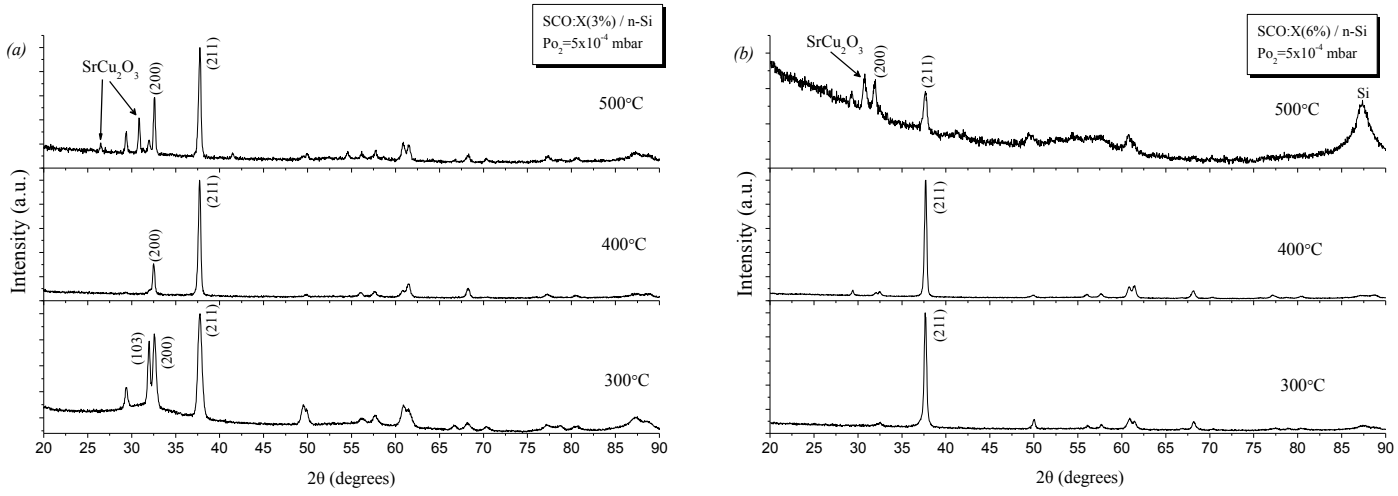

Fig. 6.8: The effect of Ts on the crystal structure of the (a) SCO:X(3%) and (b) SCO:X(6%) thin films deposited on Si substrates, at an ambient oxygen pressure of $5x10^{-4}$ mbar.

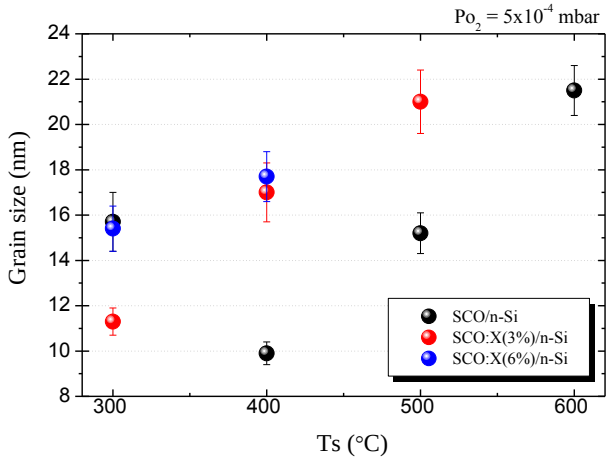

Fig. 6.9: The effect of Ts on the grain size of the SCO, SCO:X(3%) and SCO:X(6%) thin films deposited on Si substrates, at an ambient oxygen pressure of $5x10^{-4}$ mbar.

No clear changes of the diffraction angle have been observed due to doping. The size of the crystallites showed a tendency of crystal improvement, increasing from approximately 11.5 to 21 nm with the increase of the Ts, as shown in fig.6.9.

For a direct comparison fig. 6.10 presents the transmittance spectra of the un-doped and doped SCO thin film, deposited on fused silica. It can be seen that there is an increase of the transmittance at the visible region with increasing doping. In the near-infrared region, the films still indicate high transparency and thus the carrier concentration probably remains almost the same. The optical E_g of the SCO:X(3%) and SCO:X(6%) films is ~3.12 and ~3.29 eV, respectively.

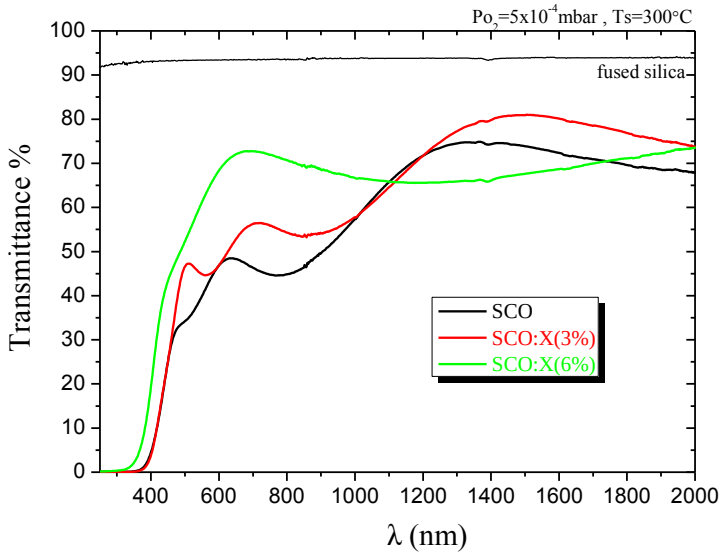

Fig. 6.10: Transmittance of un-doped and X-doped SCO thin films grown by a UV laser of 248 nm wavelength, at $5x10^{-4}$ mbar of Po_2 and 300°C of Ts.

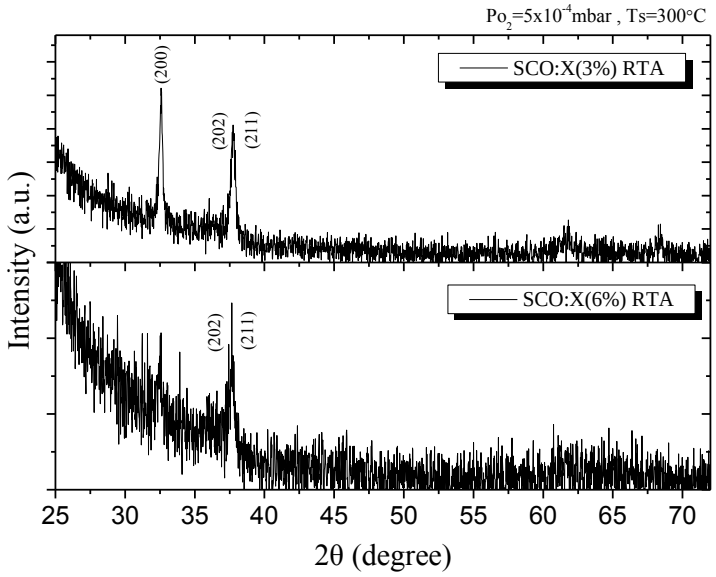

Fig. 6.11: XRD spectra of X-doped SCO thin films after RTA, grown by a 248 nm laser, at 5x10^{-4} mbar of Po_2 and 300°C of Ts.

After RTA, the films attain a certain amount of crystallinity, as also observed for the un-doped films. As shown in fig. 6.11, the XRD spectra reveal a better crystallized structure, containing the $SrCu_2O_2$ crystalline phase and a great amount of amorphous phase. As a result the films exhibited a significant increase in transmittance in the visible region shown in fig. 6.12. Furthermore, the optical E_g estimated 3.29 eV (SCO:X(3%)) and 3.31 eV (SCO:X(6%)). Fig 6.13 shows the optical E_g as a function of the doping. As can be seen there is a small tendency of the increase of the optical E_g with the doping for the as-deposited films. This might be related to a small increase of the Cu vacancies due to the doping, which favors the increase of the E_g. After annealing, a slight increase of the gap is observed but no dependence on the doping is observed.

Electrical measurements of the annealed X-doped films showed ~10-10^2 Ωcm resistivity and ~10^{15} cm^{-3} carrier concentration. There is a significant increase of the carrier concentration compared to the un-doped films by an order of ~3 and the resistivity decreased by an order of ~1.

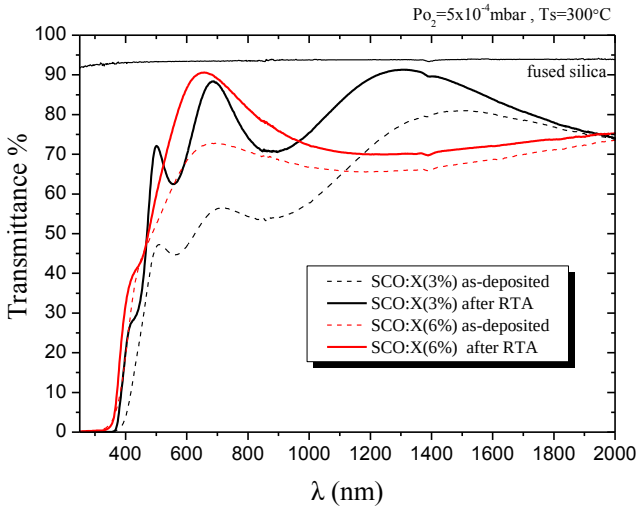

Fig. 6.12: Transmittance spectra of X-doped SCO thin films before and after RTA, grown by a 248 nm laser, at 5x10^{-4} mbar of Po_2 and 300°C of Ts.

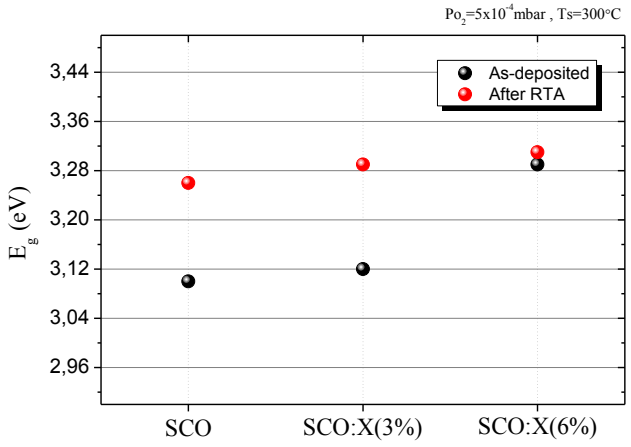

Fig. 6.13: Optical E_g, before and after RTA, as a function of the doping, for films grown by a 248 nm laser.

6.4 SCO AND SCO:X THIN FILMS DEPOSITED BY A 308nm LASER

The growth of un-doped and doped SCO thin films was obtained, on fused silica and n-Si substrates, by a pulsed UV laser of 308 nm wavelength. This brief attempt aimed to observe the effect of the different laser wavelength on the structural and optical properties of the films. When a laser beam with higher wavelength λ interacts with the target material, then the laser energy E which is transferred to the material and excite the electrons is less according to the equation $E=hc/\lambda$. Consequently, the excited electrons will emit phonons with less energy, which is afterwards converted to heat. The less energy converted to heat results in lower developing temperature on the target surface, causing the vaporization of species with less energy. Thus species with lower velocity are travelling towards the substrate. The different energy deposited on the target will alter the growth mode of the film.

For the films grown on fused silica substrates, the density of the laser energy, used for the ablation of the targets, was 0.5 and 2 J/cm^2 and the thickness of the films was below 100 nm and 250-350 nm, respectively. The films were grown under an ambient oxygen pressure of 5x10^{-4} mbar, at 300 and 400°C of substrate temperature. For the films grown on Si substrates, the density of laser energy used was 2 J/cm^2 and the growth took place under an ambient oxygen pressure of 5x10^{-4} mbar and at 300°C of Ts. The thickness of the films was 150-250 nm.

6.4.1 SCO THIN FILMS

Fig. 6.14 presents a typical image of a SCO thin film grown by the UV laser of 308 nm wavelength, which is similar to fig. 6.2 of the film deposited by the UV laser of 248 nm.

Films grown on fused silica with 0.5 J/cm^2 laser pulses had low thickness, below 100 nm. Consequently, the transmittance of light and the optical E_g was slightly higher than those

grown with 2 J/cm^2, as derived from the optical measurements. Further, similar stoichiometry to the films grown with 2 J/cm^2 was realized with 0.5 J/cm^2,at both deposition substrate temperatures (no results of this laser fluence is presented below), but with lower peak intensity. Comparing the film thicknesses obtained by both lasers (248 nm and 308 nm) used, thicker films were realized with the smaller laser wavelength. This could be correlated with the fact that the absorption coefficient of the target material is maybe increased with the 248 nm laser and thus the diffusion of the heat in the bulk is limited and more material is ablated.

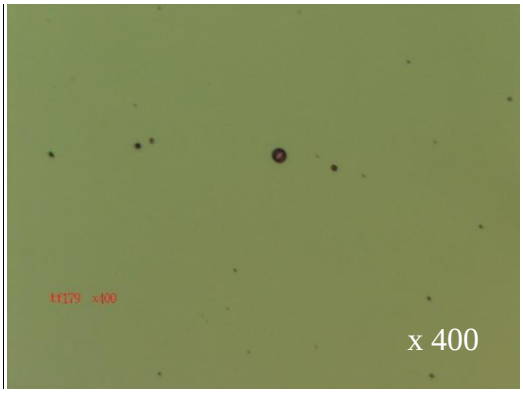

Fig. 6.14: Typical microscope image of a SCO thin film grown on a fused silica substrate (~350 nm thickness) by a 308nm laser wavelength with 10000 laser pulses of 2 J/cm^2 under 5x10^{-4} mbar of Po_2 at 400°C of Ts.

All films grown at 300°C of Ts showed amorphous crystal phase. At 400°C the crystal structure improved and showed the $SrCu_2O_2$ crystalline phase (fig. 6.15), with the (202) crystal orientation dominant. Also a smaller amount of CuO was present, which make us suppose that amorphous Sr containing phases are also present. SCO thin films grown on n-Si, at 300°C, showed similar structural characteristics to the SCO/fs which were grown at 400°C (fig. 6.16).

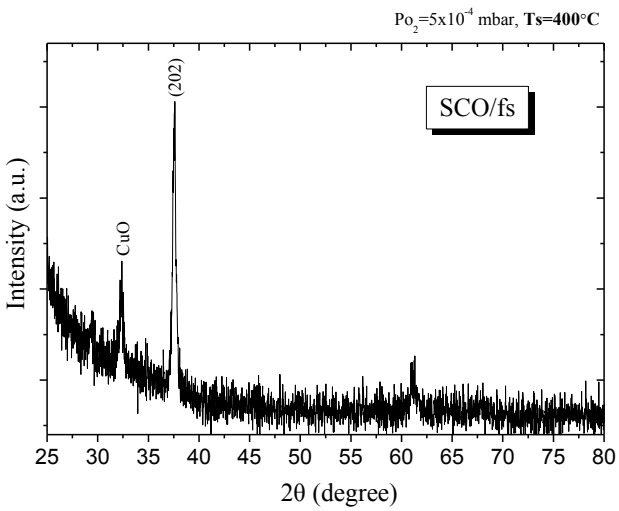

Fig. 6.15: XRD spectrum of a SCO thin film, grown on fused silica substrate by a 308 nm laser, at $5x10^{-4}$ mbar of Po_2 and 400°C of Ts.

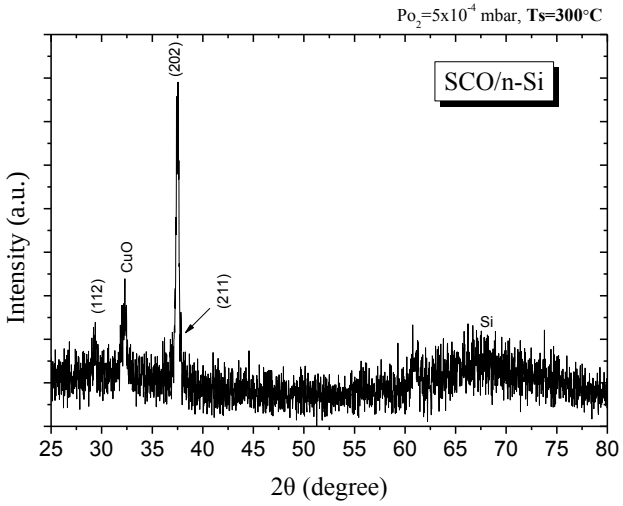

Fig. 6.16: XRD spectrum of a SCO thin film, grown on n-Si substrate by a 308 nm laser, at $5x10^{-4}$ mbar of Po_2 and 300°C of Ts.

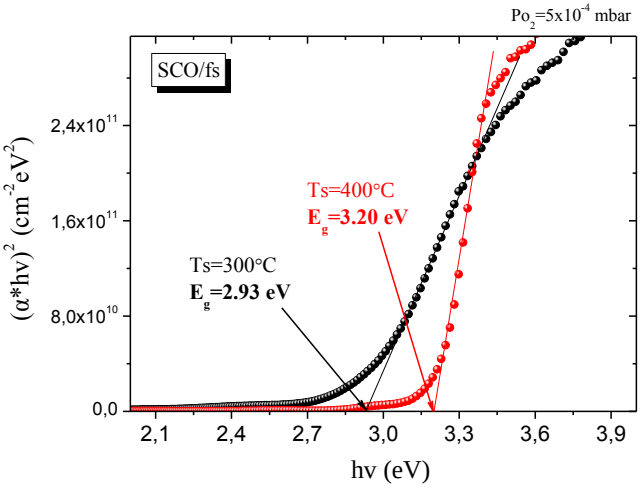

Fig. 6.17: Transmittance and reflectance spectra of a SCO thin film grown on a fused silica substrate at 300 and 400°C of Ts and $5x10^{4}$ mbar of Po_2.

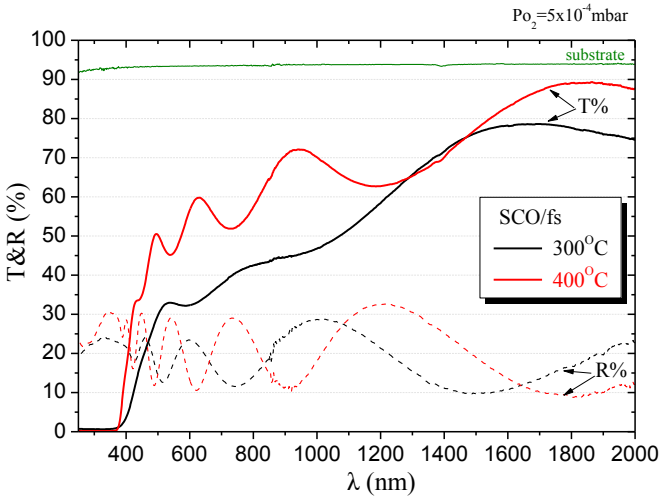

Fig. 6.18: Optical energy band gap, determined by extrapolation of $(\alpha h\nu)^2$ as a function of the photon energy (hν) of a SCO film grown by a 308 nm laser at 300 and 400°C of Ts and $5x10^{4}$ mbar of Po_2.

Fig. 6.17 presents the transmittance and reflectance spectra of a SCO thin film, deposited on fused silica, at 300 and 400°C. For the high substrate temperature a significant increase of the transmittance in the visible region observed, from approximately 30-40% to 35-60%, since the crystal structure improved. In the near-infrared region, the films are relatively transparent, i.e. no significant absorption by the free carriers is observed, maybe similar to the films deposited with

the 248 nm laser. The optical E_g of the films is 2.93 eV (300°C) and 3.20 eV (400°C), evaluated according to Tauc's plot for a direct transition (chapter 4.2.2) (fig. 6.18).

After RTA (at 330°C under forming gas flow for 10 min), the amorphous as-deposited films, which were deposited at 300°C, attain a better crystallized structure and exhibit the $SrCu_2O_2$ crystalline phase and some Cu_2O phase (fig. 6.19). It can be seen that there is an overlap between (202) and (211) crystal orientations, which seem to be dominant including (200) as well. For the films deposited at 400°C, no significant crystal improvement is observed after RTA. The transmittance in the visible region, of the films deposited at 300°C, increases significantly after RTA to approximately 45-85%, but for the films deposited at 400°C only a slight increase is observed (fig. 6.20). After RTA, the optical E_g of the films deposited at 300°C increased to ~3.24 eV, but for the films deposited at 400°C remained almost the same ~3.25 eV.

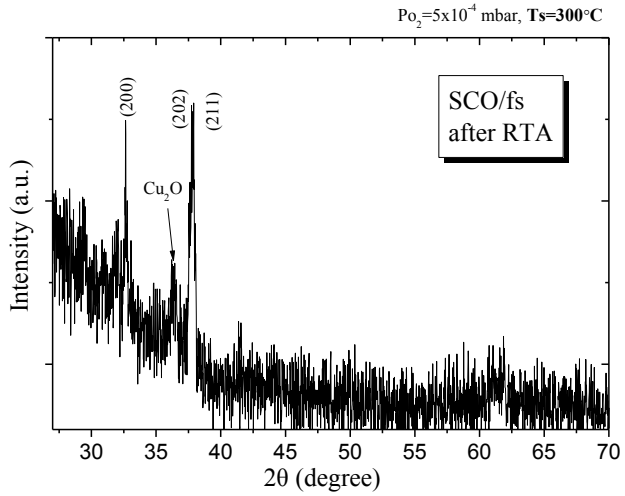

Fig. 6.19: XRD spectrum of a SCO thin film, after RTA, grown on fused silica substrate by a 308 nm laser, at 5x10^{-4} mbar of Po_2 and 300°C of Ts.

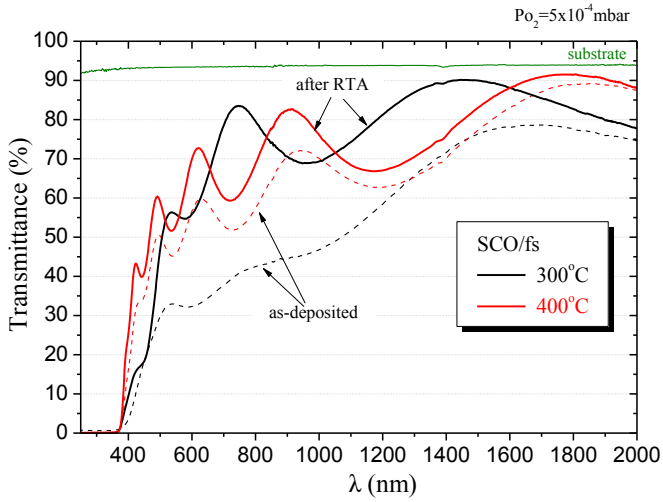

Fig. 6.20: Transmittance spectra of SCO thin films before and after RTA, grown by a 308 nm laser, at 5x10^{-4} mbar of Po_2 and 300 and 400°C of Ts.

6.4.2 DOPED SCO THIN FILMS

SCO:X(3%) and SCO:X(6%) thin films were grown on fused silica and n-Si substrates at the same experimental conditions as the un-doped films. Films grown with 0.5 J/cm^2 laser pulses had the same behavior as with the un-doped films, i.e. low thickness, high transmittance and same crystalline behavior as with films grown with 2 J/cm^2. The thickness of the films, grown with 2 J/cm^2 laser pulses, was between 250 and 500 nm and had surface image alike to the un-doped films (fig. 6.14).

Similar to the un-doped films, all films deposited on fused silica at 300°C show an amorphous phase. When films deposited at 400°C, they mainly developed according to (202) crystal orientation of the $SrCu_2O_2$ phase. Also a smaller amount of the Cu_2O crystalline phase is present. Doped SCO films which were deposited on n-Si substrates, with 2 J/cm^2 laser pulses and at 300°C, contain the $SrCu_2O_2$ crystalline phase, with the (202) being the dominant crystal orientation, and a small amount of CuO phase (figs 6.22). The crystal structure as a function of the doping, for the films deposited on fused silica and Si, does not change, the lattice parameters seem to remain almost unaltered, since no shift of the peaks is observed.

Fig. 6.23 presents the transmittance spectra of the un-doped and doped SCO thin film, deposited on fused silica. It can be seen that there is a significant increase of the transmittance at the visible region with the increase of the substrate temperature, especially for the doped films. In the near-infrared region, the films still indicate high transparency. At 400°C though, the doped films seem to exhibit a small decrease in the transmittance after ~1200 nm, where simultaneously a corresponding increase is happening to the un-doped. This might be an indication of an increased carrier concentration for the doped films. The optical E_g of the SCO:X(3%) and SCO:X(6%) films is ~2.93 and ~2.96 eV at 300°C, respectively, and slightly increases at 400°C to ~3.28 and ~3.30 eV, respectively. Compared to the un-doped films no significant changes are observed.

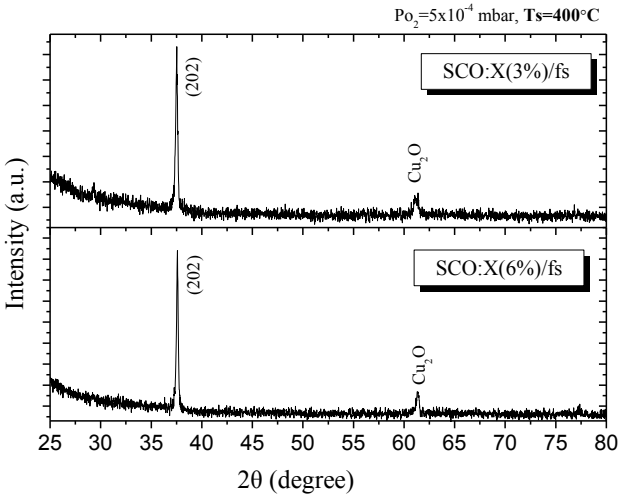

Fig. 6.21: XRD spectra of the X-doped SCO thin film, grown on fused silica substrate by a 308 nm laser, at 5x10^{-4} mbar of Po_2 and 400°C of Ts.

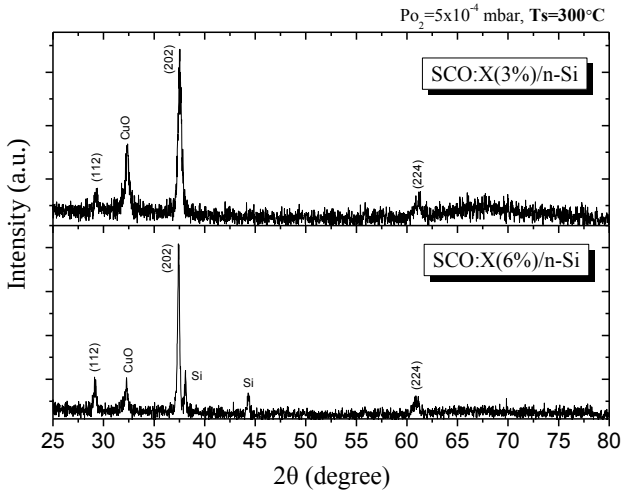

Fig. 6.22: XRD spectra of the X-doped SCO thin film, grown on n-Si substrate by a 308 nm laser, at 5x10^{-4} mbar of Po_2 and 300°C of Ts.

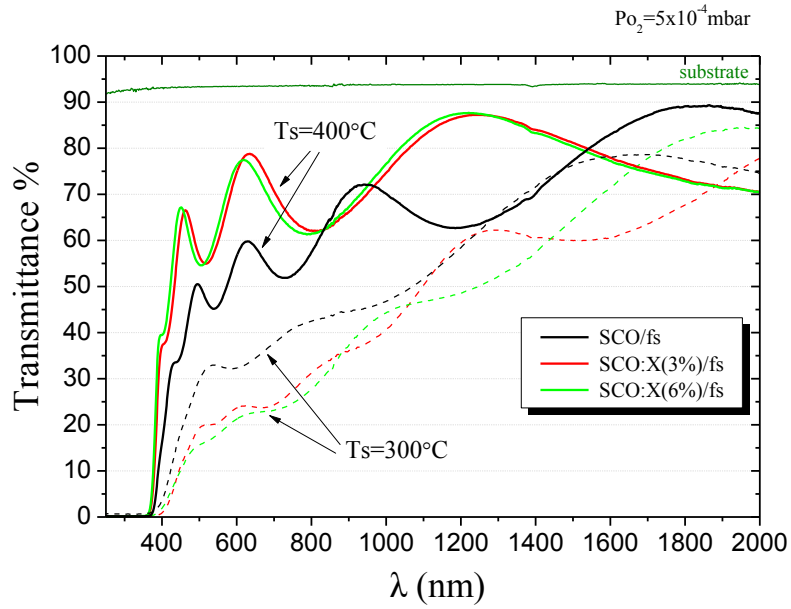

Fig. 6.23: Transmittance of un-doped and X-doped SCO thin films grown by a UV laser of 308 nm wavelength, at 5x10^{-4} mbar of Po_2 and 300 and 400°C of Ts.

After RTA, the films seem to behave quit similar to the un-doped films, that is; the amorphous as-deposited films, grown at 300°C, attain a better crystallized structure after RTA, containing the $SrCu_2O_2$ crystalline phase and a much lesser amount of amorphous and Cu_2O phase compared to the un-doped (fig. 6.24). The crystal structure of the films grown at 400°C remains the same after RTA. The transmittance spectra for the SCO:X(3%) and SCO:X(6%) thin films, before and after RTA are presented in fig. 6.25 (a) and (b), respectively. For the doped films deposited at 300°C, after RTA the transmittance increases significantly in the visible region and the optical E_g estimated 3.15 eV (SCO:X(3%)) and 3.24 eV (SCO:X(6%)). However,

for the Ts of 400°C the increase is slight and the optical E_g remains the same. After RTA, the transmittance appears almost unaltered at the NIR region. Fig 6.26 shows the optical E_g as a function of the doping, before and after RTA at different Ts. As can be seen the dependence on doping is not significant. The optical E_g depends mostly on the experimental parameters (RTA and substrate temperature).

So far, the only available electrical measurements confirmed the p-type conductivity of the films and showed resistivity of the order of ~2-15 Ωcm.

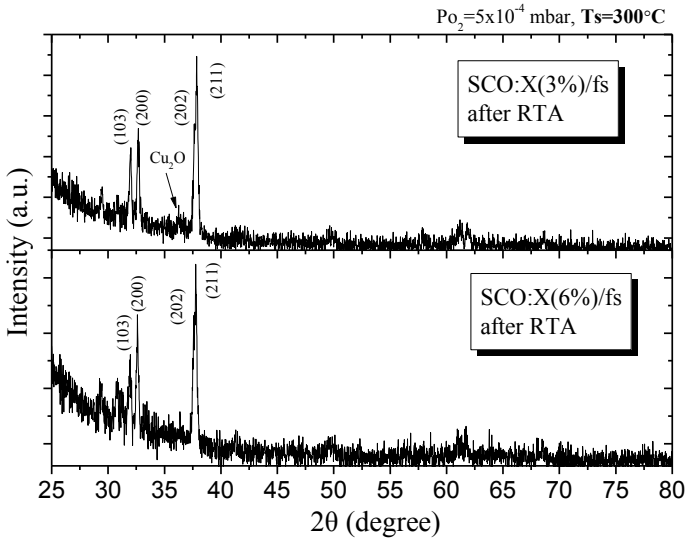

Fig. 6.24: XRD spectra of the X-doped SCO thin film after RTA, grown on fused silica substrate by a 308 nm laser, at 5x10^{-4} mbar of Po_2 and 300°C of Ts.

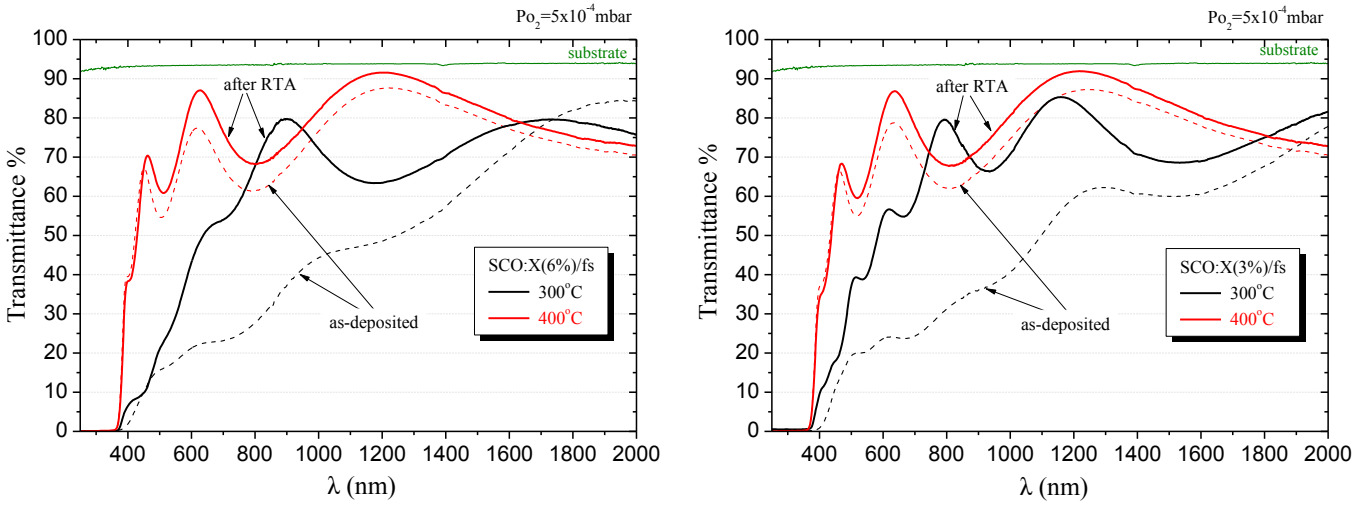

Fig. 6.25: Transmittance spectra of (a) SCO:X(3%) and (b) SCO:X(6%) thin films before and after RTA, grown by a 308 nm laser, at 5x10^{-4} mbar of Po_2 and 300 and 400°C of Ts.

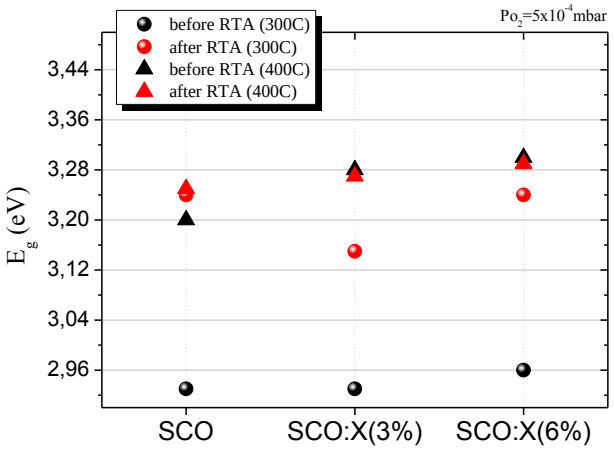

Fig. 6.26: Optical E_g, before and after RTA, as a function of the doping, for films grown by a 308 nm laser at different Ts.

6.5 CONCLUSIONS

Doped and un-doped thin films, which were grown on fused silica and Si substrates with a 248 and 308 nm laser at $5x10^{-4}$ mbar of Po_2, were structurally (XRD) and optically (transmittance & reflectance) characterized.

The films, grown on Si substrates with the 248 nm laser, exhibited phase pure $SrCu_2O_2$ crystal structure at 300 and 400°C. Films, grown with the 308 nm laser, exhibited the $SrCu_2O_2$ phase but a small amount of CuO as well.

All the films grown on fused silica at 300°C had amorphous crystal structure and low transmittance in the visible region. When those films subjected to RTA the crystal structure improved and mainly consisted of the $SrCu_2O_2$ crystal phase, the transmittance significantly increased and a small increase in the optical E_g was observed. The films deposited at 400°C with the 308 nm laser exhibited crystalline structure and high transmittance. After RTA no changes of the structural and optical properties occurred. The XRD results of the films were not consistent with the phase behavior of the bulk. All the films grown on fused silica exhibited high transparency in the NIR region, indicating low carrier concentration even for the doped films.

The derived XRD results of the present work were not consistent with the reports of Kudo[1] and Papadopoulou[2], who obtained phase pure SCO thin films, by PLD with a 248 nm laser, just at 300°C. Sheng[3] reported oriented growth on glass after 350°C. The calculated optical E_g, ~3.10-3.31 eV (248 nm laser) and ~2.93-3.30 eV (308 nm laser), is comparable with the theoretical predictions for the SCO bulk (~3.3 eV) and with those obtained by Papadodopoulou (~3.3 eV, on glass substrates with a 248 nm laser), Kudo (~3.25 eV, on SiO_2 substrates by PLD at 300°C of Ts with a 248 nm laser) and Bobeico[4] (~3.12 eV, on quartz and glass substrates by e-beam evaporation at 350°C of Ts).

To our knowledge, the best electrical properties of un-doped SCO thin films reported by Zhuang[5]. Zhuang fabricated SCO thin films by spin-on process and after annealing at 800°C the films obtained 10^{-4}-$5x10^{-4}$ Ωcm resistivity and $3x10^{19}$ to $2x10^{20}$ cm^{-3} carrier concentration. Also, Bobeico reported 18.9 Ωcm resistivity and $1.5x10^{17}$ cm^{-3} carrier concentration, at 350°C of Ts without post-annealing. So far, to our knowledge, the elements reported for doping SCO are Ca^{+2} by Sheng and K^{+1} by Kudo and Varadarajan[6]. Sheng reported 12.2 Ωcm resistivity and $1.33x10^{17}$ cm^{-3} carrier concentration at 350°C. Kudo reported similar results but after the annealing of the films (~20.8 Ωcm resistivity and $6.1x10^{17}$ cm^{-3} carrier concentration). Varadarajan though reported ρ~$1.4x10^{2}$ Ωcm. The electrical measurements of the annealed X-doped films, obtained in the present work, showed ~10-10^2 Ωcm resistivity and ~10^{15} cm^{-3} carrier concentration, with the 248 nm laser. The resistivity seems to be rather low but the carrier concentration remains at a low value. A bit lower resistivity, 2-15 Ωcm, is obtained with the 308 nm laser.

Further work must be done in order to investigate the electrical properties of the films as a function of different experimental parameters, such as temperature, oxygen pressure or different ambient gas, laser (wavelength, fluence etc.) and other. It must become comprehensible, for the specific material, the reasons of low carrier concentration and low conductivity even for the doped films. It seems that the dopant is not “activated”. Namely, its location in the crystal structure may not favor the Cu vacancy formation and probably that is why no significant increase of the optical E_g is observed as a function of the doping, and no significant increase of the carrier concentration has been estimated from the transmittance data at the NIR region.

6.6 REFERENCES

[1] A. Kudo, et al., Appl. Phys. Lett., 73, No. 2 (1998)

[2] E. Papadopoulou et al., Thin Solid Films, 516 (2008) 1449

[3] S. Sheng, et al., Semicond. Sci. Technol., 21 (2006) 586

[4] E. Bobeico, et al., Thin Solid Films, 444 (2003) 70

[5] W. Zhuang, et al., Integrated Ferroelectrics, 80, 39–45 (2006)

[6] V. Varadarajan, et al., Thin Solid Films, 488 (2005) 173

CHAPTER 7
p-n HETEROJUNCTIONS

7.1 INTRODUCTION

An attempt to examine the characteristics of some heterojunction diodes was made, having as p-type material the p-$SrCu_2O_2$.

The diodes were characterized by I–V and C–V measurements by employing the Keithley 6517A Electrometer and the Agilent 4284A LCR meter or Tektronix-programmable curve tracer-SONY. The processing and the electrical characterization of the diodes were carried out by Dr. Elias Aperathitis

7.2 p-$SrCu_2O_2$ ON n-SI

SCO thin films were grown, by PLD (with the UV-pulsed laser of 248 nm wavelength), on crystalline n-Si (001) substrates at 300 and 500°C of substrate temperature and at $5x10^{-4}$ mbar of oxygen pressure. The PLD conditions and the structural characteristics of the films are presented in paragraph 6.2 and 6.3.2.

To our knowledge, there has been no report in the literature on the value of the electron affinity of the SCO, but an estimation of the energy-band diagram can be done. Due to the wide band gap of SCO (~3.3 eV) compared to the lower band gap of Si (1.12 eV), a rather large conduction band discontinuity is expected at the interface and an approach of the energy band diagram of fig 3.4(b) is expected. Most of the reported oxide semiconductors deposited on Si exhibit diode characteristics which diverge from theoretical calculations due to structural imperfections of the layers and interface states[1]. In order to see whether any oxide would build up on the surface of Si substrate, the Si was heated up to 600°C in the PLD system in flowing oxygen for 1 h. Afterwards ellipsometry measurements revealed that the SiO_2 on the Si surface was not thicker than its native oxide (~4 nm).

The p-SCO/n-Si diodes were fabricated using standard photolithographic technique. The SCO film on the Si substrate was patterned as to have the dot geometry (diameter 700 μm) using diluted HCl solution as etchant for SCO. Ni/Au and In ohmic contacts on SCO and Si, respectively, were deposited by electron-gun evaporation. The In contact was applied at the rear side of the Si substrate after cleaning it with organic and HF. Fig. 7.1 (a) shows a schematic representation of the diode geometry (the area of the p/n junction was 0.38 mm^2) and fig. 7.1 (b) shows the ohmic behavior (linear I–V) of Ni-on-SCO.

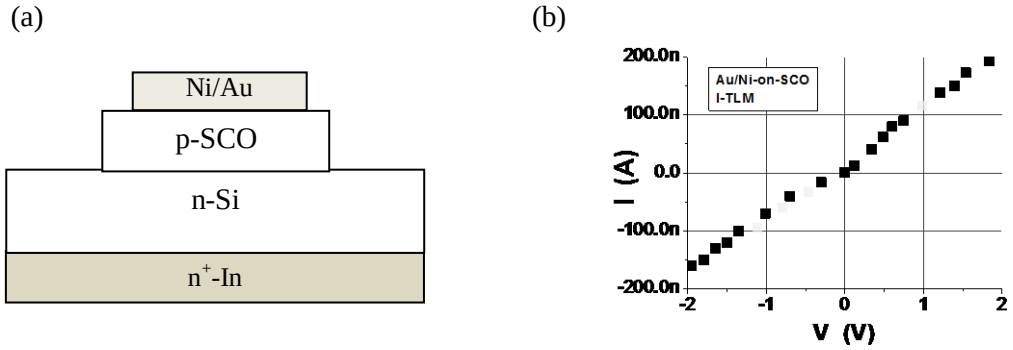

Fig. 7.1: (a) Schematic representation of the Ni-Au / p-SCO / n-Si / In diode. (b) ohmic behavior (linear I–V) of Ni-on-SCO

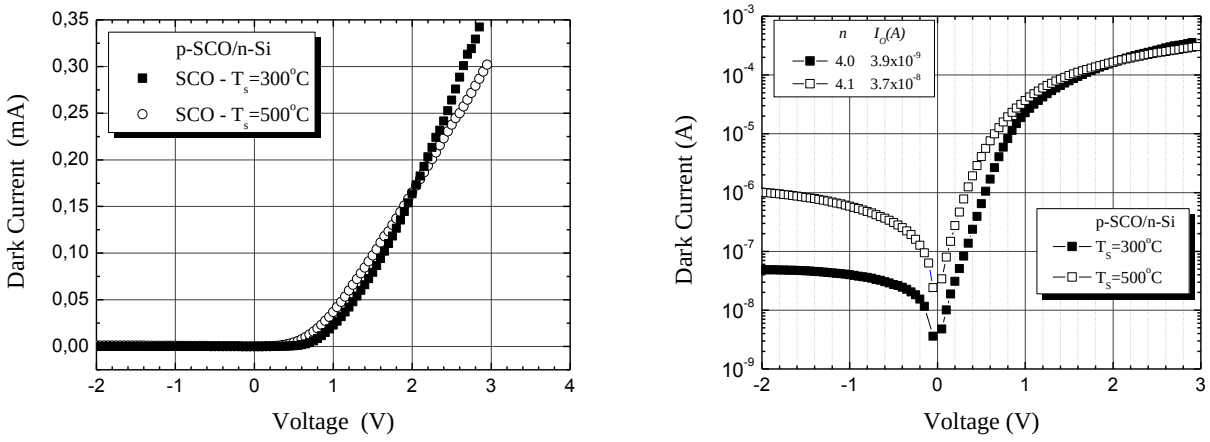

(a) *(b)*

Fig. 7.2: Dark current–voltage characteristics of p-SCO/n-Si diodes in (a) linear and (b) semilogarithmic scale.

The dark current, I_D, as a function of the applied voltage on the p-SCO/n-Si diodes is shown in fig. 7.2 (a) in linear scale and in fig. 7.2 (b) in semilogarithmic scale. The SCO/Si

heterostructures clearly show rectifying behavior. The leakage current at −2 V of the low-temperature (300°C) deposited diode and the high-temperature (500°C) deposited diode was 48.6 nA and 1.0 μA, respectively. Both diodes showed a turn-on voltage at around 0.7 V.

The reverse saturation current I_o and the ideality factor n of the real diode can be extracted from eq. 3.4[x]. The n factor for both diodes was approximately 4, suggesting a complex transport mechanism through the p–n interface of the heterojunction diodes. The I_o was 3.9×10^{-9} and 3.7×10^{-8} A for the low and high temperature deposited diode, respectively. It can be clearly seen at fig. 7.2(b) the voltage drop after ~1 V. The calculated series resistance, which resulted in the voltage drop, for the lower and the higher Ts diode was 6.2 kΩ and 7.7 kΩ, respectively. The relatively high series resistance of the diodes should mainly be attributed to the low doping of the Si substrate (10^{14}-10^{15} cm^{-3}) and the non-optimized ohmic contact used for Si.

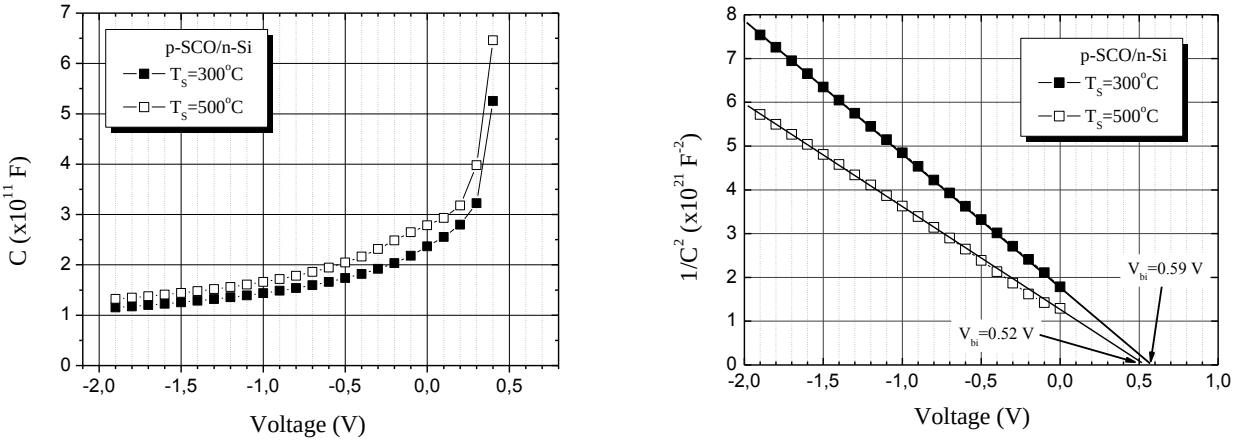

(a) *(b)*

Fig. 7.3: (a) Capacitance as a function of the applied potential and (b) the $1/C^2$ as a function of the reverse bias and the extraction of the built-in potential V_{bi} of the p-SCO/n-Si diodes.

Fig. 7.3(a) shows the capacitance as a function of the applied potential of the p-SCO/n-Si diodes. The junction capacitance is due to the dipole in the transition region. When the junction is forward biased, the depletion region decreases, since $(V_{bi}–V)$ decreases, and consequently the capacitance increases (eq. 3.4).

Eq. 3.4 shows the relationship between the capacitance of the diode and the applied voltage, i.e. $C=c(V_{bi}-V)^{-1/2}$, where c is constant. Plotting $1/C^2$ as a function of the reverse applied voltage V (fig.7.3(b)), the built-in voltage V_{bi} can be extracted by extrapolating the $1/C^2$-*vs*-V plot and the intercept at $1/C^2=0$ is the V_{bi}. A straight line could be fitted on the $1/C^2$–V plot of the low-temperature deposited diode, indicating an abrupt interface, with a V_{bi} of 0.59 V. For the

[x] Eq.3.4, which refers to p-n homojunctions, also corresponds to p-n heterojunctions.

high-temperature deposited diode a V_{bi} of 0.59 V was calculated but a small deviation from the straight line, for reverse bias voltages between -0.5 and 0 V, can be seen. The observed $SrCu_2O_3$ phase in the SCO layer deposited at 500 °C and the possibility of some kind of inter-diffusion (Cu and/or Sr) taking place at the SCO–Si interface during deposition of the SCO layer (copper is known to diffuse in Si, creating deep level traps in the Si band gap[2] might be associated with the lower V_{bi} of this diode.

7.3 p-$SrCu_2O_2$/n-ZnO ON ITO

Two p-n hetrerojunctions were grown by the 248 nm and 308 nm pulsed laser. The structure of the p-n hetrerojunction is Au-Ni/p-SCO:X(3%)/n-ZnO/n^+-ITO on a fused silica substrate. Crystalline thin film of n^+-ITO was grown on fused silica substrate by rf-magneton sputtering, as a transparent metallic electrode. ZnO was deposited onto ITO by PLD at $5x10^{-5}$ mbar of Po_2 and 300°C substrate temperature, representing the n-type material semiconductor of the diode. Next, SCO:X(3%) thin film was deposited onto ZnO by PLD in situ, at $5x10^{-4}$ mbar of Po_2 and Ts=300°C, representing the p-type material semiconductor of the diode. The structure was then subjected to RTA at 330°C in forming gas. The diode was finally fabricated using the same photolithographic technique as for the p-SCO/n-Si diodes.

The ohmic behavior (linear I–V) of Ni-on-SCO is the same as for the case of the SCO/Si diode (fig. 7.1 (b)).

As mentioned in paragraph 3.2, in the case of an asymmetrically doped junction, the depletion layer extends primarily into the less doped side. To limit this situation, p- and n- type materials with similar carrier concentrations should be chosen. The SCO:X(3%) thin films have carrier concentration less than 10^{15} cm^{-3}. Thus, among the fabricated ZnO and ZnO:Al thin films, by the 248 nm laser pulses, the ZnO film deposited at $5x10^{-5}$ mbar of Po_2 and Ts=300°C was chosen to be the participant n-type material for the diode, since it had ~10^{18} cm^{-3} carrier concentration, which is the lowest obtained. Since no work has been done for the growth of ZnO films by the 308 nm laser, it was chosen to grow ZnO films according to the deposition parameters used for the growth of ZnO by the 248 nm laser.

An important advantage of the above materials is their suitability for low temperature deposition, which favors the avoidance of chemical reaction between ZnO and SCO:X(3%). Furthermore, the band gaps of the fabricated ZnO (~3.2eV) and SCO:X(3%) (~3.1eV) do not differ much, as this will favor a less discontinuity at the junction. The energy band diagram of

the heterojunction approaches that of fig 3.2(a), but some discontinuity at the interface is expected.

7.3.1 p-$SrCu_2O_2$:X(3%)/n-ZnO ON ITO BY A 248 nm LASER

The XRD spectrum of the structure, grown by the 248 nm laser, is presented in fig. 7.4. It contains the SCO polycrystalline phase where (211) and (220) are the dominant crystal orientations. Also, the (002) crystal orientation of ZnO, Cu_2O and the diffraction peaks of ITO are visible. The diode has ~20-60% transmittance in the visible range (fig. 7.5), rather predictable since both films showed low transmittance when deposited, separately, on fused silica and further the thickness of the diode is ~900 nm.

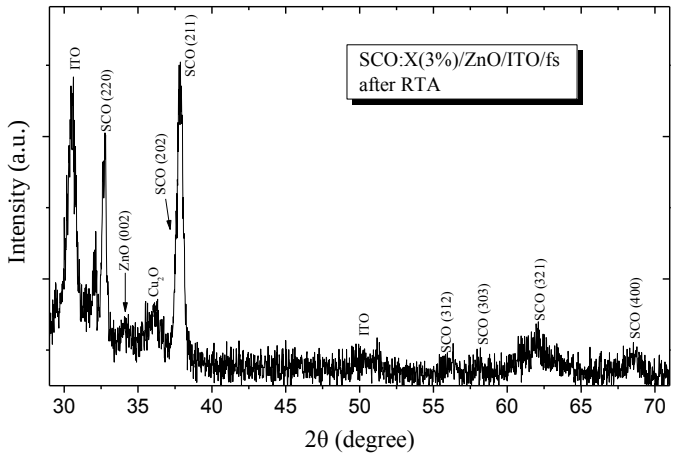

Fig. 7.4: XRD spectrum of the SCO:X(3%)/ZnO structure, grown on a ITO/fs substrate by a 248 nm laser, after RTA at 330°C.

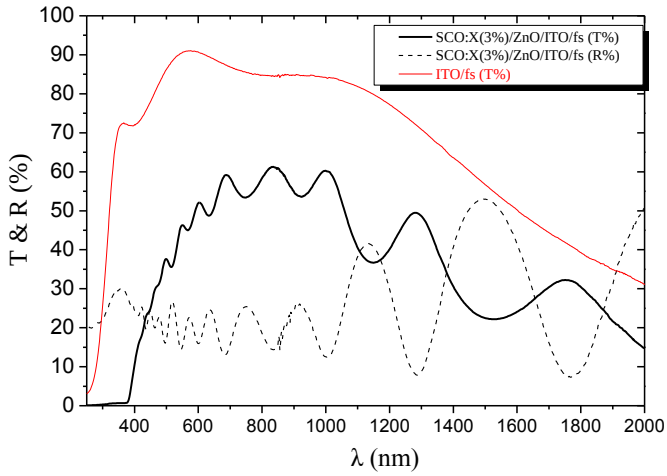

Fig. 7.5: Transmittance and reflectance spectra of the SCO:X(3%)/ZnO structure, grown on a ITO/fs substrate by a 248 nm laser, after RTA at 330°C.

The dark current, I_D, as a function of the applied voltage on the p-SCO/n-ZnO diode is shown in fig. 7.6(a) in linear scale. The SCO/ZnO heterostructure show rectifying behavior. The diode shows turn-on voltage at around 1 V. The reverse saturation current I_o and the ideality factor n are 1.79×10^{-12} mA and ~6.8, respectively, extracted from eq. 3.4. A large deviation from

the ideal diode is observed, probably due to structural imperfections and not abrupt interface (inderdiffusion of atoms at the interface).

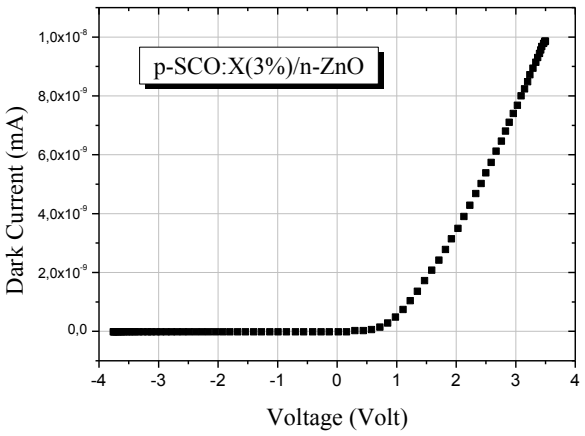

Fig. 7.6: Dark current–voltage characteristics of a p-SCO/n-ZnO diode, grown by a 248 nm laser, in linear scale.

7.3.2 p-$SrCu_2O_2$:X(3%)/n-ZnO ON ITO BY A 308 nm LASER

The thickness of the diode is ~220 nm. The XRD spectrum of the structure, grown by the 308 nm laser, is presented in fig. 7.7, and exhibits the same diffracted peaks to that grown by the 248 nm laser. In this case the peak of the (002) crystal orientation of ZnO is more intense. The diode has ~50-85% transmittance in the visible range (fig. 7.8).

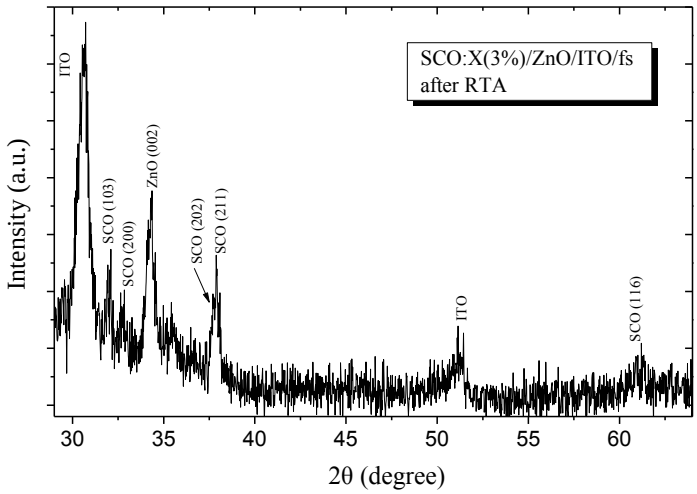

Fig. 7.7: XRD spectrum of the SCO:X(3%)/ZnO structure, grown on a ITO/fs substrate by a 308 nm laser, after RTA at 330°C.

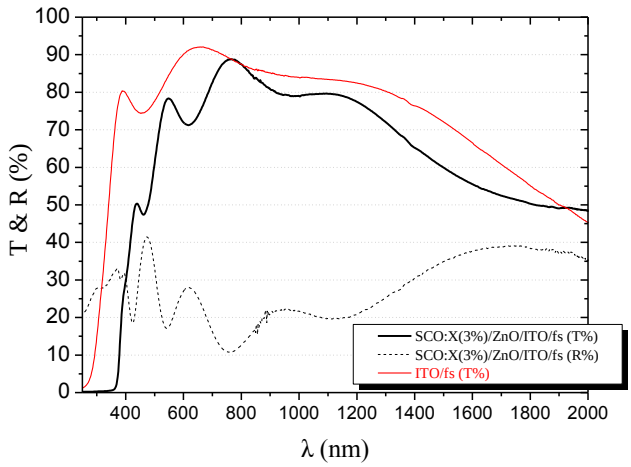

Fig. 7.8: Transmittance and reflectance spectra of the SCO:X(3%)/ZnO structure, grown on a ITO/fs substrate by a 308 nm laser, after RTA at 330°C.

The dark current, I_D, as a function of the applied voltage on diode is shown in fig. 7.9(a) in linear scale. The SCO/ZnO heterostructure show rectifying behavior. The diode shows a "slow" turn-on voltage at around 0.7 V, as in the previous diode but with high leakage current, 0.25 mA at -4 V. The reverse saturation current I_o and the ideality factor n are 1.26×10^{-3} mA and ~8.2, respectively. The structural and interfacial imperfections are probably present.

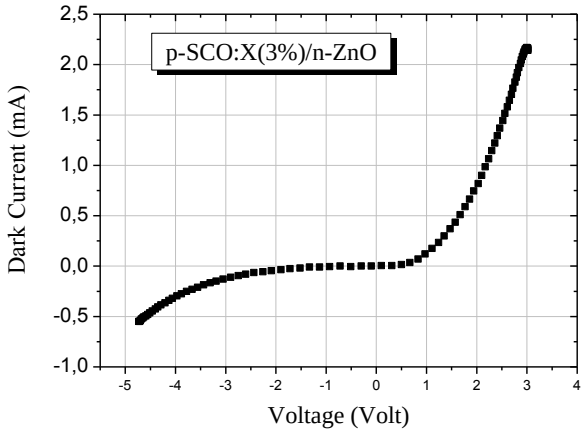

Fig. 7.9: Dark current–voltage characteristics of a p-SCO/n-ZnO diode, grown by a 308 nm laser, in linear scale.

The reported p-n heterojunctions, to our knowledge, so far, utilizing SCO as the p-type semiconductor, are presented in table 7.1. According to the present results, more work is needed for the SCO/ZnO diode which had both layers deposited at the low deposition temperature of 300°C. However, the results are similar to those reported in the literature for such diodes.

7.4 REFERENCES

[1] A.N. Banerjee, et al., Prog. Cryst. Growth Charact. Mater., 50 (2005) 52
J. Gao, et al., Mater. Sci. Eng. B, 144 (2007) 100

[2] J.F. Hermet, et al., J. Appl. Phys. 68 (1990) 638
A.E. Dolbak, et al., Semiconductors 36 (2002) 958

Table 7.1: Growth conditions and properties of p-n heterojunctions, utilizing SCO as the p-type semiconductor.

Structure	Deposition technique	Turn-on voltage (V)	Annealing conditions	comments	Reference
n^+-ZnO/n-ZnO/p-SCO/ITO/glass	SCO ; reactive evapor. at 350 °C n-ZnO ; magn. sputt. at 250 °C	0.3-0.6	-	- Ideality factor *n* 1.62 - structural imperfections - non-reproducible diodes with rectifying behavior - T %: 70-80 % in the visible region	Kudo[1] 1999
Ni/p-SCO:K/n-ZnO/ITO/YSZ	SCO:K ; PLD at 300 °C n-ZnO ; PDL	1.5	SCO:K ann. at 300°C and $7x10^{-4}$ Pa O_2	- Very abrupt heteroepitaxial interface - polycrystalline SCO	Ohta[2] 2000
Ni/p-SCO/n-ZnO/ ITO/YSZ	SCO ; PLD at 350 and 600°C n-ZnO ; PDL	~ 1.2 (350°C) ~ 3 (600°C)	-	Lattice mismatch : 12.9% for SCO(112)/ZnO(0001) at 350°C 72.9% for SCO(100)/ZnO(0001) at 600°C	Hosono[3] 2002
Ni/p-SCO:K /n-ZnO/ In-Ga	SCO:K ; RF magn. sputt. at 300°C on ZnO substrate	0.7 [SCO/ZnO (Zn-face)] 0.9 [SCO/ZnO (A-face)] 2.2 [SCO/ZnO (O-face)]	3 h x 2 at 650 °C	Good transparency	Nakamura[4] 2005
In/n- ZnO:Al/p-SCO:Ca/ITO	SCO:Ca ; PLD at 350 °C Al:ZnO ; RF magn. sputt. at 200°C	0.3-0.6			Sheng[5] 2006
ZnO:Al/n-ZnO/p- SCO:Ca/p-Si	SCO:Ca ; spin-on ZnO ; spin-on	-2.5	- SCO:Ca ; 800°C, 30 min. in vacuum - ZnO: 800°C, 10 min. in Ar	High leakage current at 3 V	Zhuang[6] 2006
Ni/p-SCO:X(3%)/n-ZnO/ITO/fs	SCO:X(3%) ; PLD at 300 °C ZnO ; PDL at 300 °C	~ 0.7	- SCO:X(3%) ; 330°C in forming gas	- Ideality factor *n* ~6.8 and 8.2 - structural imperfections	Present work

[1] A. Kudo, et al., Appl. Phys. Lett., 75, 18 (1999)

[2] H. Ohta, et al., Appl. Phys. Lett., 77, 4 (2000)

[3] H. Hosono, et al., Journal of Crystal Growth, 237–239 (2002) 496–502

[4] Y. Nakamura, et al., Journal of the European Ceramic Society, 25 (2005) 2167–2170

[5] S. Sheng, et al., Semicond. Sci. Technol., 21 (2006) 586–590

[6] W. Zhuang, et al., Integrated Ferroelectrics, 80, 39–45(2006)

PAPERS

1. "*Undoped and Al-doped ZnO films with tuned properties grown by pulsed laser deposition*", E.L. Papadopoulou, M. Varda, K. Kouroupis-Agalou, M. Androulidaki, E. Chikoidze, P. Galtier, G. Huyberechts, E. Aperathitis
Thin Solid Films ***516****, (2008) 8141–8145*

2. "*The effect of PLD deposition parameters on the properties of p − $SrCu_2O_2$/n-Si diodes*", E.L. Papadopoulou, M. Varda, A. Pennos, M. Kaloudis, M. Kayambaki, M. Androulidaki, K. Tsagaraki, Z. Viskadourakis, O. Durand, G. Huyberechts, E. Aperathitis
Thin Solid Films ***516****, (2008) 8154–8158*